INTERNATIONAL SCIENTIFIC JOURNAL

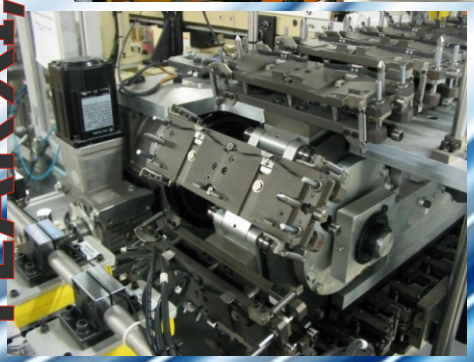
trans & MOTAUTO WORLD

ISSN PRINT 2367-8399
ISSN WEB 2534-8493

YEAR XI, ISSUE 1/2026









SCIENTIFIC TECHNICAL UNION OF MECHANICAL INGENEERING "INDUSTRY 4.0"
108 RAKOVSKI STR., SOFIA 1000, BULGARIA

INTERNATIONAL SCIENTIFIC JOURNAL

TRANS MOTAUTO WORLD

PUBLISHER:

SCIENTIFIC TECHNICAL UNION OF MECHANICAL ENGINEERING INDUSTRY-4.0

108, Rakovski Str., 1000 Sofia, Bulgaria
tel. (+359 2) 987 72 90,
tel./fax (+359 2) 986 22 40**,**
office@stumejournals.com
www.stumejournals.com

All articles are published after peer review by two independent reviewers.

ISSN PRINT 2367-8399
ISSN WEB 2534-8493
YEAR XI, ISSUE 1 / 2026

EDITORIAL BOARD

CHIEF EDITOR
Prof. Petar Kolev, Bulgaria

MEMBERS:

Prof. Ahmet H. Ertas, TR
Prof. Aleksandar Kostikj, MK
Prof. Andrey Ferenets, RU
Prof. Angel Dimitrov, BG
Prof. Beti Angelevska, MK
Prof. Dainis Berjoza, LV
Prof. Dan Scarpete, RO
Prof. Daniela Todorova, BG
Prof. Emilia Andreeva-Moschen, AT
Prof. Hristo Stanchev, BG
Prof. Igor Penkov, EE
Prof. Igor Smirnov, UA
Prof. Igor Taratorkin, RU
Prof. Iliyan Lilov, BG
Prof. Lech Sitnik, PL
Prof. Ljudmila Boyko, UA
Prof. Madaminjon Aripdzanov, UZ
Prof. Martin Kendra, SK
Prof. Massimo Borghi, IT
Prof. Miho Mihow, BG
Prof. Murat Dogruel, TR
Prof. Natalia Sidenko, LV
Prof. Natasa Tomic-Petrovic, RS
Prof. Nikolay Georgiev, BG
Prof. Nikolay Ovchenkov, RU
Prof. Oleg Sharkov, RU
Prof. Pepo Yordanov, BG
Prof. Polatbeg Zhunisbekov, KZ
Prof. Rinat Kurmaev, RU
Prof. Rosen Ivanov, BG
Prof. Sanjin Troha, HR
Prof. Teymuraz Kochadze, GE
Prof. Tomaz Morchadze, GE
Prof. Vadim Zhmud, RU
Prof. Valyo Nikolov, BG
Prof. Zoran Jovanovic, RS

RESPONSIBLE SECRETARY:
Prof. Nikolay Tonchev, Bulgaria

C O N T E N T S

TRANSPORT TECHNICS. INVESTIGATION OF ELEMENTS.

Using laser surface microtexturing to improve tribological properties of surfaces
Jakub Brezina, Štefan Novotný, Janette Brezinová, Péter Pinke 3

Application possibilities of ultrasonic testing for quality control of resistance spot welds in the automotive industry
Ján Viňáš, Marie Kolaříková, Ladislav Kolařík 8

Comparative thermo-mechanical severity assessment of automotive brake discs under repeated braking cycles
Halil Demolli, Gezim Preniqi, Shkelzen Shabani 13

Implementation of Composite Materials into the Design of an Experimental Vehicle for the Shell Eco-Marathon Competition
Štefan Kender, Štefan Novotný 17

Operation guidelines for proper arrangement of pumps in the marine steam propulsion system
Mrzljak Vedran, Prpić-Oršić Jasna, Jelić Maro, Baressi Šegota Sandi 21

Mesh-Converged Modal Profile Assessment of Functionally Graded Spur Gears
Shkelzen Shabani, Halil Demolli 25

TRANSPORT. SAFETY AND ECOLOGY. LOGISTICS AND MANAGEMENT

Traffic safety in Serbia and automotive industry today
Nataša Tomić-Petrović 28

Technical validity of motorcycles and mopeds as a factor of road safety in the Republic of Croatia
Luka Zovak, Goran Košir, Goran Zovak, Marija Ferko 30

Determining the use indicators of the wagon vehicle and improving the efficiency of the transportation process
Israil Shukur Oglu Elyazov, Etibar Bakhtiyar Oglu Guliyev 35

ENGINES

Prospects for the use of liquefied gas in marine diesel engines
Romanoz Topuria, Teimuraz Kochadze, Mikheil Lejava, Zaza Shubladze, Malxaz Tavdgiridze 41

Piston secondary dynamics and their effect on blow-by, friction and power loss.
Erjon Selmani, Shpresa Caslli, Fadil Likaj 45

Using laser surface microtexturing to improve tribological properties of surfaces

Jakub Brezina[1], Štefan Novotný[1], Janette Brezinová[1], Péter Pinke[2]
Technical University of Košice, Faculty of Mechanical Engineering, Slovakia[1]
Óbudai Egyetem Bánki Donát, Faculty of Mechanical and Safety Engineering, Budapest, Hungary[2]
correspondence: jakub.brezina@tuke.sk

Abstract: *Tribological properties of functional surfaces are a key factor influencing the durability, reliability and efficiency of mechanical systems. One of the progressive approaches to surface modification is laser surface microtexturing, which allows for the precise creation of controlled microstructures capable of modifying contact conditions and lubricant retention at tribological interfaces. This article focuses on the application of laser-induced surface microtexturing to improve the tribological performance of hard nanocomposite coatings nACRo³ and nACRo⁴ . The experimental part of the research is dedicated to the preparation of microtextures on the substrate surface using a pulsed laser system, followed by the deposition of nanocomposite coatings nACRo³ and nACRo⁴ . The created microstructures are characterized in terms of their geometry, distribution and influence on the contact properties of the coated surfaces. The wettability of the microtextured surfaces was evaluated based on the measurement of the contact angle. Optimizing surface microtexture is an effective way to increase wettability and potentially improve lubrication conditions during technological processes of forming or tribological loading of materials.*
Keywords*: laser surface texturing, tribology, nanocomposite coating, wettability, contact angle, PVD coating, tool steel, die casting*

1. Introduction

The tribological properties of functional surfaces represent a key factor influencing the service life, reliability and operational efficiency of mechanical systems. Currently, growing demands to reduce energy losses, minimise wear and extend the service life of components are driving intensive research into new surface modification methods. The condition of the surface layer and the nature of the contact interface play a decisive role in load transfer, friction generation and the initiation of degradation processes during operation. For this reason, considerable attention is devoted to progressive surface engineering technologies that enable targeted modification of the topography and functional properties of surfaces according to the required operating conditions [1–3].

One of the promising methods for improving tribological properties is laser surface microtexturing [4,5,8]. This technology enables the precise and reproducible creation of microstructures with a defined geometric shape, dimensions and distribution on the material surface.

Laser surface microtexturing is a modern surface engineering technology based on the localised action of highly concentrated laser energy on the material surface [5,9]. Using precisely controlled pulsed laser systems, microstructures of various geometric shapes can be created, such as dimples, grooves, channels or regular grid-like structures, with dimensions ranging from a few micrometres to tens of micrometres. A significant advantage of this technology is the high precision of the process, the possibility of non-contact surface modification and the ability to be applied to materials with high hardness or to surfaces coated with protective coatings. Microtexture parameters, such as depth, diameter, density and the mutual arrangement of the microstructures, have a fundamental influence on the resulting tribological properties of the surface. A properly designed microtexture can reduce the real contact area between tribological pairs, promote the hydrodynamic effect of lubrication and stabilise the lubricating film during operation. In addition to tribological applications, laser microtexturing is also used to improve coating adhesion, increase corrosion resistance, control surface wettability and for the treatment of biologically active implants. Thanks to its flexibility and possibility of precise process control, laser microtexturing ranks among the promising technologies employed in the development of intelligent and highly functional surfaces for modern technical applications.

The advantages of laser microtexturing include high process flexibility, non-contact machining and the possibility of application to a wide range of engineering materials. The created microtextures can significantly influence contact conditions at the tribological interface, improve lubricant retention, promote the formation of a stable lubricating film and simultaneously reduce adhesive and abrasive wear mechanisms. In addition, the microstructures can act as lubricant reservoirs or trap wear particles, thereby contributing to the stabilisation of the tribological process [6,7,8].

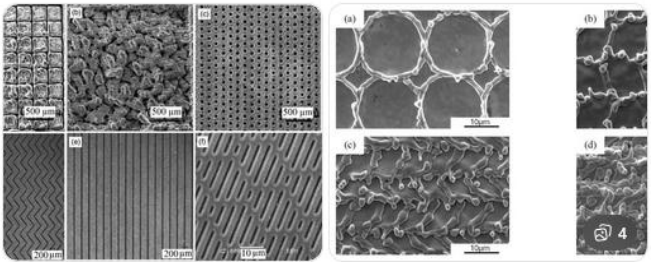


Fig. 1 *Microtextured surface produced by a pulsed laser system with regularly arranged microstructures designed to improve the tribological properties of the surface*

In the design of microtexture geometry, research in recent years has frequently drawn inspiration from natural surfaces that have been evolutionarily optimised to minimise friction, reduce adhesion or enable efficient liquid transport [13,14]. This approach, referred to as biomimetics or bionic surface design, is based on the study of structures found, for example, on shark skin, butterfly wings, lotus leaves or the surface of desert beetles. The surfaces of these organisms feature naturally formed micro- and nanostructures that provide specific functional properties, such as a self-cleaning effect, reduced flow resistance or increased wear resistance. Laser microtexturing therefore frequently employs textures in the form of regular dimples, grooves or hierarchical structures that mimic natural patterns. Biomimetic microtextures can significantly improve lubricant retention, stabilise the lubricating film and reduce contact stresses at the tribological interface. The results of several studies confirm that properly designed biomimetic structures can effectively reduce the coefficient of friction and wear rate compared to conventional smooth surfaces.

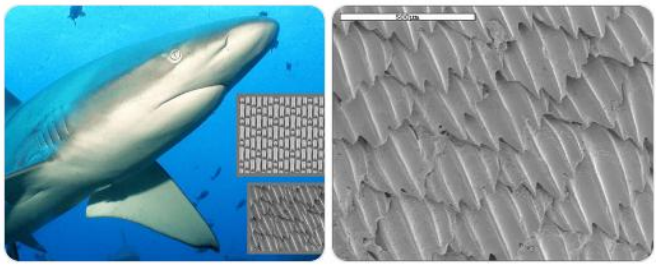


Fig. 2 *Biomimetic microtexture inspired by shark skin structure, used to reduce friction and optimise flow in tribological contact*

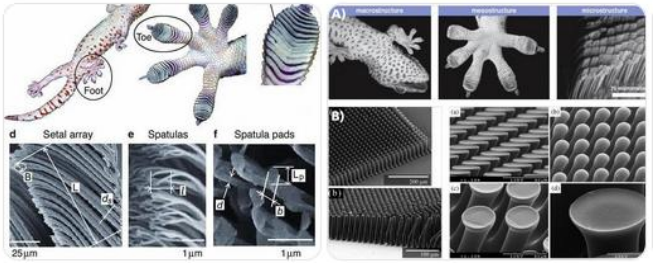


Fig. 3 *Biomimetic microstructure inspired by the surface of gecko foot pads, used to optimise the adhesive and frictional properties of functional surfaces.*

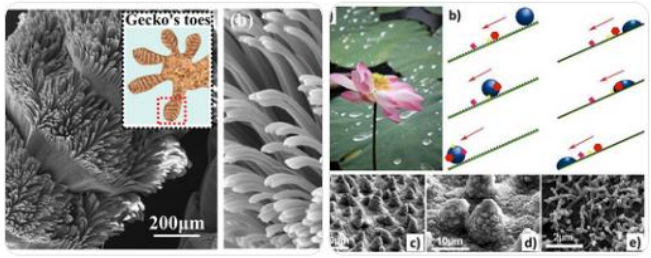


Fig. 4 *Surface structure inspired by snake skin, characterised by directionally oriented microgrooves that ensure friction reduction.*

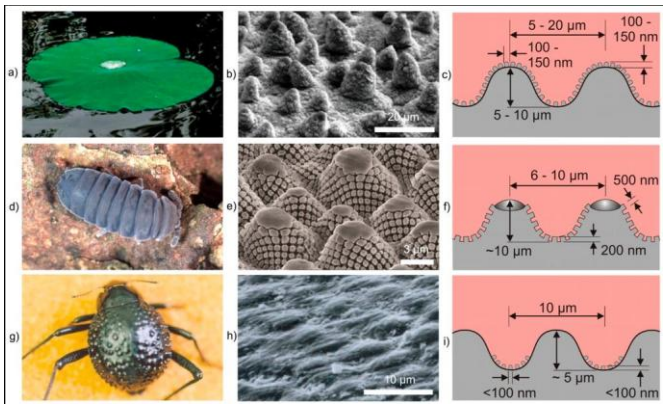


Fig. 5 *Biomimetic texture inspired by the surface of the desert beetle, used to control wettability and liquid retention on functional surfaces.*

In combination with modern hard coatings, laser microtexturing represents a promising approach to the development of highly functional surfaces intended for demanding operating conditions [10–12]. Of particular importance in this area are nanocomposite coatings, which are characterised by high hardness, good thermal stability and enhanced wear resistance. Among the progressive types of such coatings are the nanocomposite coatings nACRo³ and nACRo⁴ , which find application primarily in the field of cutting tools, engineering components and highly loaded functional surfaces. Their tribological behaviour, however, can be significantly affected by the nature of the substrate surface and its microgeometry [24-28].

This paper deals with the application of laser surface microtexturing to improve the tribological properties of nanocomposite coatings nACRo³ and nACRo⁴ . The experimental part of the study focuses on the preparation of microtextures using a pulsed laser system and the subsequent deposition of the aforementioned coatings on the modified substrate surface. Attention is paid to the characterisation of the created microstructures in terms of their geometry, distribution and influence on the contact characteristics of the surface. The tribological properties of the prepared surfaces are then analysed through friction and wear tests conducted under defined operating conditions. The work also includes a morphological analysis of the worn surfaces, which enables identification of the dominant wear mechanisms and evaluation of the effectiveness of the applied surface treatment.

2. Materials and Methods

Samples made from a material used in the manufacture of dies for high-pressure die casting of Al alloys were used for the experimental part. Specifically, this is the tool steel Uddeholm Dievar, alloyed with chromium, molybdenum and vanadium, and also containing further elements that improve its mechanical and thermal properties. This material is designed for operation at elevated temperatures and is characterised by high resistance to thermal fatigue and wear, which is typical of dies used in high-pressure aluminium die casting. In practice, it is used primarily for the manufacture of dies for aluminium alloys and their shaped and functional components. Products made from this steel are manufactured using powder metallurgy technology, which ensures a homogeneous microstructure and favourable in-service properties. The chemical composition of Uddeholm Dievar — a high-strength die steel — is given in Table 1, and the mechanical properties in Table 2.

Table 1: Chemical composition of Uddeholm Dievar substrate

Chemical element	C	Si	Mn	V	Mo	Cr
Weight [%]	0.38	0.2	0.5	0.6	2.3	5

Table 2: Mechanical properties of Uddeholm Dievar substrate

Tensile strength Rm [MPa]	Hardness [HRC]	Proof strength $Rp_{0.2}$ [MPa]	Elongation A [%]	Reduction of area [%]
1480	44	1210	13	55

Substrate Surface Texturing

The Piranha Multi FL205 laser system (ACSYS Lasertechnik), equipped with a ytterbium (Yb) fibre laser with a nominal power of 20 W, was used for substrate surface texturing. Two distinct morphological types of dimple textures were produced during experimental preparation: stochastically generated and regularly arranged. Regular textures were created in the form of grid structures with defined periodicities of 50 × 50 µm, 100 × 100 µm and 50 × 100 µm (Fig. 6). The primary objective of the surface treatment was to experimentally verify the hypothesis that dimple textures act as reservoirs for the release agent during the high-pressure die casting of aluminium alloys, thereby potentially influencing the tribological and adhesive conditions at the die-melt interface.

Application of nACRo3 and nACRo4 Coatings

Two types of physical vapour deposition (PVD) coatings — specifically nACRo3 and nACRo4 — were applied to both the textured and non-textured substrate surfaces, while a third group of samples remained uncoated. Deposition was carried out by means of advanced PVD technologies — cathodic arc evaporation and magnetron sputtering. Key process parameters, such as the supply of reactive gases (primarily nitrogen) and alloying elements (e.g. silicon), were controlled to ensure the required microstructure, high coating density and optimum adhesion to the substrate, which was supported by the use of appropriate interlayers (e.g. CrN or AlCrN).

The nACRo3 and nACRo4 coatings belong to the group of advanced nanocomposite protective layers based on the Al-Cr-N system and its modified variants. Their microstructure is derived from the concept of nc-(Al,Cr)N/a-Si_3 N_4 nanocomposites, in which nanocrystalline grains of the (Al,Cr)N phase with a typical size of approximately 5–10 nm are embedded in an amorphous or quasi-amorphous matrix. This characteristic architecture leads to a synergistic combination of high hardness, thermal stability and resistance to oxidative and tribological wear. The nanocomposite effect, based primarily on the restriction of dislocation movement (Hall–Petch mechanism) and the presence of an amorphous phase acting as a barrier to crack propagation, leads to increased hardness (approximately 30–40 GPa), toughness and resistance to delamination.

From the perspective of chemical composition and microstructural optimisation, the nACRo3 and nACRo4 coatings represent evolutionary modifications of classical AlCrN systems. The nACRo3 coating can be characterised as an older generation with a relatively higher chromium content and a lower proportion of amorphous phase. It is characterised by a fine-grained structure and a balanced ratio of hardness, adhesion and toughness. The presence of chromium promotes the formation of a stable passivation layer of $Cr_2 O_3$ at elevated temperatures, which increases the oxidation resistance of the coating. Typical hardness values range from 30 to 35 GPa, and the coating exhibits good resistance to abrasive wear and a favourable coefficient of friction. These properties predestine it primarily for applications with moderate thermal and mechanical loading, such as conventional metal cutting. The nACRo4 coating represents a newer generation with an optimised chemical composition, characterised by a higher aluminium content and often also a more pronounced proportion of amorphous phase (e.g. $Si_3 N_4$ -based). This modification leads to an even finer nanostructure and a more homogeneous phase distribution, manifested as an increase in hardness to approximately 35–40 GPa and improved resistance to plastic deformation. The higher aluminium content promotes the formation of a protective $Al_2 O_3$ layer, which ensures high oxidation stability even at temperatures exceeding 1000 °C and increases resistance to degradation processes, including recrystallisation under long-term thermal loading. From a tribological point of view, both coatings are characterised by a low coefficient of friction (approximately 0.4–0.6 depending on operating conditions) and high wear resistance even at high contact pressures. From an application standpoint, the nACRo3 and nACRo4 coatings are intended primarily for tooling applications, especially in the machining of difficult-to-cut materials such as high-temperature alloys, stainless steels and titanium alloys. Their high thermal stability enables effective use under dry machining or minimum quantity lubrication (MQL) conditions. While the nACRo3 coating offers a balanced compromise between mechanical and tribological properties under moderate loading, the nACRo4 coating is optimised for extreme conditions, such as high-speed machining where high temperatures and intense wear dominate. The differences between these coatings thus stem primarily from their chemical composition and nanostructural arrangement, which determine their resulting mechanical, thermal and tribological characteristics.

Evaluation of Surface Wettability of Samples

Within the experimental evaluation, the effect of surface texturing on surface wetting was analysed, with the contact angle as the primary monitored quantity. This parameter represents the fundamental quantitative indicator of wettability and enables evaluation of the interaction between the material surface and the liquid, which is closely linked to the surface energy and topography.

Measurements were performed on surfaces with both stochastic and regular textures, with the regular texture represented by grids with dimensions of 50 × 50 µm and 100 × 50 µm. The investigated surfaces were also coated with nACRo3 and nACRo4 PVD coatings, which can significantly influence not only the mechanical and tribological properties, but also the wetting behaviour of the surface through changes in its chemical composition and energy state. Wettability determination was carried out in accordance with the requirements of standard ISO 19403-2:2017 using the Advex Instruments measurement system. The contact angle was determined by the optical method as the angle between the tangent to the droplet and the sample surface at the three-phase boundary.

Three liquids with different physicochemical properties were selected as test media: distilled water as a reference solution and two technologically used release agents, Safety Lube 61014B and Safety Lube 68502. Each liquid was applied to the sample surface using a laboratory micropipette in the form of droplets with a defined volume. The contact angle between the sample surface and the liquid was then evaluated. To increase the reliability of the results, the measurements were performed repeatedly and subsequently subjected to statistical analysis.

3. Results

Surface Texturing

This subsection presents the results of substrate surface texturing. The created dimple structures with stochastic and regular arrangement are presented. The individual texture types are shown in Fig. 6.

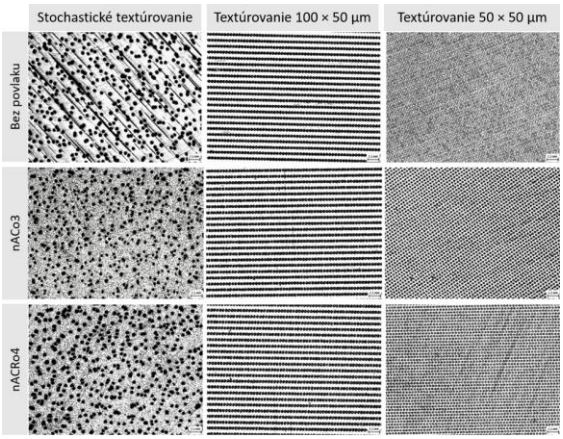


Fig. 6 Surface structuring of samples

Evaluation of Surface Wettability of Samples

The wettability of sample surfaces was evaluated by measuring contact angles. These measurements were carried out using two types of release agents, specifically Safety Lube 61014 and Safety Lube 68502. The obtained data were evaluated and mutually compared.



Fig. 6 Illustration of contact angle measurement at the droplet/substrate interface with Safety Lube 61014 B on uncoated samples

The results presented in Fig. 7 and 8 show that the release agent Safety Lube 61014B in combination with an uncoated sample exhibits the best wetting properties with the regular 100 × 50 µm texture. Conversely, for samples with nACRo3 and nACRo4 PVD coatings, the regular 50 × 50 µm texture appears most suitable in terms of wettability. This difference can be attributed to the combined effect of texture geometry and the modified surface properties of the coatings, which influence liquid spreading on the surface and droplet stability.

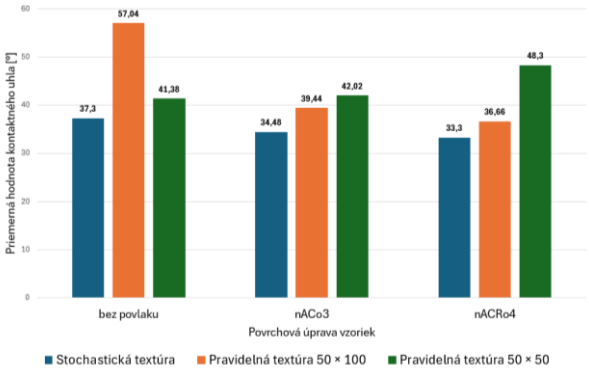


Fig. 7 Graphical representation of sample surface wettability with Safety Lube 61014 B

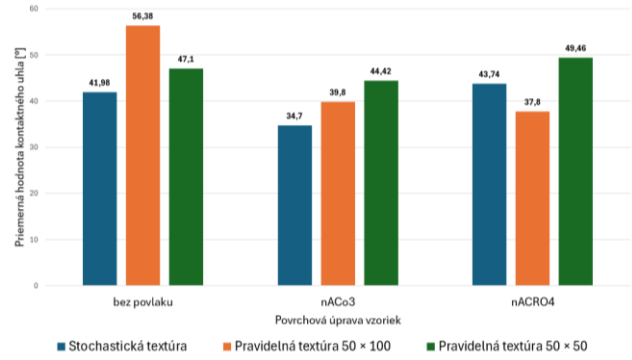


Fig. 8 Graphical representation of sample surface wettability with Safety Lube 68502

A lower surface contact angle is conditioned not only by the texture itself, but also by the type of applied coating. The results clearly show that the texture has a considerable influence on the contact angle value, and that the application of a PVD coating leads to its visible reduction. This finding has a significant impact on practical use in the technological processes of aluminium die casting, where the control of wettability is a key factor.

4. Conclusion

Based on the evaluation of contact angles, it can be stated that surface wettability was significantly influenced by both the type of surface treatment and the Safety Lube lubricant used. For both investigated lubricants, it was generally found that a lower contact angle indicates better surface wettability; the best results were achieved by samples with a regular 50 × 50 µm texture (for coated samples) or a regular 100 × 50 µm texture (for uncoated samples), or alternatively a stochastic texture depending on the coating type; surfaces without texture (“untextured”) exhibited higher contact angle values in most cases, indicating poorer wettability.

With Safety Lube 61014 B, a more pronounced effect of surface texturing was observed. The regular 50 × 50 µm texture achieved the lowest contact angle values, particularly on the nACRo3 surface, indicating improved spreading of the lubricant on the surface. Conversely, some coating-texture combinations led to an increase in contact angle, pointing to a different interaction between the lubricant and the surface microgeometry. The combination of a suitable texture and surface treatment can significantly improve the tribological properties of the surface; regular microtexture promotes more uniform lubricant spreading, although the effect of the texture also depends on the chemical character of the coating and the lubricant used.

Optimisation of surface microtexture represents an effective means of increasing wettability and potentially improving lubrication conditions in technological processes of forming or tribological loading of materials.

Acknowledgments: This research is the result of a project supported by project Visegrad Fund fellowship No. 62610056 - Scientific Cooperation in Advanced Surface Engineering: Joint Research on PTA and Laser Cladding for Die-Casting Mold Renovation. The Slovak Research and Development Agency, the VEGA Scientific Grant Agency "Possibilities of applying laser additive technologies in the restoration of functional surfaces" (1/0597/23), the Cultural and Educational Grant Agency KEGA "Hybrid education of students for the current needs of the automotive industry" (024TUKE-4/2025) and “Increasing the competences of graduates in the automotive production study program using virtual reality tools" (042TUKE-4/2026), "Innovative approaches to the restoration of functional surfaces by laser surface treatment" (APVV-20-0303) and "Integrity of protective multilayers under high-temperature exposure conditions" (APVV-24-0381).

5. References

1. ETSION, Izhak. Improving tribological performance of mechanical components by laser surface texturing. Tribology Letters. 2004, 17(4).
2. SCHILLE, J., SCHNEIDER, L., MAUERSBERGER, S. et al. High-rate laser surface texturing for advanced tribological functionality. Lubricants. 2020, 8(3).
3. MENEZES, P. L., KISHORE and KAILAS, S. V. Influence of surface texture on coefficient of friction and transfer layer formation during sliding. Wear. 2006, 261.
4. ARSLAN, A., MASJUKI, H. H., KALAM, M. A. et al. Effects of texture diameter and depth on the tribological performance of DLC coating under lubricated sliding condition. Applied Surface Science. 2015, 356.
5. SUGIHARA, T. and ENOMOTO, T. Improving anti-adhesion in aluminum alloy cutting by micro stripe texture. Precision Engineering. 2012, 36(2).
6. STRATAKIS, E., BONSE, J., HEITZ, J. et al. Laser engineering of biomimetic surfaces. Nature Reviews Physics. 2020, 2.
7. SKOULAS, E., MANOUSAKI, A., FOTAKIS, C. and STRATAKIS, E. Biomimetic surface structuring using cylindrical vector femtosecond laser beams. Scientific Reports. 2017, 7.
8. CAI, Y. et al. Enhancement of tribological performance with laser surface texturing: A review. Proceedings of the Institution of Mechanical Engineers, Part J: Journal of Engineering Tribology. 2025.
9. SHENG, Z. et al. Tribological effects of surface biomimetic micro-nano textures on metal cutting tools: A review. Biomimetics. 2025, 10(5).
10. LIN, N. et al. Surface texture-based surface treatments on Ti6Al4V alloys. Materials. 2018, 11.
11. MORABČÍKOVÁ, J. et al. Influence of laser texturing and coating on the tribological properties of tool steels. Machines. 2024, 12(5).
12. SONG, X. et al. Biomimetic lubricant-grafted surfaces on laser-textured coatings. Friction. 2024, 12(12).
13. BHUSHAN, Bharat. Introduction to Tribology. Hoboken: Wiley, 2013.
14. BHUSHAN, Bharat. Biomimetics: Bioinspired Hierarchical-Structured Surfaces for Green Science and Technology. Berlin: Springer, 2012.
15. PUOZA, J. C. et al. Research progress of surface texturing and thermal diffusion technologies in tribology. Surface Engineering and Applied Electrochemistry. 2025.
16. ROSENKRANZ, A., GRÜTZMACHER, S., GACHOT, C. and MÜCKLICH, F. Fundamentals of laser surface texturing for tribological applications. Lubricants. 2020, 8(10).
17. XING, Y., DENG, J., WU, G. and LI, S. Effect of laser surface texturing on tribological performance under starved lubrication conditions. Tribology International. 2021, 156.
18. ZHAO, H., WANG, X., LIU, Y. et al. Recent advances in biomimetic surface texturing for tribological applications. Coatings. 2021, 11(6).
19. ZHAO, L., WANG, Q., ZHANG, J. et al. Influence of laser micro-textures on wettability and tribological behavior of coated surfaces. Surface and Coatings Technology. 2021, 426.
20. VAZIRISERESHK, M. R., MARTINI, A., STRUBBE, D. and BAYLES, J. Solid lubricant performance with surface texturing under lubricated sliding conditions. Lubricants. 2021, 9(2).
21. LU, X., ZHOU, H., CHEN, Y. et al. Biomimetic micro/nanostructured surfaces fabricated by laser processing for multifunctional applications. Micromachines. 2022, 13(4).
22. BONSE, J., HÖHM, S., KIRNER, S. V., ROSENFELD, A. and KRÜGER, J. Laser-induced periodic surface structures — A scientific evergreen. IEEE Journal of Selected Topics in Quantum Electronics. 2022, 23(3).
23. PAIVA, J. M., FOX-RABINOVICH, G., LOCKS JUNIOR, E. et al. Tribological and wear performance of nanocomposite PVD hard coatings deposited on aluminum die casting tool. Materials. 2018, 11(3), 358. DOI: 10.3390/ma11030358.

24. LILLE, H., RYABCHIKOV, A., PEETSALU, P. et al. Residual stresses on various PVD hard coatings on tube and plate substrates. Coatings. 2020, 10(11), 1054. DOI: 10.3390/coatings10111054.
25. SERGEJEV, F., SURZENKOV, A., SAARNA, M. et al. Wear of different PVD coatings at industrial fine-blanking field tests. Materials Science (Medžiagotyra). 2015, 21(3), pp. 343–348. DOI: 10.5755/j01.ms.21.3.7249.
26. MORAČÍKOVÁ, J., MORAČÍK, R., KUSÝ, M. et al. Influence of laser surface texturing on tribological performance of tool steels. Journal of Materials Engineering and Performance. 2018, 27, pp. 5417–5426. DOI: 10.1007/s11665-018-3607-0.
27. PANJAN, M. et al. Surface topography of PVD hard coatings. Coatings. 2021, 11(11), 1387. DOI: 10.3390/coatings11111387.
28. DRNOVŠEK, A. et al. Surface roughness and its effect on adhesion and tribological performance of magnetron sputtered nitride coatings. Coatings. 2024, 14(8), 1010. DOI: 10.3390/coatings14081010.

Application possibilities of ultrasonic testing for quality control of resistance spot welds in the automotive industry

Ján Viňáš[1,*], Marie Kolaříková[2], Ladislav Kolařík[2]
Technical University of Košice, Faculty of Mechanical Engineering, Košice, Slovakia[1]
Czech Technical University in Prague, Faculty of Mechanical Engineering, Prague, Czech Republic[2]
jan.vinas@tuke.sk

Abstract: *This study investigates the application possibilities of ultrasonic testing for quality control of resistance spot welds used in the automotive industry. Experimental resistance spot welds were produced on galvanized DP600 and H420LAD steel sheets using different welding current values. The weld quality was evaluated by metallographic analysis, EDX surface analysis and several ultrasonic testing approaches, including automatic C-scan evaluation and manual A-scan interpretation. The obtained ultrasonic results were correlated with metallographic observations and macrostructural characteristics of welded joints to assess the sensitivity of ultrasonic methods for detecting weld imperfections and evaluating weld nugget formation. The results confirmed that welding current significantly influences weld geometry, weld nugget formation and the occurrence of internal defects. Among the samples investigated, the most acceptable weld quality was achieved at a welding current of 7.6 kA for both investigated steel grades. The study also demonstrated the potential of advanced ultrasonic testing methods for rapid and reliable non-destructive inspection of resistance spot welds in automotive manufacturing.*
Keywords*: RESISTANCE SPOT WELDING; ULTRASONIC TESTING; C-SCAN; DP600 STEEL; H420LAD STEEL; NON-DESTRUCTIVE TESTING*

1. Introduction

Resistance spot welding (RSW) is one of the most widely used joining technologies in modern manufacturing industries. Its importance is particularly evident in the automotive sector, where thousands of spot welds are used to join sheet metal components during the production of vehicle body structures. These welds represent key structural joints that directly influence the stiffness, strength and crashworthiness of the vehicle body [1-2]. A typical automotive body structure contains several thousand resistance spot welds connecting sheet metal components (Fig. 1). Because a single vehicle may contain several thousand welds, maintaining consistent weld quality is essential for ensuring the reliability and safety of the final product. In industrial practice, the quality of resistance spot welds is usually evaluated through parameters such as weld nugget diameter, mechanical strength and the occurrence of internal defects. Traditionally, destructive testing methods, including peel tests, tensile tests or chisel tests, have been used to verify the integrity of welded joints. Although these techniques provide reliable information about joint strength, their application in mass production is limited because the tested components must be destroyed. For this reason, significant attention has been devoted to the development and implementation of non-destructive testing (NDT) techniques capable of evaluating weld quality without damaging the inspected structure [3-4].

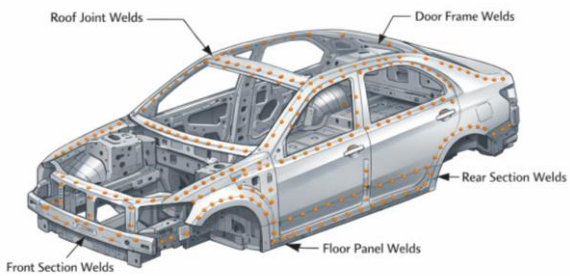


Fig. 1. *Distribution of resistance spot welds in a typical automotive body structure.*

Among the available NDT techniques, ultrasonic testing (UT) has become one of the most commonly used methods for the inspection of resistance spot welds. The method utilizes high-frequency acoustic waves that propagate through the welded joint and reflect from material interfaces or internal discontinuities. By analysing these reflected signals, it is possible to detect defects such as cracks, porosity, lack of fusion or insufficient weld nugget formation [5-6]. Compared with other inspection techniques, including radiographic testing, eddy current inspection or infrared thermography, ultrasonic testing offers a favourable balance between detection capability, penetration depth and practical applicability in industrial environments. Previous studies indicate that ultrasonic testing, together with radiography and infrared thermography, belongs among the few NDT methods capable of detecting the majority of typical resistance spot welding defects [7-8]. Despite its advantages, the ultrasonic inspection of spot welds is not without difficulties. The weld region is relatively small and consists of multiple overlapping layers of sheet material with a welded nugget formed between them. Such geometry can complicate the propagation of ultrasonic waves and make signal interpretation more demanding. As a result, the reliability of the inspection may depend on several factors, including probe positioning, coupling conditions, signal attenuation or the experience of the operator performing the measurement [9-10]. To overcome these limitations, recent research has focused on improving both the hardware and the data processing methods used in ultrasonic inspection systems. Advanced techniques such as C-scan imaging or phased-array ultrasonic testing allow a more detailed visualization of weld geometry and internal structures. These methods provide improved capability for evaluating weld nugget dimensions and identifying internal defects that may not be easily detectable using conventional ultrasonic inspection approaches [11-12]. Another significant research direction is the application of artificial intelligence and machine learning algorithms for the analysis of ultrasonic inspection data. These approaches enable automated interpretation of complex ultrasonic signals and support real-time monitoring of weld quality directly during the welding process. By analysing large datasets of measured signals, AI-based systems can recognize patterns related to specific types of weld defects, filter measurement noise and improve the accuracy of defect identification. As a consequence, the influence of operator subjectivity can be reduced and the reliability of automated inspection systems can be significantly improved [13-14]. Considering the growing demand for reliable quality assurance in high-volume industrial production, ultrasonic testing continues to represent an important tool for the non-destructive evaluation of resistance spot welds [15]. The aim of this study is to investigate the application possibilities of ultrasonic testing for the quality control of resistance spot welds and to evaluate the sensitivity of ultrasonic methods in detecting internal weld defects and determining the detectability limits of imperfections depending on their size and type.

2. Materials and experimental methods

Within the experimental work, the quality of weld joints produced by resistance spot welding was analyzed on various grades of double-sided galvanized steel sheets used in automotive body production. The evaluated weld joints were made on sheets of high-strength dual-phase steel DP600 with a nominal thickness of

0.9 mm, supplied in accordance with the requirements of EN 10338. The material was protected by an electrolytically deposited zinc coating (EG) with a coating weight of approximately 50 $g \cdot m^{-2}$, corresponding to a thickness of approximately 5 µm per side (designation ZE50/50). As a second base material, H420LAD steel, in accordance with EN 10268, was used. The material had a nominal thickness of 0.9 mm and was coated with an electrolytically deposited zinc layer (EG) with a thickness of approximately 7 µm per side (≈ ZE70/70).

Table 1. *Chemical composition of dual-phase steel DP600 (% Wt.) (Fe bal.)*

C	Si	Mn	P	S	Al	Nb	Cr	Ti	Mo
0,11	0,26	1,68	0,014	0,01	0,015	0,09	0,2	0,15	0,11

Table 2. *Mechanical properties of steel DP600*

Tensile strength [MPa]	Yield strength [MPa]	Elongation A80 [%]
600	330	20

Table 3. *Chemical composition of steel H420LAD (% Wt.). (Fe bal.)*

C	Si	Mn	P	S	Al	Nb	V	Ti
0,1	0,03	1,5	0,025	0,01	0,015	0,09	0,2	0,15

Table 4. *Mechanical properties of steel H420 LAD*

Tensile strength [MPa]	Yield strength [MPa]	Elongation A80 [%]
590	480	18

The resistance spot welding process was performed using a programmable pneumatic resistance spot welding machine VTS BP 20. Welding electrodes with CuCr electrode caps were used during the experiments. CuCr welding electrode caps with a tip diameter of 6 mm were used for all welding experiments. The electrode geometry and welding conditions were selected according to common industrial practice for welding galvanized automotive steel sheets.

For the DP600 steel sheets, the welding current varied in the range from 6.0 kA to 8.0 kA (samples A-E), while for the H420LAD steel sheets the welding current ranged from 6.6 kA to 8.0 kA (samples F-I). In all experiments, a constant welding time of 14 periods and a constant electrode force of 2.6 kN were maintained. The investigated welds included both acceptable weld joints and welds containing intentionally generated imperfections such as insufficient fusion, excessive electrode indentation, localized porosity and unstable weld nugget formation. Different welding current levels were selected in order to simulate various welding conditions occurring in automotive manufacturing practice.

Table. 5: *Parameters of resistance spot welding*

Samples	**Welding Current (kA)**	**Welding Time (periods)**	**Electrode Force (kN)**
A	6,0	14	2,6
B	6,6	14	2,6
C	7,0	14	2,6
D	7,6	14	2,6
E	8,0	14	2,6
F	6,6	14	2,6
G	7,0	14	2,6
H	7,6	14	2,6
I	8,0	14	2,6

As part of the metallographic analysis, the surface of the contact areas on the sheet surfaces was also examined using light microscopy performed on a Tesla BS 301 electron microscope, while the chemical EDX analysis was carried out by point analysis using a Jeol 10000 chemical analyzer.

An ultrasonic inspection system Matrixeye VI with automatic C-scan evaluation, manufactured by Toshiba, was used for the experimental measurements. Imagel R03-GEL1 was applied as the coupling medium between the ultrasonic probe and the tested samples. The software automatically evaluates the weld quality as either OK (acceptable) or NOK (unacceptable) according to predefined evaluation criteria.

In addition to the Matrixeye VI system, ultrasonic measurements were also compared with the Tessonics RSWA F2 ultrasonic system operating with automatic evaluation based on an inscribed circle method. The system utilized a 15 MHz ultrasonic probe and automatically evaluated weld quality according to the measured weld nugget diameter and indentation depth.

Manual ultrasonic evaluation was additionally performed using an Olympus EPOCH 650 device equipped with a straight-beam ultrasonic probe. In this case, A-scan signals were manually interpreted by an experienced operator in order to evaluate weld integrity and detect the presence of internal imperfections. Unlike automatic C-scan systems, the A-scan method strongly depended on operator experience and signal interpretation.

The obtained ultrasonic results were subsequently compared with metallographic analyses and destructive evaluation methods in order to verify the sensitivity and reliability of the applied ultrasonic testing approaches.

Examples of the applied ultrasonic evaluation methods are shown in Fig. 2. The approaches investigated included automatic C-scan evaluation using diagonal measurement, automatic weld evaluation based on the inscribed circle method and manual interpretation of A-scan signals.

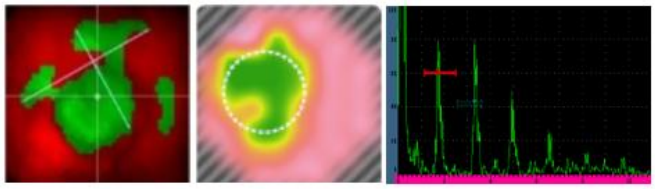


Fig. 2. *Examples of ultrasonic evaluation methods used for resistance spot weld inspection: automatic C-scan evaluation using diagonals (left), inscribed circle evaluation (center), and manual A-scan interpretation (right) [16].*

3. Results and discussion

3.1 Metallographic evaluation of welds

The macrostructures of the investigated resistance spot welds produced on DP600 steel sheets are shown in Figs. 3–5. The welds were produced using different welding current values to evaluate the influence of welding parameters on weld formation and weld quality.

Weld A produced at a welding current of 6 kA is shown in Fig. 3. The weld exhibits insufficient weld nugget formation and the presence of visible internal discontinuities, indicating inadequate heat input during the welding process. Such weld morphology may negatively influence the mechanical properties and load-bearing capacity of the joint.

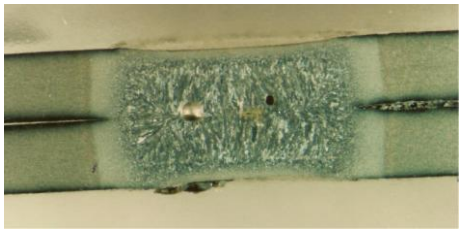


Fig. 3. *Macrostructure of Weld A produced at a welding current of 6 kA.*

Weld D, shown in Fig. 4, demonstrated the most acceptable weld morphology among the samples investigated. The weld nugget exhibited relatively uniform geometry and a stable fusion zone without pronounced macroscopic defects. The weld area appeared continuous and symmetrical, indicating suitable welding conditions for the investigated DP600 steel sheets.



Fig. 4. *Macrostructure of Weld D produced at a welding current of 7.6 kA.*

The macrostructure of Weld E produced at the highest welding current of 8 kA is shown in Fig. 5. Excessive heat input caused visible degradation of the weld region and irregularities near the electrode indentation. The results indicate that increasing the welding current does not necessarily lead to improved weld quality. On the contrary, excessive current may contribute to weld metal expulsion, surface degradation and the formation of internal defects.

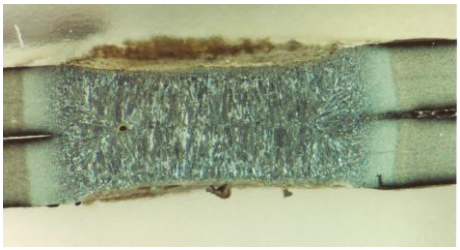


Fig. 5. *Macrostructure of Weld E produced at a welding current of 8.0 kA.*

Overall, the experimental results confirmed that the welding current significantly influences weld nugget formation, weld geometry and the occurrence of welding imperfections in DP600 steel sheets. An optimal range of welding parameters is therefore essential for achieving stable weld quality and reliable mechanical performance of resistance spot welded joints.

The macrostructures of the investigated resistance spot welds produced on H420LAD steel sheets are shown in Figs. 6–8. The welds were produced using different welding current values to evaluate the influence of welding current on weld nugget formation and overall weld quality.

The macrostructure of Weld F produced at a welding current of 6.6 kA is shown in Fig. 6. The weld exhibited insufficient fusion between the joined sheets and visible imperfections in the central part of the weld nugget. Small cavities and localized discontinuities were observed in the weld region, indicating inadequate heat input during the welding process. The observed imperfections were probably associated with the presence of Zn coating residues and unstable melting conditions in the contact region between the galvanized sheets and the welding electrodes. The weld nugget exhibited limited dimensions and non-uniform morphology, which may negatively affect the mechanical properties of the welded joint.

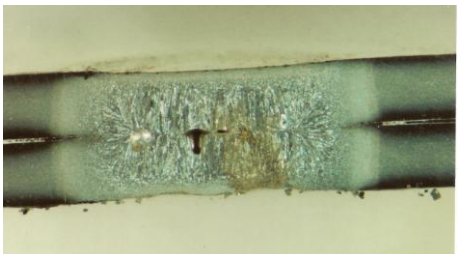


Fig. 6. *Macrostructure of Weld F produced at a welding current of 6.6 kA.*

The macrostructure of Weld H produced at a welding current of 7.6 kA is shown in Fig. 7. This weld exhibited the most acceptable weld morphology among the samples investigated. The weld nugget was continuous and symmetrical without significant macroscopic defects. Only minor local imperfections were observed in the transition regions between the weld nugget and the heat-affected zone. The results indicate that the selected welding current provided suitable thermal conditions for stable weld formation in H420LAD steel sheets.

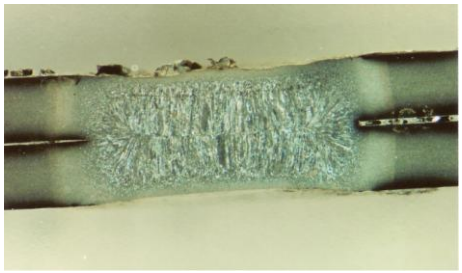


Fig. 7. *Macrostructure of Weld H produced at a welding current of 7.6 kA.*

The macrostructure of Weld I produced at the highest welding current of 8.0 kA is documented in Fig. 8. Increasing the welding current resulted in excessive heat input, leading to significant weld nugget growth and visible surface deformation in the region beneath the electrode indentation. The weld nugget exhibited the largest width and height among all investigated samples. Local surface irregularities and indications of weld metal expulsion were observed near the weld region. These features indicate overheating of the weld area and excessive melting of material under the electrodes.

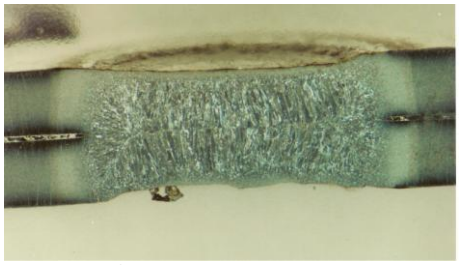


Fig. 8. *Macrostructure of Weld I produced at a welding current of 8.0 kA.*

Based on the performed metallographic analysis, it can be concluded that the welding current significantly affected weld nugget formation, weld geometry and the occurrence of welding imperfections. Under the applied welding conditions, including a welding time of 14 periods and electrode force of 2.6 kN, the most suitable weld quality was achieved at a welding current of 7.6 kA.

3.2 Surface and EDX analysis

Figure 9 shows the surface of sample C in the center of the electrode indentation. Numerous chemical analyses were performed on the surfaces of the samples tested in order to determine the precise chemical compositions, as documented in Fig. 9 for the presented sample C.

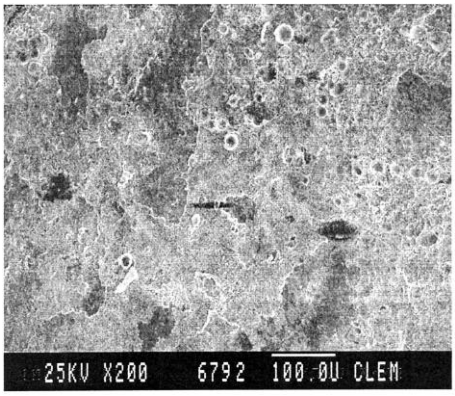


Fig. 9. *Surface of sample C in the center of the welding electrode indentation.*

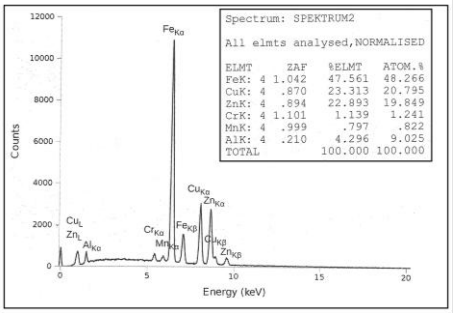


Fig. 10. *Result of EDX analysis on the surface of welded sample C.*

A point chemical analysis was performed on the surface of the welded joint. The presence of Fe and brass, i.e., a CuZn alloy, was identified on the sample surface. The presence of brass on the surface of the electrode indentation had already been observed during the visual inspection, while the EDX analysis only confirmed its occurrence.

The brass layer was formed as a result of Zn diffusion from the sheet coating into the contact surface of the welding electrode tip made of CuCr alloy. During resistance spot welding, the temperature in the weld area exceEDX 1300 °C. In the welding process, melting of the Zn coating first occurs at the contact interface between the electrode tip and the galvanized sheet at approximately 420 °C. The molten Zn adheres to the welding electrode tip, resulting in the formation of a thin brass layer on the contact surface of the electrode tip. At temperatures above 907 °C, Zn evaporation from the weld region occurs. However, due to the applied electrode force during the welding process, the evaporation of Zn from the weld area is partially suppressed. Part of the Zn adheres to the electrode tip, while another part penetrates into the base material. A significant portion of Zn is expelled from the weld area due to the dynamic effect of Zn vapors. EDX surface analyses also confirmed the presence of Cr, Mn, and Al. Chromium was present both as a strengthening alloying element in the Cu alloy of the electrode tips and as part of the chemical composition of the base material. Manganese originated from the base material composition. Aluminum was identified both as an alloying element used during the coating process of automotive steel sheets and as an alloying element in the base material, where it contributes to the stabilization of the investigated steel grade.

3.3 Ultrasonic testing evaluation of welds

Ultrasonic testing results confirmed a strong correlation between weld quality and the ultrasonic response obtained from the investigated welded joints. The automatic C-scan systems enabled rapid visualization of weld nugget geometry and identification of regions with unstable fusion or internal discontinuities.

Representative examples comparing ultrasonic C-scan evaluation, computed tomography and metallographic analysis are shown in Fig. 11. The comparison confirmed good correlation between ultrasonic signal response and the real weld nugget geometry observed by destructive and tomographic methods.

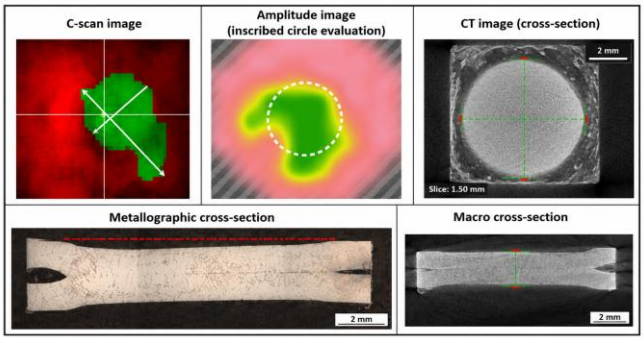


Fig. 11. *Comparison of ultrasonic C-scan evaluation (left), inscribed circle evaluation (center), CT image (top right), metallographic section (bottom left) and macro cross-section (bottom right) for a selected resistance spot weld [16].*

Welds produced using lower welding current values exhibited irregular ultrasonic indications and reduced weld nugget dimensions. In several cases, the ultrasonic systems classified these welds as NOK due to insufficient weld nugget formation and unstable signal response. These observations were consistent with the metallographic analyses, where incomplete fusion and localized imperfections were observed.

The most stable ultrasonic response was obtained for welds produced at a welding current of 7.6 kA. The corresponding C-scan images exhibited continuous and symmetrical weld nugget areas with uniform signal distribution. These results correlated well with the metallographic observations, where the welds demonstrated acceptable weld morphology and stable fusion zones.

Welds produced using excessive welding current values showed irregular ultrasonic signal behavior caused by weld metal expulsion and excessive electrode indentation. In these cases, the automatic evaluation algorithms occasionally overestimated the weld nugget dimensions due to irregular signal reflections from the deformed weld region.

Comparison of the investigated ultrasonic evaluation approaches showed that automatic C-scan methods provide rapid weld quality assessment suitable for industrial in-line inspection. However, manual A-scan interpretation enabled more detailed identification of local imperfections and signal irregularities. The results indicate that combining automatic ultrasonic evaluation with operator-based signal interpretation may improve the reliability of resistance spot weld quality control.

The comparison of ultrasonic images with CT and metallographic observations confirmed that ultrasonic evaluation methods can identify changes in weld nugget geometry and internal weld discontinuities. Nevertheless, significant differences were observed between individual evaluation algorithms when determining the weld nugget diameter.

Figure 12 summarizes the weld nugget diameters determined using different ultrasonic testing evaluation approaches for selected weld imperfections.

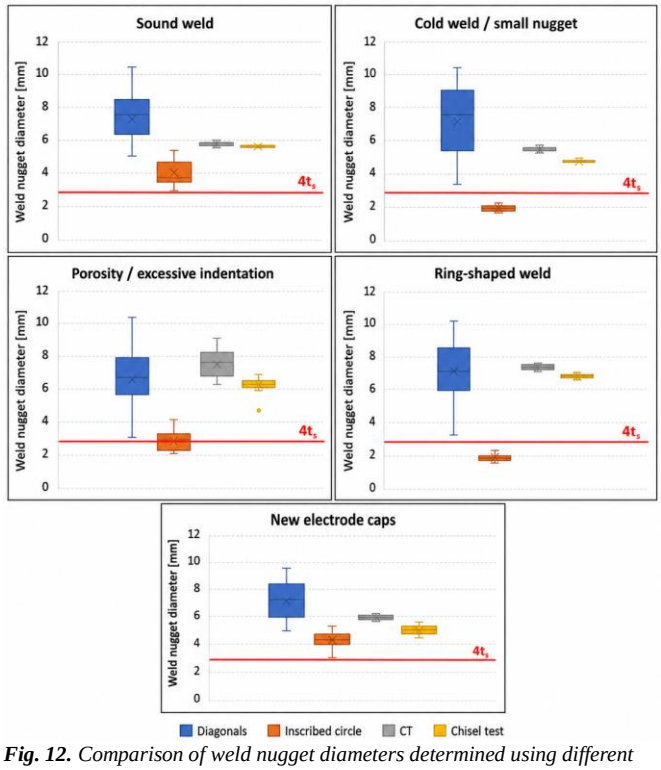


Fig. 12. *Comparison of weld nugget diameters determined using different ultrasonic testing evaluation methods for selected resistance spot weld imperfections [16].*

The red line shown in Fig. 12 represents the minimum acceptable weld nugget diameter according to the $4\sqrt{t}$ criterion commonly used for resistance spot weld evaluation. The results indicate noticeable differences between automatic C-scan evaluation methods and

destructive verification methods. The diagonal-based evaluation method tended to overestimate weld nugget dimensions, while the inscribed circle method provided more conservative results. The comparison also confirmed that manual evaluation and CT measurements provide more reliable information about internal weld quality and the presence of welding imperfections.

4. Conclusion

The presented study investigated the application possibilities of ultrasonic testing for the quality control of resistance spot welds produced on DP600 and H420LAD steel sheets commonly used in automotive body structures. The experimental results confirmed that welding current significantly affects weld nugget formation, weld geometry and the occurrence of welding imperfections. Metallographic analyses showed that insufficient welding current resulted in unstable weld formation and local discontinuities, while excessive welding current caused weld metal expulsion and surface degradation. For both investigated steel grades, the most suitable weld morphology was achieved at a welding current of 7.6 kA under the applied welding conditions. The performed ultrasonic inspections demonstrated that ultrasonic testing represents an effective non-destructive method for evaluating resistance spot weld quality. Automatic C-scan evaluation methods enabled rapid weld assessment, while manual A-scan interpretation provided more detailed information about internal imperfections and signal behavior. The comparison of ultrasonic results with metallographic observations confirmed the capability of ultrasonic methods to detect variations in weld quality and internal defects. The obtained results indicate that advanced ultrasonic testing systems have significant potential for implementation in automotive production as reliable tools for rapid in-line quality control of resistance spot welds. The results obtained also demonstrated that ultrasonic testing can significantly reduce the need for destructive testing methods in high-volume automotive production. Future research will focus on the implementation of advanced automated ultrasonic evaluation systems for real-time industrial weld quality monitoring.

Acknowledgements

This research was supported by the Visegrad Fellowship Program No. 62610048 and No. 2610076, for which the authors express their gratitude. The authors also acknowledge the support of the Slovak Research and Development Agency (APVV) through the projects “Innovative Approaches to the Restoration of Functional Surfaces by Laser Surface Treatment” (APVV-20-0303) and “Integrity of Protective Multilayers under High-Temperature Exposure Conditions” (APVV-24-0381), the VEGA Scientific Grant Agency through the project “Possibilities of Applying Laser Additive Technologies in the Restoration of Functional Surfaces” (1/0597/23), and the KEGA Cultural and Educational Grant Agency through the project “Hybrid Education of Students for the Current NeEDX of the Automotive Industry” (024TUKE-4/2025).

5. References

1. D. Ulbrich, J. Moravec, M. Smrž, Ultrasonic inspection of resistance spot welds in automotive structures, **Materials 16**, 7029 (2023)
2. Y. Zhou, *Resistance Spot Welding of Steel Sheets*, Woodhead Publishing, Cambridge (2015)
3. A.F. Andreoli, A.P. Tschiptschin, S.D. Brandi, Correlation between peel test and real-time ultrasonic monitoring of spot weld quality, **Soldagem Inspec. 21**, 326–335 (2016)
4. W. Dai, Y. Huang, J. Liu, Online quality inspection of resistance spot welding using process signals, **J. Manuf. Syst. 63**, 226–236 (2022)
5. Z. Chen, J. Zhang, Y. Zhou, Ultrasonic nondestructive evaluation of resistance spot welds for zinc-coated steel sheets, **Ultrasonics 49**, 298–304 (2009)
6. P. Liu, Y. Zhang, X. Li, On-line measurement of nugget diameter in resistance spot welding using ultrasonic signals, **Measurement 223**, 113764 (2024)
7. L. Yang, H. Wang, Q. Li, Ultrasonic nondestructive testing of spot welds in automotive structures, **Sensors 24**, 4771 (2024)
8. Ó. Martín, A. Sánchez, J.M. Prado, Advances in quality control of resistance spot welding processes, **Metals 12**, 1810 (2022)
9. J. Buckley, Improvements in ultrasonic inspection of resistance spot welds, **NDT.net 13** (2008)
10. K. Nomura, T. Shibata, H. Sato, Non-contact ultrasonic measurement of weld nugget diameter in resistance spot welding, **Ultrasonics 130**, 106875 (2023)
11. J. Liu, H. Fujii, K. Nakata, Ultrasonic C-scan detection for stainless steel spot welds, **ISIJ Int. 54**, 1876–1883 (2014)
12. D. Ulbrich, M. Smrž, J. Moravec, Correlation between ultrasonic signals and mechanical properties of spot welds, **Materials 15**, 1704 (2022)
13. Y. Li, H. Zhang, Deep learning for ultrasonic defect detection in weld inspection, **NDT E Int. 118**, 102372 (2021)
14. S. Mohanty, A.K. Mishra, Machine learning applications in ultrasonic non-destructive evaluation, **Measurement 187**, 110315 (2022)
15. R. Blitz, G. Simpson, *Ultrasonic Methods of Non-Destructive Testing*, Springer, London (2016)
16. M. Kolaříková, J. Viňáš, L. Kolařík, M. Petřík, D. Stárek, Verification of sensitivity of different ultrasonic testing methods for resistance spot welds, Proc. **PROMATTEN** 2025, Prague (2025)

Comparative thermo-mechanical severity assessment of automotive brake discs under repeated braking cycles

Halil Demolli, Gezim Preniqi, Shkelzen Shabani
University of Prishtina, Prishtina, Kosovo
E-mail: halil.demolli@uni-pr.edu, gezim.preniqi@student.uni-pr.edu, shkelzen.shabani@uni-pr.edu

Abstract: *This paper presents a comparative finite element assessment of the thermo-mechanical severity of automotive brake discs for Mercedes-Benz A180, E220 and E350 under intensive and repeated braking cycles. Transient thermal and structural simulations were evaluated for 27 cases covering high-speed, interurban and urban braking profiles. Gray cast iron EN-GJL-250/G3000 was used as the disc material, while heat flux, convection and radiation were considered as thermal boundary conditions. Maximum temperature, heat flux, total elastic deformation and von Mises stress were normalised and combined through several severity-index scenarios. The results show that the repeated 120-0-120-0 km/h braking cycle is the governing condition for all vehicles. A180 reached the highest raw temperature, stress and deformation, while the equal-weight severity indices confirmed the same critical braking profile within each vehicle group. All cases remained below the selected thermal and mechanical limits.*

Keywords: BRAKE DISC, FEA, THERMO-MECHANICAL ANALYSIS, SEVERITY INDEX, VON MISES STRESS

1. Introduction

The brake disc is one of the main safety-related components in a passenger vehicle. During braking, the kinetic energy of the vehicle is converted into heat at the pad-disc interface. This creates a coupled thermal and structural problem because the temperature field, thermal gradients, elastic deformation and equivalent stress evolve at the same time. If the generated heat is not dissipated efficiently, brake fade, surface distortion, local cracking or accelerated wear may occur [1, 2, 11].

For this reason, finite element analysis is useful for thermo-mechanical evaluation of brake discs under transient thermal and structural loading [2,3]. Repeated braking is particularly important because the second braking event may start before the disc returns to the initial thermal state, which can increase heat accumulation and thermo-mechanical severity [1,11]. The present paper condenses a larger numerical study of three vehicle classes and proposes a normalized severity assessment based on maximum temperature, heat flux, total elastic deformation and von Mises stress. Recent regulatory and scientific references on brake wear emissions are used only to frame the future extension of the model [5–10].

Thermo-mechanical brake analysis is more demanding than purely thermal calculation because temperature is not only an output. It also becomes a structural load through thermal expansion. Non-uniform heating creates local expansion differences, and if these are constrained by disc geometry, hub contact or support conditions, additional thermal stresses appear. For gray cast iron discs, this coupled response is decisive because the material is widely used for its thermal conductivity and damping capacity, but it remains sensitive to local tensile stress and thermal gradients [2,3,11].

The contribution of this paper is not a new material model or a validated failure criterion; rather, it is a compact severity-based interpretation of a larger set of numerical results. Instead of presenting many individual ANSYS images, the paper reduces the response to comparable indicators: maximum temperature, maximum heat flux, total elastic deformation and equivalent von Mises stress.

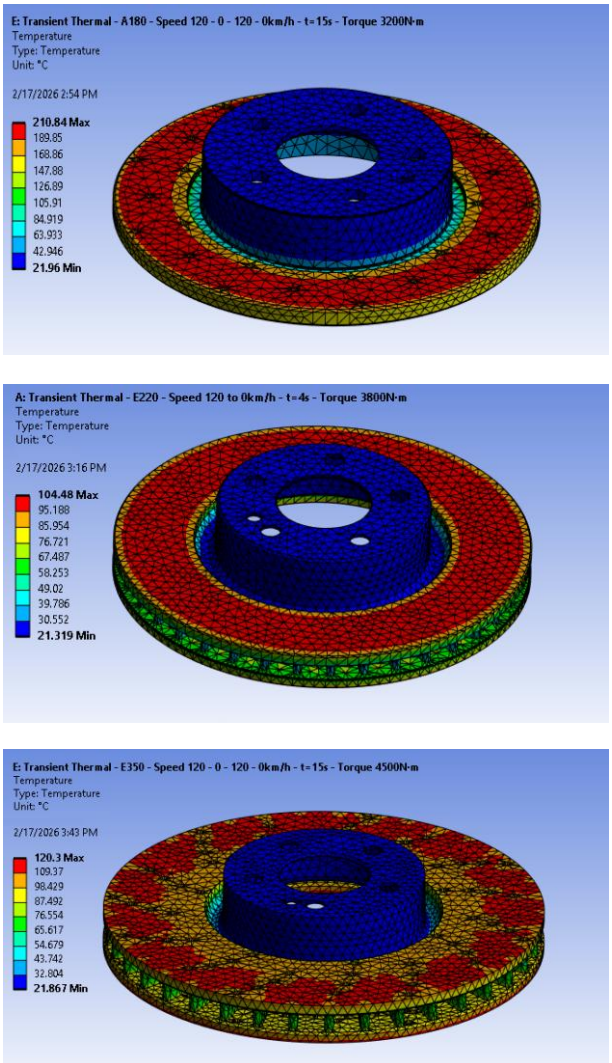


Fig. 1. Brake disc models for different vehicle types.

2. Material and methods

The cases examined are based on brake disc simulations for three models of Mercedes-Benz passenger vehicles: A180, E220 and E350. The numerical model considers 27 cases: nine braking scenarios for each vehicle. The scenarios include high-speed braking from 120 km/h, interurban braking from 80 km/h and urban repeated braking from 50 km/h. Each speed group contains emergency braking, progressive braking and repeated braking with a thermal recovery interval.

Table 1: *Condensed braking scenario matrix*

Group	Cases	Speed scenario	Time profile
High speed	1, 10, 19; 2, 11, 20 3, 12, 21	120 → 0; 120 → 0; 120→0→120→0	4 s; 12 s; 4+7+4 s
Interurban	4, 13, 22; 5, 14, 23 6, 15, 24	80 → 0; 80 → 0; 80 → 0 → 80 → 0	4 s; 12 s; 4+7+4 s
Urban	7, 16, 25 8, 17, 26 9, 18,27	50→0→50→0→50→0	5+10+5+10+5; 5+20+5+20+5; 5+30+5+30+5

The brake disc material is gray cast iron EN-GJL-250/G3000.

Table 2: *Main material data used in the FEM model*

Property	Value	Unit
Density	7200	kg/m^3
Young modulus	$1.1x10^5$	MPa
Poisson ratio	0.26	-
Thermal conductivity	52	$W/(m\cdot^0C)$
Specific heat	460	$J/(kg\cdot^0C)$
Adopted thermal reference temperature ~400 °C	~400	^0C

The use of one material model for the three vehicles allows a direct comparison of the influence of braking profile and disc configuration. The differences in the response can therefore be interpreted through the imposed thermal loading, heat dissipation capacity and structural stiffness rather than through changes in material constants.

The FEM workflow combines Transient Thermal and Static Structural analysis in ANSYS Workbench [3]. Heat flux is applied to the friction surface, while convection and radiation are used to represent heat dissipation from the disc surface. The obtained temperature field is then transferred to the structural model to evaluate total elastic deformation and equivalent von Mises stress.

The selected output quantities are engineering indicators. Maximum temperature identifies the risk of thermal overload and brake fade tendency. Heat flux represents the severity of the thermal input. Elastic deformation indicates the geometric response of the disc, while von Mises stress gives a compact measure of combined mechanical and thermal stress.

The braking process was treated as conversion of vehicle kinetic energy into heat at the pad-disc contact region. Equations (1)-(4) follow standard brake-energy balance, heat-partition and transient thermal FEM practice [1].

$$E_k = 0.5 \cdot m \cdot v_0^2 \quad (1)$$

where m is the vehicle mass and v_0 is the initial braking speed.

The heat absorbed by one disc was estimated through an energy-partition approach, in which the vehicle kinetic energy is distributed according to brake-force distribution, disc-side heat partition and contact-side distribution factors [1, 11, 12]:

$$Q_d = \lambda \cdot \alpha \cdot \beta \cdot E_k \quad (2)$$

where λ denotes brake-force distribution, α is the heat-partition factor to the disc, and β accounts for side/contact distribution.

The average thermal power is [1, 2]:

$$P_{avg} = Q_d / t_b \quad (3)$$

and the contact heat flux was calculated as [3, 11]:

$$q = P_{avg} / A_b \quad (4)$$

where tb is braking duration and Ab is the effective contact area.

For severity ranking, the simulation outputs were normalised using min-max normalisation within each vehicle group [13]:

$$X_n = (X - X_{min})/(X_{max} - X_{min}) \quad (5)$$

The following equal-weight SI formulation was considered [14]:

$$SI=(T_n+q_n+u_n+\sigma_n)/4 \quad (6)$$

The index is dimensionless and is used only for relative ranking of the simulated cases. It does not replace material strength verification or experimental validation.

3. Results and discussion

The complete set of 27 simulation cases is summarized in Table 3. The table presents the normalized values of maximum temperature, heat flux, elastic deformation and von Mises stress, together with the calculated severity index. This compact representation allows the thermo-mechanical response of the three brake-disc models to be compared under the same braking profiles. Instead of evaluating each output separately, the normalized results provide a clearer basis for identifying the most demanding operating conditions and for ranking the simulated cases according to their overall severity.

Table 3. *Raw FEM response values and equal-weight severity index*

Case	Veh.	T, °C	q, W/mm²	U, mm	σvM, MPa	SI
1	A180	128.920	1.050	0.159	106.550	0.596
2	A180	115.480	0.422	0.151	75.530	0.324
3	A180	210.840	1.070	0.280	161.740	1.000
4	A180	69.912	0.467	0.070	66.976	0.149
5	A180	64.057	0.191	0.070	55.327	0.038
6	A180	108.400	0.487	0.136	76.390	0.315
7	A180	67.600	0.171	0.070	51.580	0.030
8	A180	64.120	0.158	0.070	50.595	0.019
9	A180	61.370	0.152	0.060	50.036	0.000
10	E220	104.480	0.917	0.160	107.230	0.565
11	E220	82.751	0.300	0.149	88.178	0.226
12	E220	160.490	0.917	0.230	148.920	1.000
13	E220	58.775	0.400	0.130	96.152	0.191
14	E220	49.190	0.136	0.120	83.480	0.017
15	E220	83.600	0.408	0.158	97.520	0.316
16	E220	53.000	0.127	0.120	80.960	0.013
17	E220	51.490	0.127	0.119	80.950	0.007
18	E220	50.140	0.127	0.118	80.944	0.002
19	E350	82.300	0.674	0.160	104.020	0.653
20	E350	66.500	0.266	0.148	91.488	0.287
21	E350	120.300	0.675	0.200	115.450	1.000
22	E350	48.900	0.300	0.148	100.100	0.314
23	E350	42.040	0.119	0.132	88.824	0.071
24	E350	66.200	0.300	0.151	95.374	0.342
25	E350	44.300	0.093	0.126	84.469	0.012
26	E350	43.240	0.093	0.126	84.364	0.008
27	E350	42.300	0.093	0.125	84.300	0.001

The results confirm that repeated high-speed braking is the dominant severity condition for all three vehicles. The maximum values of temperature, heat flux, elastic deformation and von Mises stress occurred in cases 3, 12 and 21, corresponding to the repeated 120-0-120-0 km/h braking cycle. This is consistent with the heat build-up mechanism: the second braking event starts while the disc still stores heat from the first event.

The normalized severity index also confirms that the repeated high-speed cycle is the most severe case within each vehicle group. However, because the normalization was performed within each vehicle group, the SI values should be interpreted as relative rankings inside each vehicle category. Therefore, cross-vehicle comparison should be based on the raw response values reported in the table.

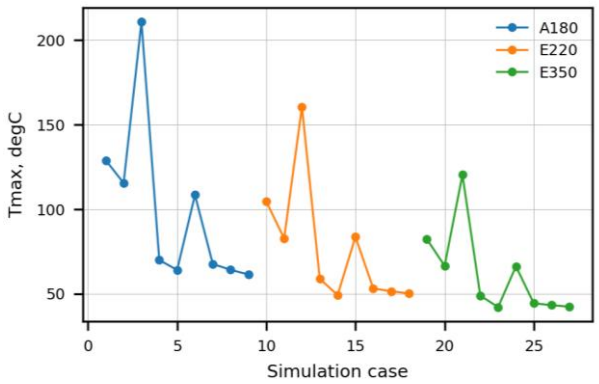


Fig. 2. *Maximum disc temperature over the full set of 27 simulation cases*

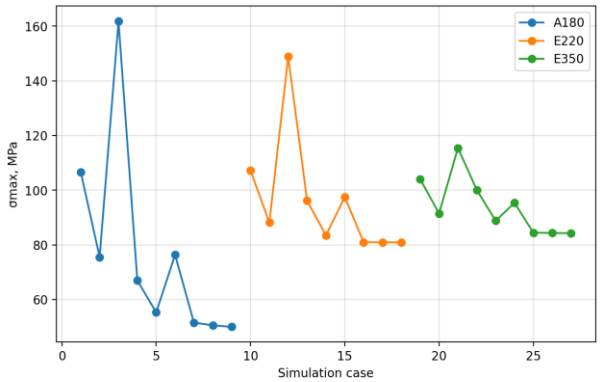


Fig. 3. *Maximum equivalent stress over the full set of 27 simulation cases*

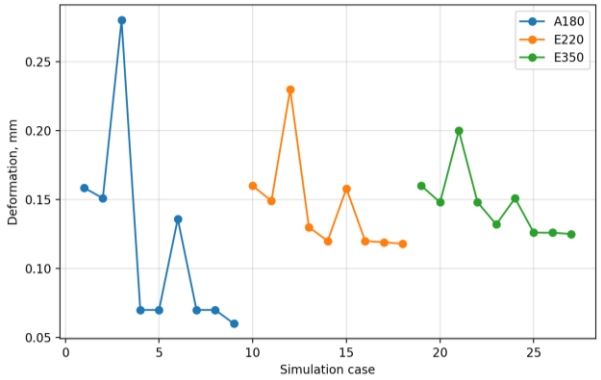


Fig. 4. *Maximum elastic deformation over the full set of 27 simulation cases*

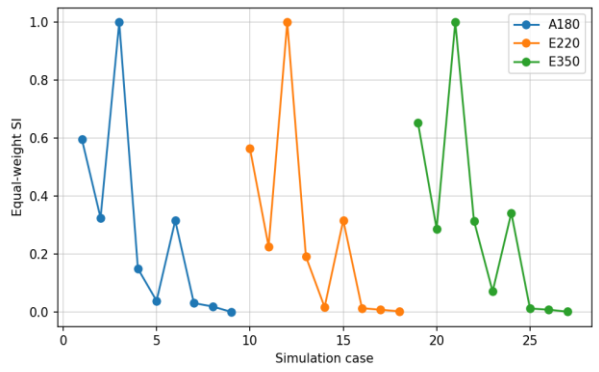


Fig. 5. *Equal-weight four-parameter severity index over the full set of simulation cases*

The high-speed regime shows the strongest contrast between emergency, progressive and repeated braking. For A180, changing from a single 120-0 km/h stop in 4 s to the repeated 120-0-120-0 profile increases the maximum temperature from 128.90 ^{0}C to 210.85 ^{0}C. For E220, the same change increases the maximum temperature from 104.48 ^{0}C to 160.49 ^{0}C, while for E350 it increases from 82.36 ^{0}C to 120.38 ^{0}C. This confirms that repeated braking is more critical than braking time alone.

In the interurban 80 km/h regime, the repeated cases again produce the highest temperature within each vehicle group, but the absolute values are substantially lower than in the 120 km/h regime. The A180 repeated 80 km/h case reaches 108.41 ^{0}C, E220 reaches 83.65 ^{0}C and E350 reaches 66.20 ^{0}C. These results are consistent with the kinetic energy relation, since the energy to be dissipated decreases with the square of speed.

In the urban 50 km/h repeated regime, the influence of recovery interval becomes visible. The cases with longer recovery time have lower maximum temperature, especially for A180. This is a useful design observation because it shows that thermal accumulation during frequent low-speed braking may be controlled by cooling opportunity between stops, even when each individual stop is not severe.

Table 4: *Critical thermo-mechanical response for each vehicle*

Vehicle	Case	Tmax, ^{0}C	q, W/mm^2	u, mm	σvM, MPa
A180	3	210.85	1.070	0.280	161.74
E220	12	160.49	0.917	0.230	148.92
E350	21	120.38	0.675	0.200	115.45

The A180 reached the highest maximum temperature, 210.85 °C, together with the highest von Mises stress, 161.74 MPa, and the largest elastic deformation, 0.280 mm. The corresponding values for E220 were 160.49 °C, 148.92 MPa and 0.230 mm, while the E350 critical repeated high-speed case reached 120.38 °C, 115.45 MPa and 0.200 mm. These values show that the thermal and mechanical severity is not controlled by vehicle class alone. Disc diameter, effective thermal capacity, exposed cooling area and heat-flux distribution strongly influence the final response.

Using 400 °C as an adopted conservative thermal reference for the gray cast iron brake disc, the critical A180 case reaches approximately 52.7% of this reference value, while E220 and E350 reach 40.1% and 30.1%, respectively. This comparison provides an additional absolute thermal-utilization indicator, but it should not be interpreted as a failure-temperature assessment.

The stress results follow the same severity ordering in the repeated high-speed cases: A180 > E220 > E350. The numerical results indicate that the equivalent von Mises stresses remain within the elastic structural range considered in the model. Therefore, the simulated cases do not suggest plastic deformation under the analysed loading conditions. However, thermal cracking and fatigue-related damage were not directly modelled and should be addressed in future experimental or coupled fatigue analyses.

The urban repeated cycles show much lower thermal severity. For A180, the urban temperature maximum varies from 61.37 °C to 67.60 °C; for E220, from 50.14 °C to 53.08 °C; and for E350, from 42.30 °C to 44.30 °C. Increasing the recovery interval from 10 s to 30 s reduces the accumulated temperature, especially in A180, while the changes in stress and deformation are smaller. This indicates that the cooling interval mainly affects the thermal field, whereas the local structural response also depends on geometry and support constraints.

Table 5. *Mean thermo-mechanical response for each vehicle*

Vehicle	Tmax, ^{0}C	q, W/mm^2	u, mm	σvM, MPa
A180	98.97	0.463	0.118	77.19
E220	77.12	0.384	0.145	96.04
E350	61.80	0.290	0.146	94.26

The average temperature response decreases from A180 to E350, whereas the average von Mises stresses for E220 and E350 remain close to each other and are higher than the average A180 stress. This non-proportional relationship between thermal and structural response is important, because it shows that brake-disc performance cannot be assessed from temperature response alone. A meaningful design comparison must consider the coupled thermo-mechanical behavior, including heat input, heat dissipation, elastic deformation and stress distribution.

Because the SI values were calculated using normalized response parameters within each vehicle group, they are used for relative ranking of braking cases inside the same vehicle category. Cross-vehicle comparison should therefore be based on the raw FEM

response values, particularly maximum temperature, heat flux, deformation and von Mises stress.

4. Conclusion

A comparative thermo-mechanical severity assessment of automotive brake discs was developed for Mercedes-Benz A180, E220 and E350 using 27 FEM simulation cases. The analysis leads to the following conclusions.

First, repeated high-speed braking from 120-0-120-0 km/h is the most critical condition for all vehicles. Second, A180 shows the highest absolute peak response among the analysed cases, with T_{max} = 210.84 °C, σ_{vM} = 161.74 MPa and u = 0.280 mm. Third, E220 and E350 show lower peak thermal response in the same repeated braking cycle, which confirms the influence of disc geometry, thermal capacity and cooling surface. Fourth, all simulated peak temperatures remain below the adopted conservative thermal reference temperature, while the stresses remain within the elastic structural range reported by the numerical model. Therefore, no plastic deformation or thermal-structural failure is expected for the scenarios investigated. Finally, the proposed SI scenarios provide a compact way to rank braking duty cycles and show that the ranking is stable under both equal-weight. The added reference framework also shows how the FEM outputs can later be linked to Archard wear modelling and EMEP/EEA emission-factor estimates, without claiming measured wear or PM emissions in the present paper.

5. References

1. Limpert R. Brake Design and Safety. SAE International, Warrendale, 2011.
2. Belhocine A., Bouchetara M. Thermomechanical modelling of dry contacts in automotive disc brake. International Journal of Thermal Sciences. 2012;60:161-170.
3. ANSYS Inc. Ansys Mechanical User's Guide: Transient Thermal and Static Structural Analysis. Canonsburg, PA: ANSYS Inc.; 2024.
4. FE analysis of the brake pad and brake disc wear with thermal-structure interaction. Wear. 2025;582-583:206331. doi:10.1016/j.wear.2025.206331.
5. UNECE. UN Global Technical Regulation No. 24: Laboratory Measurement of Brake Emissions for Light-Duty Vehicles. United Nations Economic Commission for Europe; 2023.
6. EMEP/EEA. Air Pollutant Emission Inventory Guidebook 2023: Road Transport, Tyre and Brake Wear. European Environment Agency; 2023.
7. European Parliament and Council. Regulation (EU) 2024/1257 on Euro 7 emission standards, 2024.
8. Grigoratos T., Mathissen M., Vedula R. T., Giechaskiel B., et al. Interlaboratory study on brake particle emissions - Part I: Particulate matter mass emissions. Atmosphere. 2023;14(3):498.
9. Mathissen M., Grigoratos T., Lahde T., Vogt R., et al. Interlaboratory study on brake particle emissions - Part II: Particle number emissions. Atmosphere. 2023;14(3):424.
10. Storch L., Hamatschek C., Hesse D., Feist F., Bachmann T., Eichler P., Grigoratos T. Comprehensive analysis of current primary measures to mitigate brake wear particle emissions from light-duty vehicles. Atmosphere. 2023; 14(4):712. doi:10.3390/atmos14040712.
11. Meresse D., Harmand S., Siroux M., Watremez M., Dubar L. Experimental disc heat flux identification on a reduced scale braking system using the inverse heat conduction method. Applied Thermal Engineering. 2012;48:202-210.
12. Yevtushenko A., Topczewska K., Zamojski P. The heat partition ratio during braking in a functionally graded friction couple. Materials. 2022;15(13):4623. doi:10.3390/ma15134623.
13. Vafaei N., Ribeiro R. A., Camarinha-Matos L. M. Normalization techniques for multi-criteria decision making: Analytical Hierarchy Process case study. In: Camarinha-Matos L. M., et al., editors. Technological Innovation for Cyber-Physical Systems. IFIP Advances in Information and Communication Technology, vol. 470. Cham: Springer; 2016. p. 261-269. doi:10.1007/978-3-319-31165-4_26.
14. Hwang C. L., Yoon K. Multiple Attribute Decision Making: Methods and Applications - A State-of-the-Art Survey. Lecture Notes in Economics and Mathematical Systems, vol. 186. Berlin: Springer-Verlag; 1981. doi:10.1007/978-3-642-48318-9.

Implementation of Composite Materials into the Design of an Experimental Vehicle for the Shell Eco-Marathon Competition

Štefan Kender*, Štefan Novotný

1 Technical University of Košice, Faculty of Mechanical Engineering, Department of Automotive Production, Mäsiarska 74, 040 01 Košice, Slovakia

* Correspondence: stefan.kender@tuke.sk

Abstract:. *The current optimization of materials in the automotive industry is primarily driven by the objective of progressively reducing vehicle curb weight, which serves as a critical instrument for lowering greenhouse gas emissions and enhancing energy efficiency. Empirical data demonstrate a direct correlation between weight reduction and fuel consumption: a 10% decrease in vehicle mass generates an approximate 7% reduction in fuel consumption. Composite materials, defined as heterogeneous systems consisting of at least two components—a continuous matrix (binder) and a discontinuous reinforcement (fibers, particles, or layers)—enable a synergistic effect of mechanical properties that are unattainable with monolithic metallic materials. In structural applications, polymer matrices (including both thermosets and thermoplastics) predominate in combination with high-strength carbon, aramid, or glass fiber reinforcements. These material systems exhibit extreme specific strength, a high modulus of elasticity, fatigue resistance, and anisotropic properties that allow for the directional optimization of stiffness. For components requiring maximum dimensional stability and self-supporting (monocoque) capabilities, sandwich configurations are utilized, typically integrating an aramid honeycomb core between high-performance composite face sheets. The qualitative parameters of the resulting components are directly dependent on the chosen manufacturing technology and the fiber-to-resin ratio. The Vacuum Infusion (VI) method represents a highly efficient process in which a vacuum-sealed mold ensures the uniform saturation of dry reinforcement with liquid resin. This procedure minimizes porosity, achieves a high fiber volume fraction—reaching up to 70% in advanced systems—and guarantees high production reproducibility and surface quality without the need for secondary machining. Despite their technical superiority, the primary limiting factors for widespread implementation remain the high economic cost of raw materials and the complexity of manufacturing cycles. Prospective development is focused on streamlining processes for mass production, implementing sustainable bio-fibers as reinforcing components, and addressing the challenges of recyclability and component replacement at the end of the life cycle. Advanced composite structures thus form the essential material foundation for the next generation of ultra-lightweight and safe transport vehicles.*

KEYWORDS: *COMPOSITE MATERIALS, MATRICES, FILLER, SANDWICH COMPOSITE, ARAMID HONEYCOMB, CARBON FIBERS.*

1. Introduction

Weight reduction and improvement of aerodynamic properties are among the key objectives of modern automotive engineering. Carbon fibre reinforced polymer matrix composites (CFRP) enable the design of lightweight yet stiff structural components that cannot be achieved using conventional metallic materials at the same mass [1]. These materials are characterised by exceptional specific stiffness and strength, excellent corrosion resistance and favourable fatigue properties [2, 8].

The Shell Eco-Marathon (SEM) is an international competition for vehicles with extremely low fuel consumption. In its current organised form it has been held since 1985, encompassing the Prototype and UrbanConcept categories on three continents [6]. The Faculty of Mechanical Engineering at TUKE has actively participated in SEM since 1994. Previous models were built from steel tubular frames with plastic body panels (total mass 45–55 kg). The new Prototype 2025 replaced the frame with a self-supporting sandwich composite monocoque body with the aim of significantly reducing mass and aerodynamic drag.

.2. Aerodynamic design and cfd analysis

2.1 Body Shape Optimisation

The body design was carried out in the CATIA V5/R16 CAD environment. The primary requirement was minimum aerodynamic drag while complying with the SEM competition regulations [6] and driver dimensional requirements. Through iterative optimisation of seven shape variants, the final form was selected – a streamlined body with an elliptical cross-section and an elongated rear section inspired by a teardrop aerodynamic profile.

2.2 CFD Flow Simulation

Aerodynamic evaluation of the shape variants was carried out by numerical CFD (Computational Fluid Dynamics) flow simulation. The steady-state simulation was solved by the finite volume method in the CATIA V5/R16 flow module with a computational domain of 2.5×10^{6} cells. Parameters: air ($\rho = 1.225$ kg/m³, $\mu = 1.789 \times 10^{-5}$ Pa·s), $v_\infty = 11$ m/s, Aref = 0.142 m². The velocity distribution around the body is shown in Fig. 1 – significant acceleration occurs over the upper surface, and a low-pressure wake forms behind the body.

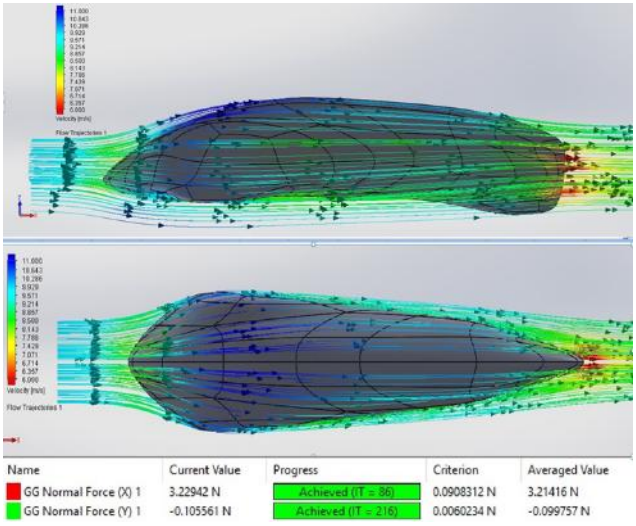


Fig. 1 Velocity streamlines around the Prototype 2025 body – CFD simulation ($v_\infty = 11$ m/s)

The CFD simulation results are summarised in Tab. 1. The drag force was determined from $FD = \frac{1}{2} \cdot \rho \cdot v^2 \cdot Cd \cdot Aref$. For Prototype 2025 at v = 30 km/h: $FD = 0.5 \times 1.225 \times 8.33^2 \times 0.092 \times$

0.142 = 0.56 N, corresponding to only 25.2 % of the drag force of the previous model (FD,old = 2.22 N).

Tab. 1 Comparison of aerodynamic characteristics

Parameter	Prev. model	Prototype 2025
Drag coeff. Cd [–]	0,26	0,20
Frontal area Aref [m²]	0,142	0,142
Drag force v=30 km/h [N]	2,22	0,56
Inlet velocity v∞ [m/s]	11,0	11,0

3. Composite sandwich structure

3.1 Material Components

The Prototype 2025 body is a sandwich composite structure. The outer and inner CFRP skins consist of a carbon twill 2/2 woven fabric (200 g/m², biaxial orientation [0°/90°]) with a vacuum infusion epoxy matrix [1]. A hybrid interlayer of woven CF/aramid fabric (sandwich mid-plane) increases toughness and impact energy absorption [4]. The core is an aramid Nomex® honeycomb (cell size 9.5 mm, ρc = 48 kg/m³), providing high bending stiffness at minimum mass [3, 11].

Tab. 2 Mechanical properties of sandwich material components

Material	E [GPa]	σ_u [MPa]	ρ [kg/m³]	thk./ply [mm]
CFRP fabric twill 2/2, 200 g/m²	62	560	1 520	0,28
Hybrid CF/aramid, 240 g/m²	45	420	1 380	0,30
Aramid Nomex® honeycomb, 48 kg/m³	–	3,2*	48	6,00
Epoxy matrix (VI system)	3,5	85	1 200	–

3.2 Sandwich Lay-up and Fibre Volume Fraction

The sandwich laminate is designed symmetrically about the core, thereby preventing deformations caused by the coupling effect [1, 2]. Detailed ply sequence, thicknesses and fibre volume fraction Vf are given in Tab. 3. The average Vf = 52.6 % achieved by the VI process significantly exceeds hand lay-up (Vf ≈ 30–40 %) and directly correlates with improved specific mechanical properties [9].

Tab. 3 Lay-up of the Prototype 2025 body sandwich structure

Layer	Material	thk. [mm]	N vrs.	Vf [%]
Outer skin (top)	CFRP fabric	0,84	3	55,1
Hybrid interlayer	CF/aramid fabric	0,60	2	48,6
Sandwich core	Aramid Nomex® honeycomb	6,00	–	–
Inner skin (bottom)	CFRP fabric	0,84	3	54,2
Total thickness	–	8,28	–	52,6 (Ø)

4. Manufacturing – vacuum infusion (vi)

Vacuum Infusion technology was used to manufacture both body components (chassis section and top cover). The dry reinforcement was placed in a rigid polyester mould, the mould was sealed with an airtight film, and liquid epoxy resin was drawn through a distribution network into the reinforcement under vacuum ($p \leq -0.95$ bar) [9]. Infusion rate ≈ 0.8 m²/h at p = −0.93 bar. Cure: 24 h at 23 °C, post-cure 4 h at 60 °C.

The VI process provided: Vf > 50 %, porosity < 1 %, repeatable quality and a closed manufacturing process with no VOC emissions. Body mass: mcar = 7.8 kg.



Fig. 2 Mould preparation and placement of CFRP reinforcement fabrics prior to infusion



Fig. 3 Manufacturing of the chassis section by Vacuum Infusion

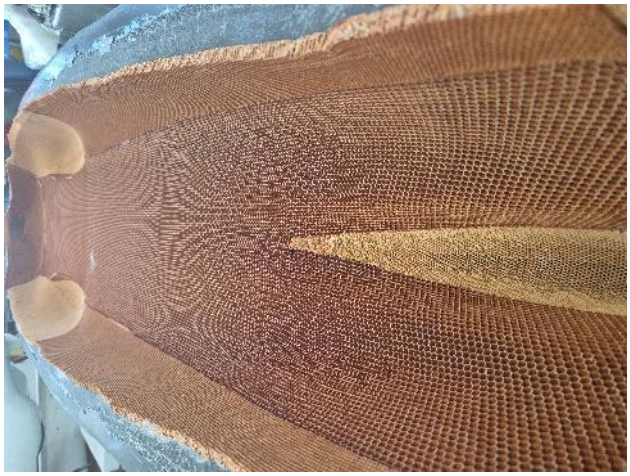


Fig. 4 Bonding of aramid honeycomb into the sandwich structure

5. Numerical structural analysis (ansys)

5.1 Finite Element Model

The structural integrity of the chassis section was verified by FEA in ANSYS Mechanical 2024 R1. The geometry (STEP from CATIA V5) was modelled using 3D shell elements SHELL281 (8-node, quadratic) with orthotropic material lay-up definitions according to Tab. 2 and 3 [12]. Mesh: global element size 4 mm, refined to 2 mm at axle attachments. Total elements: 186 452, nodes: 312 668.

5.2 Boundary Conditions and Loading

Constraint points: four axle attachments + two engine mounts (all translational DOFs fixed, rotations free). Loading: self-weight (g = 9.81 m/s²), driver load mdriver = 65 kg → F = 637 N applied as pressure on the seat surface, dynamic factor fd = 2.5 (road unevenness). Total design load: Fdesign = 1 600 N.

5.3 Numerical Analysis Results

FEA results are given in Tab. 4. The maximum von Mises equivalent stress σmax = 52.8 MPa occurs in the CFRP skin at the front axle attachment. Safety factor SF = σ_u□/σmax = 650/52.8 = 12.3 – a significant structural margin. Core safety factor SF = τ_u/τmax = 1.72/0.38 = 4.5. Maximum deflection δmax = 2.1 mm over the chassis length of 1 460 mm corresponds to a relative deflection of L/δ ≈ 695.

Tab. 4 FEA results for the chassis section (ANSYS Mechanical 2024 R1)

Result quantity	Value	Unit
Max. von Mises stress σmax	52,8	MPa
Allowable stress CFRP σ_u□	650	MPa
SF – skin (σ_u□/σmax)	12,3	–
Max. core shear τmax	0,38	MPa
Honeycomb shear strength τ_u	1,72	MPa
SF – core (τ_u/τmax)	4,5	–
Max. deflection δmax	2,1	mm
Design load	1 600	N
Element count (SHELL281)	186 452	–
Node count	312 668	–



Fig. 5 Chassis section of the Prototype 2025 body after demoulding

6. Results and discussion

6.1 Overall Vehicle Parameters

The total vehicle mass including the powertrain (35 cm³, 1 kW), steering, wheels with ceramic bearings and safety components reached mtotal = 35 kg. Body mass decreased from 14.6 kg to 7.8 kg (−46.6 %) as a direct result of the transition to the sandwich composite monocoque.

6.2 Shell Eco-Marathon Europe 2025 Competition Results

The Prototype 2025 vehicle competed in the Prototype ICE – Gasoline category. The TUKE team achieved a best result of 825 km/l – a team historical record and an improvement of 25.4 % over the previous best result of 658 km/l. A summary comparison of parameters is given in Tab. 5.

Tab. 5 Parameter comparison of the previous model and Prototype 2025

Parameter	Prev. model	Prot. 2025
Total mass [kg]	40	35
Body mass [kg]	14,6	7,8
Drag coeff. Cd [–]	0,26	0,20
Drag force v=30 km/h [N]	2,22	0,56



Fig. 6 Prototype 2025 vehicle at Shell Eco-Marathon Europe 2025

The achieved result confirms that the combination of aerodynamic optimisation (CFD), low mass of the sandwich composite body (VI technology) and minimisation of rolling resistance (ceramic bearings) represents an effective approach to significantly improving the fuel efficiency of prototype vehicles [7, 10].

7. Conclusion

Based on the results achieved, the following conclusions can be drawn:

1. CFD body optimisation (CATIA V5) reduced Cd from 0.26 to 0.20
2. The sandwich body (CFRP / hybrid CF+aramid / aramid honeycomb, VI technology) achieved a mass of 7.8 kg – a reduction of 46.6 % while retaining full monocoque function.
3. Vacuum Infusion ensured Vf = 52.6 % (vs. ≈ 35 % for hand lay-up), achieving an optimum specific mechanical property ratio.

4. FEA in ANSYS (SHELL281) confirmed structural integrity: σmax = 52.8 MPa → SF = 12.3; δmax = 2.1 mm at a design load of 1 600 N.
5. Total vehicle mass: 35 kg (−32.7 % compared to the previous model)
6. The competition result of 825 km/l is the TUKE team historical record (an improvement of 25.4 % over the previous record of 658 km/l).

Future research will focus on shortening the VI production cycle, automating the infusion process and the use of bio-fibres and recyclable thermoplastic matrices in line with sustainability principles.

Acknowledgement

This paper was produced within the grant project KEGA 024TUKE-4/2025 – Hybrid Education of Students for the Current Needs of the Automotive Industry and project IVG-25-02 – Development and Manufacturing of an Experimental Composite Vehicle for Shell Eco-Marathon 2025.

References

[1] DANIEL, I.M., ISHAI, O.: Engineering Mechanics of Composite Materials. 2nd ed. Oxford University Press, New York, 2006. ISBN 978-0-19-515097-1.

[2] BARBERO, E.J.: Introduction to Composite Materials Design. 3rd ed. CRC Press, Boca Raton, 2018. ISBN 978-1-138-19680-9.

[3] VINSON, J.R.: The Behavior of Sandwich Structures of Isotropic and Composite Materials. Technomic Publishing, Lancaster, 1999. ISBN 978-1-56676-699-3.

[4] PARK, S.J.: Carbon Fibers. 2nd ed. Springer, Dordrecht, 2018. ISBN 978-981-13-0538-2. https://doi.org/10.1007/978-981-13-0538-2

[5] FONG, A. et al.: A review on the hybrid polymer composites comprising natural fibre and nanomaterial reinforcement. Journal of Composite Materials, 2025, vol. 59, no. 22, pp. 2615–2646. https://doi.org/10.1177/00219983251334861

[6] SHELL INTERNATIONAL LIMITED: Shell Eco-Marathon Official Rules 2025 – Chapter I. London, 2024. [Online]. [cited 15.03.2025]. Available at: https://www.shell.com/make-the-future/shell-ecomarathon/rules.html

[7] BUDINSKI, K.G., BUDINSKI, M.K.: Engineering Materials: Properties and Selection. 9th ed. Pearson Education, Upper Saddle River, 2010. ISBN 978-0-13-712842-6.

[8] VASILIEV, V.V., MOROZOV, E.V.: Advanced Mechanics of Composite Materials and Structural Elements. 3rd ed. Elsevier, Amsterdam, 2013. ISBN 978-0-08-098231-1.

[9] LOOS, A.C., SPRINGER, G.S.: Curing of Epoxy Matrix Composites. Journal of Composite Materials, 1983, vol. 17, no. 2, pp. 135–169. https://doi.org/10.1177/002199838301700205

[10] WIEDEMANN, J.: Leichtbau: Elemente und Konstruktion. 3rd ed. Springer, Berlin, 2007. ISBN 978-3-540-33656-5.

[11] HEXCEL CORPORATION: HexWeb® Aramid Fibre Honeycomb – Product Data Sheet. Stamford, 2023. [Online]. [cited 10.02.2025]. Available at: https://www.hexcel.com/user_upload/assets/datasheets/Honeycomb/7740.pdf

[12] ANSYS INC.: ANSYS Mechanical User's Guide, Release 2024 R1. Canonsburg, PA: ANSYS Inc., 2024.

Operation guidelines for proper arrangement of pumps in the marine steam propulsion system

Mrzljak Vedran[1], Prpić-Oršić Jasna[1], Jelić Maro[2], Baressi Šegota Sandi[3]
[1]Faculty of Engineering, University of Rijeka, Vukovarska 58, 51000 Rijeka, Croatia
[2]Maritime Department, University of Dubrovnik, Ćira Carića 4, 20000 Dubrovnik, Croatia
[3]Faculty of Informatics, Juraj Dobrila University of Pula, 52100 Pula, Croatia
E-mail: vedran.mrzljak@riteh.uniri.hr, jasna.prpic.orsic@riteh.uniri.hr, maro.jelic@unidu.hr, sandi.baressi.segota@unipu.hr

Abstract: *In this paper are investigated and presented the most influential operating parameters and the guidelines for proper arrangement of pumps in the condensing/feedwater heating system. The observed system operates in marine steam propulsion power plant. In the analyzed system operates three pumps: Condensate Pump (CP), Auxiliary Pump (AP) and FeedWater Pump (FWP). Considering all observed pumps, FWP is the dominant mechanical power consumer because it operates with the highest pressure difference and with the highest fluid mass flow rate. Used mechanical power and losses (energy and exergy) of all observed pumps are directly proportional to fluid mass flow rate through the pump - higher fluid mass flow rate through the pump will result with higher mechanical power used by pump and with higher losses (both energy and exergy) and vice versa. Energy and exergy efficiencies of the observed pumps have reverse proportional trends. The most influencing factor related to the pump efficiency (both energy and exergy) is the pump inlet pressure. Pump inlet pressure is directly proportional to the pump exergy efficiency, but simultaneously pump inlet pressure is reverse proportional to pump energy efficiency.*
KEYWORDS: PUMP ANALYSIS, PUMP ARRANGEMENT, OPERATION DYNAMICS, DEPENDENT VARIABLES, MARINE STEAM PROPULSION SYSTEM

1. Introduction

Pumps are inevitable components of any steam power plant or system [1]. At least two pumps (condensate pump and feedwater pump) must operate in the condensing/feedwater heating system of any steam power plant [2, 3]. Along with two mentioned ones, recent condensing/feedwater heating systems are complex ones and they usually have one or more additional auxiliary pump [4, 5].

Any condensing/feedwater heating system has a main goal to increase water temperature (as well as pressure) before it enters steam generator [6]. In such way can be obtained notable savings in a consumption of fuel used in steam generator [7]. Therefore, without pumps, such systems cannot be operable.

In the literature can be found analyses related to the entire condensing/feedwater heating system and guidelines for its proper operation [8, 9]. However, operation guidelines for proper arrangement of the pumps in that system are still missing.

In this paper are presented operation guidelines and the most influencing operating parameters which should be considered for proper pump arrangement in the condensing/feedwater heating system. The observed system and three pumps which operate in it are placed in marine steam propulsion power plant. The analysis will show relations between used mechanical power, efficiencies and losses (both energy and exergy) of all pumps and the operating parameters which have the dominant impact on them.

2. Pumps position in marine condensing/feedwater heating system and principle of their operation

Pumps observed in this paper are Condensate Pump (CP), Auxiliary Pump (AP) and FeedWater Pump (FWP) which operates in condensing/feedwater heating system of marine steam propulsion power plant, Fig. 1.

Along with the observed pumps, condensing/feedwater heating system is composed of two High Pressure Feedwater Heaters (HPFH1 and HPFH2) and with two Low Pressure Condensate Heaters (LPCH1 and LPCH2). Both High Pressure Feedwater Heaters get a steam for heating purposes from the High Pressure Cylinder (HPC) of the main turbine, while both Low Pressure Condensate Heaters get a steam for heating purposes from the Low Pressure Cylinder (LPC) of the main turbine. Between High Pressure Feedwater Heaters and Low Pressure Condensate Heaters is mounted Deaerator which get steam for heating and deaerating purposes from Intermediate Pressure Cylinder (IPC) of the main turbine. In addition, observed condensing/feedwater heating system has one additional auxiliary heater which collects all steam leakages from the entire plant and uses it for increasing water temperature before LPCH1.

CP collects condensate obtained in the main steam condenser and delivers it to the Deaerator, Fig. 1. AP is used for returning condensate obtained from heating steam to the main water line (all other heating steam condensate returns were performed by reducing condensate pressure using pressure reducing valves [10]). Finally, FWP takes water from the Deaerator, increase its pressure and delivers it through High Pressure Feedwater Heaters to the steam generator.

In Fig. 1 are also presented operating points on each pump inlet and outlet relevant for the analysis (for the CP relevant operating points are A and B, for AP relevant operating points are C and D, and for FWP relevant operating points are E and F).

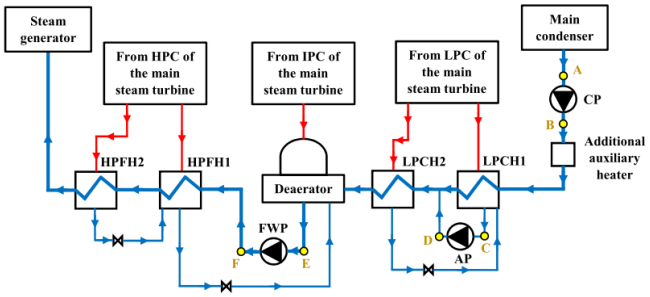


Fig. 1. *Pumps arrangement in the condensing/feedwater heating system of marine steam propulsion plant along with operating points required for the analysis*

For each of the observed pumps, in this paper is performed an energy analysis. Energy analysis of any pump is based on the comparison of ideal (isentropic) and real (polytropic) water pressure increase process. For the CP, both real and ideal pressure increase processes are presented in Fig. 2 (specific enthalpy-specific entropy diagram). For any other pump, the ideal and real pressure increase processes look the same like these in Fig. 2 (the only change occur in water operating parameters).

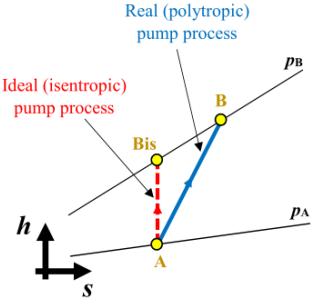


Fig. 2. *Ideal (isentropic) and real (polytropic) pressure increase process of condensate pump (CP) in h-s diagram*

Ideal (isentropic) pressure increase process neglects all the losses and water specific entropy remains always the same. Real (polytropic) pressure increase process considers the losses and water specific entropy increases, as presented in Fig. 2 [11].

Any pump consumes mechanical power for the pressure increase process. Due to neglecting all the losses which occur in the pressure increase process, in ideal process the same pump will consume the lowest possible mechanical power. In real exploitation, it is impossible to obtain an ideal process on any pump, but ideal process can and should be a guideline for losses reducing.

3. Equations for the energy analysis of pumps

Energy analysis of any system or component is based on the first law of thermodynamics [12, 13]. In an energy analysis exists some general equations and balances which should always be satisfied – they will be presented first, after which will be presented equations for the energy analysis of the specific pump.

3.1. General energy equations

The main energy balance equation valid for any system or component is [14]:

$$\dot{Q}_{\text{in}} + P_{\text{in}} + \sum \dot{E}n_{\text{in}} - \dot{Q}_{\text{out}} - P_{\text{out}} - \sum \dot{E}n_{\text{out}} - \dot{E}n_{\text{L}} = 0, \quad (1)$$

where $\dot{Q}$ is heat energy transfer, P is mechanical power, index in is related to the inlet (input), index out is related to outlet (output) and index L is related to loss. $\dot{E}n$ is a total energy flow of any fluid stream which is defined by an equation [15]:

$$\dot{E}n = \dot{m} \cdot h, \quad (2)$$

where $\dot{m}$ is mass flow rate and h is fluid specific enthalpy. If in the component or system did not occur fluid leakages, valid mass flow rate balance is [16]:

$$\sum \dot{m}_{\text{in}} = \sum \dot{m}_{\text{out}}. \quad (3)$$

General energy efficiency equation, valid for any system or component is [17]:

$$\eta_{\text{en}} = \frac{\text{CUMULATIVE ENERGY OUTPUT}}{\text{CUMULATIVE ENERGY INPUT}}. \quad (4)$$

3.2. Equations for the energy analysis of observed pumps

All equations for the energy analysis of the observed pumps are developed according to guidelines and recommendations from the literature [18-20]. The energy analysis equations will be presented for the Condensate Pump (CP) only, for other pumps the equations are the same (pressure increase processes are defined according to Fig. 2), but the operating points, presented in Fig. 1, for each pump differs. Different operating points for each pump denotes different pressures, temperatures and mass flow rates for each pump. Markings in the CP energy analysis equations are related to operating points from Fig. 1 and Fig. 2.

CP mass flow rate balance is:

$$\dot{m}_{\text{A}} = \dot{m}_{\text{B}} = \dot{m}_{\text{Bis}}. \quad (5)$$

Ideal (isentropic) mechanical power of CP which will be theoretically consumed is:

$$P_{\text{ID,CP}} = \dot{m}_{\text{A}} \cdot (h_{\text{Bis}} - h_{\text{A}}). \quad (6)$$

Real (polytropic) mechanical power consumed by CP is:

$$P_{\text{RE,CP}} = \dot{m}_{\text{A}} \cdot (h_{\text{B}} - h_{\text{A}}). \quad (7)$$

CP energy loss is:

$$\dot{E}n_{\text{L,CP}} = P_{\text{RE,CP}} - P_{\text{ID,CP}}. \quad (8)$$

Energy efficiency of CP is:

$$\eta_{\text{en,CP}} = \frac{P_{\text{ID,CP}}}{P_{\text{RE,CP}}}. \quad (9)$$

4. Fluid (water) operating parameters required for the analysis of all observed pumps

In each operating point for all observed pumps from Fig. 1, water operating parameters are found in [21] and presented in Table 1. It should be highlighted that in [21] were found water pressure, temperature and mass flow rate in each operating point of all observed pumps, other operating parameters are calculated by NIST-Refprop 9.0 software [22]. In Table 1 are presented operating parameters of the real (polytropic) pressure increase process in each pump.

As described before, ideal (isentropic) pressure increase process of each pump is the process between the same pressures, with the same fluid mass flow rates, but in such process is assumed that fluid specific entropy remains constant from the pump inlet until the pump outlet. For each observed pump, water operating parameters in ideal (isentropic) pressure increase process are presented in Table 2.

Table 1. *Water operating parameters at each pump inlet and outlet – real (polytropic) pressure increase process*

Pump	O.P.*	Temperature (K)	Pressure (kPa)	Mass flow rate (kg/s)	Specific enthalpy (kJ/kg)	Specific entropy (kJ/kg·K)
CP	**A**	305.88	5	10.947	137.15	0.47423
	B	305.92	520	10.947	137.78	0.47460
AP	**C**	358.93	60	1.491	359.29	1.14370
	D	358.98	520	1.491	359.86	1.14400
FWP	**E**	426.32	520	15.593	645.87	1.87390
	F	428.03	10300	15.593	659.20	1.88010

* O.P. = Operating point (refers to Fig. 1 and Fig. 2)

Table 2. *Water operating parameters at each pump inlet and outlet – ideal (isentropic) pressure increase process*

Pump	O.P.*	Pressure (kPa)	Mass flow rate (kg/s)	Specific enthalpy (kJ/kg)	Specific entropy (kJ/kg·K)
CP	**A**	5	10.947	137.15	0.47423
	Bis	520	10.947	137.66	0.47423
AP	**C**	60	1.491	359.29	1.14370
	Dis	520	1.491	359.75	1.14370
FWP	**E**	520	15.593	645.87	1.87390
	Fis	10300	15.593	656.53	1.87390

* O.P. = Operating point (refers to Fig. 1 and Fig. 2)

5. Results and obtained operation guidelines related to the arrangement of observed pumps

In Fig. 3 is presented mechanical power (both ideal and real) used by each observed pump in the marine condensing/feedwater heating system. As ideal (isentropic) pressure increase process of each pump neglects all the losses which occur during such process (neglects increase in water specific entropy), for each pump is obtained that mechanical power used in the ideal pressure increase process is lower in comparison to real pressure increase process.

From Fig. 3 can be derived several important conclusions. When comparing all observed pumps, FWP is the dominant mechanical power consumer because it operates with the highest pressure difference and with the highest fluid mass flow rate (the same conclusion is also valid for any other steam power plant [23, 24]). CP uses much lower mechanical power in comparison to FWP, while mechanical power used by AP can almost be neglected in comparison to other observed pumps. For AP this is an expected phenomenon because AP is the auxiliary pump which operates with the lowest pressure difference and the lowest fluid mass flow rate (in comparison to other observed pumps).

More important conclusion clearly seen in Fig. 3 is that mechanical power used by each of the observed pumps is directly proportional to fluid mass flow rate through the pump – higher fluid mass flow rate will require higher mechanical power for the pump

drive and vice versa. This conclusion is not valid for the observed pumps which operate in a marine steam propulsion system only – the same conclusion can be derived from various other steam power plants and systems [25, 26].

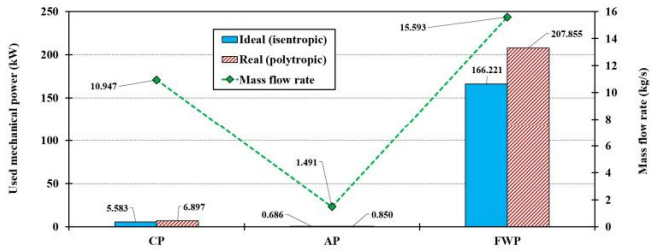


Fig. 3. *Ideal (isentropic) and real (polytropic) mechanical power used by pump in relation to fluid mass flow rate through the pump*

In Fig. 4 is presented energy and exergy losses of each observed pump in relation to fluid mass flow rate throughout the pump. It should be noted that in this paper is performed energy analysis (and consequentially is obtained energy loss of each pump), while the exergy analysis (and consequentially exergy loss of each pump) is performed in [21] from which the results are adopted. It is interesting to present both energy and exergy losses for all observed pumps in the same place, Fig. 4, because it can be clearly seen that regardless of the used analysis (energy or exergy) both losses will follow the same trend. The highest losses (both energy and exergy) are obtained for the FWP, followed by CP, while the lowest losses (again both energy and exergy) are obtained for the AP.

However, the more important conclusion from Fig. 4 is that pump losses (both energy and exergy) and fluid mass flow rate through the pump are directly proportional – higher fluid mass flow rate will result with higher losses and vice versa. The same conclusion is not valid for the observed pumps only, this conclusion can also be derived if other condensing/feedwater heating systems from various other steam power plants are observed [4, 5].

From Fig. 3 and Fig. 4 can be derived unique conclusion related to the observed pumps used mechanical power and losses – both used mechanical power and losses (energy and exergy) of the observed pumps are directly proportional to fluid mass flow rate through the pump. Higher fluid mass flow rate through the pump will result with higher mechanical power used by pump and with higher losses (both energy and exergy) and vice versa. Therefore, the fluid mass flow rate is the dominant parameter on which depends the amount of power used by the pump and pump losses.

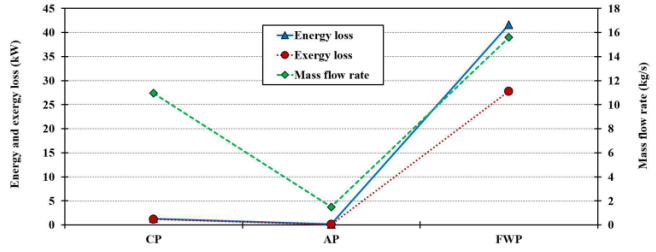


Fig. 4. *Pump energy and exergy loss in relation to fluid mass flow rate through the pump*

This analysis also considers which operation parameter is dominantly related to the efficiencies of the observed pumps (both energy and exergy efficiencies). Unlike fluid mass flow rate which is proportional to pump used mechanical power and losses, efficiencies (both energy and exergy) are proportional to the pump inlet pressure, Fig. 5. Again, exergy efficiency of each observed pump is taken from [21] where the exergy analysis is performed, while in this research is obtained energy efficiency of each pump.

From Fig. 5 can clearly be seen that energy and exergy efficiencies of the observed pumps have reverse proportional trends. In energy analysis is obtained that the highest energy efficiency (equal to 80.95%) has CP, followed by AP (80.70%) and the lowest energy efficiency has FWP (equal to 79.97%). In exergy analysis, CP has the lowest efficiency (equal to 82.86%), followed by AP (86.62%) while the highest exergy efficiency has FWP (equal to 86.63%).

Pump inlet pressure is directly proportional to the pump exergy efficiency (higher pump inlet pressure results with higher pump exergy efficiency and vice versa), but simultaneously pump inlet pressure is reverse proportional to pump energy efficiency (higher pump inlet pressure results with lower pump energy efficiency and vice versa). Such trends of both energy and exergy efficiency in relation to pump inlet pressure are characteristic of the observed pumps from marine condensing/feedwater heating system, such trends cannot be confirmed in other steam power plants.

Finally, this analysis confirms that the most influencing factor related to the pump efficiency is the pump inlet pressure, the trends between efficiencies of the pumps and pump inlet pressure require further research with an aim to obtain relations valid in general.

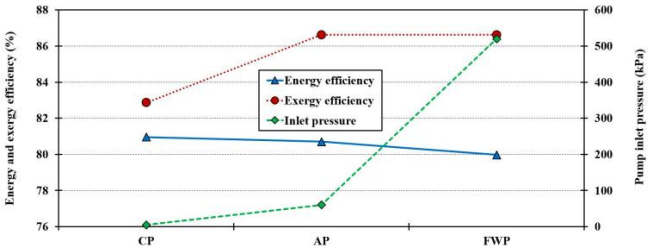


Fig. 5. *Pump energy and exergy efficiency in relation to the pump inlet pressure*

After finding the most influential operating parameters which has the dominant impact on the operation and arrangement of the pumps, it should be highlighted that a recent Artificial Intelligence (AI) methods allow optimization of operation (not only for the pumps but also for the entire condensing/feedwater heating system) [27-30].

6. Conclusions

In this paper are investigated and presented the most influential operating parameters and the guidelines for proper arrangement of pumps in the condensing/feedwater heating system. The observed system operates in marine steam propulsion power plant. In the analyzed system operates three pumps: Condensate Pump (CP), Auxiliary Pump (AP) and FeedWater Pump (FWP). The most important conclusions derived from this analysis are:

- As ideal (isentropic) pressure increase process of each pump neglects all the losses which occur during such process (neglects increase in water specific entropy), for any observed pump used mechanical power will be lower in ideal (isentropic) than in real (polytropic) pressure increase process.
- FWP is the dominant mechanical power consumer because it operates with the highest pressure difference and with the highest fluid mass flow rate. CP uses much lower mechanical power in comparison to FWP, while mechanical power used by AP can almost be neglected in comparison to other observed pumps.
- Used mechanical power and losses (energy and exergy) of the observed pumps are directly proportional to fluid mass flow rate through the pump. Higher fluid mass flow rate through the pump will result with higher mechanical power used by pump and with higher losses (both energy and exergy) and vice versa.
- Energy and exergy efficiencies of the observed pumps have reverse proportional trends. In energy analysis is obtained that the highest energy efficiency (equal to 80.95%) has CP, followed by AP (80.70%) and the lowest energy efficiency has FWP (equal to 79.97%). In exergy analysis, CP has the lowest efficiency (equal to 82.86%), followed by AP (86.62%) while the highest exergy efficiency has FWP (equal to 86.63%).
- The most influencing factor related to the pump efficiency (both energy and exergy) is the pump inlet pressure. Pump inlet pressure is directly proportional to the pump exergy efficiency (higher pump inlet pressure results with higher pump exergy efficiency and vice versa), but simultaneously pump inlet pressure is reverse proportional to pump energy efficiency (higher pump inlet pressure results with lower pump energy efficiency and vice versa).

- Some of the obtained relations and conclusions in this research have general validity, but the exact connection and trends between pump inlet pressure and pump efficiencies (both energy and exergy) requires further research.

7. Acknowledgment

This work was supported by the Croatian Science Foundation under the project number HRZZ-IP-2022-10-2821; University of Rijeka scientific grants: Funded by the European Union – NextGenerationEU – ENERGOPT - uniri-iz-25-6; GENE-CLASS - uniri-iz-25-220 and VEDRO - uniri-iz-25-10; SPIN projects IP.1.1.03.0120, IP.1.1.03.0028 and IP.1.1.03.0039; University North project UNIN-TEH-25-1-8; the EU NextGeneration under the Juraj Dobrila University of Pula institutional research project number IIP_010144 and IIP_010136; and the EC Digital Europe Programme EDIH Adria 101083838.

8. References

[1] Sutton, I. (2017). Plant design and operations. Gulf Professional Publishing

[2] Elhelw, M., Al Dahma, K. S., & el Hamid Attia, A. (2019). Utilizing exergy analysis in studying the performance of steam power plant at two different operation mode. Applied Thermal Engineering, 150, 285-293. (doi:10.1016/j.applthermaleng.2019.01.003)

[3] Kopac, M., & Hilalci, A. (2007). Effect of ambient temperature on the efficiency of the regenerative and reheat Çatalağzı power plant in Turkey. Applied Thermal Engineering, 27(8-9), 1377-1385. (doi:10.1016/j.applthermaleng.2006.10.029)

[4] Adibhatla, S., & Kaushik, S. C. (2014). Energy and exergy analysis of a super critical thermal power plant at various load conditions under constant and pure sliding pressure operation. Applied thermal engineering, 73(1), 51-65. (doi:10.1016/j.applthermaleng.2014.07.030)

[5] Ahmadi, G. R., & Toghraie, D. (2016). Energy and exergy analysis of Montazeri steam power plant in Iran. Renewable and Sustainable Energy Reviews, 56, 454-463. (doi:10.1016/j.rser.2015.11.074)

[6] Noroozian, A., Mohammadi, A., Bidi, M., & Ahmadi, M. H. (2017). Energy, exergy and economic analyses of a novel system to recover waste heat and water in steam power plants. Energy conversion and management, 144, 351-360. (doi:10.1016/j.enconman.2017.04.067)

[7] Mitrović, D., Zivkovic, D., & Laković, M. S. (2010). Energy and exergy analysis of a 348.5 MW steam power plant. Energy Sources, Part A: Recovery, Utilization, and Environmental Effects, 32(11), 1016-1027. (doi:10.1080/15567030903097012)

[8] Mrzljak, V., Lorencin, I., Anđelić, N., & Car, Z. (2021). Thermodynamic Analysis of a Condensate Heating System from a Marine Steam Propulsion Plant with Steam Reheating. Journal of Marine Science and Application, 20(1), 117-127. (doi:10.1007/s11804-021-00191-5)

[9] Naserabad, S. N., Mehrpanahi, A., & Ahmadi, G. (2019). Multi-objective optimization of feed-water heater arrangement options in a steam power plant repowering. Journal of Cleaner Production, 220, 253-270. (doi:10.1016/j.jclepro.2019.02.125)

[10] Mrzljak, V., Poljak, I., & Žarković, B. (2018). Exergy analysis of steam pressure reduction valve in marine propulsion plant on conventional LNG carrier. NAŠE MORE: znanstveni časopis za more i pomorstvo, 65(1), 24-31. (doi:10.17818/NM/2018/1.4)

[11] Mrzljak, V., Žarković, B., & Poljak, I. (2017). Energy and exergy analysis of sea water pump for the main condenser cooling in the LNG carrier steam propulsion system. Mathematical Modeling, 1(3), 144-147.

[12] Kanoğlu, M., Çengel, Y. A., & Dinçer, İ. (2012). Efficiency evaluation of energy systems. Springer Science & Business Media.

[13] Dincer, I., & Rosen, M. A. (2012). Exergy: energy, environment and sustainable development. Newnes.

[14] Poljak, I., Orović, J., Mrzljak, V., & Bernečić, D. (2020). Energy and exergy evaluation of a two-stage axial vapour compressor on the LNG carrier. Entropy, 22(1), 115. (doi:10.3390/e22010115)

[15] Mrzljak, V., Prpić-Oršić, J., & Poljak, I. (2018). Energy power losses and efficiency of low power steam turbine for the main feed water pump drive in the marine steam propulsion system. Pomorski zbornik, 54(1), 37-51. (doi:10.18048/2018.54.03)

[16] Aljundi, I. H. (2009). Energy and exergy analysis of a steam power plant in Jordan. Applied thermal engineering, 29(2-3), 324-328. (doi:10.1016/j.applthermaleng.2008.02.029)

[17] Mrzljak, V., Poljak, I., & Mrakovčić, T. (2017). Energy and exergy analysis of the turbo-generators and steam turbine for the main feed water pump drive on LNG carrier. Energy conversion and management, 140, 307-323. (doi:10.1016/j.enconman.2017.03.007)

[18] Erdem, H. H., Akkaya, A. V., Cetin, B., Dagdas, A., Sevilgen, S. H., Sahin, B., ... & Atas, S. (2009). Comparative energetic and exergetic performance analyses for coal-fired thermal power plants in Turkey. International Journal of Thermal Sciences, 48(11), 2179-2186. (doi:10.1016/j.ijthermalsci.2009.03.007)

[19] Mrzljak, V., Poljak, I., & Medica-Viola, V. (2017). Dual fuel consumption and efficiency of marine steam generators for the propulsion of LNG carrier. Applied Thermal Engineering, 119, 331-346. (doi:10.1016/j.applthermaleng.2017.03.078)

[20] Jahangiri, A., & Ameri, M. (2020). Interaction effects of natural draft dry cooling tower (NDDCT) performance and 4E (energy, exergy, economic and environmental) analysis of steam power plant under different climatic conditions. Sustainable Energy Technologies and Assessments, 37, 100599. (doi:10.1016/j.seta.2019.100599)

[21] Koroglu, T., & Sogut, O. S. (2018). Conventional and advanced exergy analyses of a marine steam power plant. Energy, 163, 392-403. (doi:10.1016/j.energy.2018.08.119)

[22] Lemmon, E. W., Huber, M. L., & McLinden, M. O. (2010). NIST Standard Reference Database 23, Reference Fluid Thermodynamic and Transport Properties (REFPROP), version 9.0, National Institute of Standards and Technology. R1234yf. fld file dated December, 22, 2010.

[23] Khanmohammadi, S., Azimian, A. R., & Khanmohammadi, S. (2013). Exergy and exergo–economic evaluation of Isfahan steam power plant. International Journal of Exergy, 12(2), 249-272. (doi:10.1504/IJEX.2013.053386)

[24] Ameri, M., Ahmadi, P., & Hamidi, A. (2009). Energy, exergy and exergoeconomic analysis of a steam power plant: A case study. International Journal of energy research, 33(5), 499-512. (doi:10.1002/er.1495)

[25] Poljak, I., Orović, J., & Mrzljak, V. (2018). Energy and exergy analysis of the condensate pump during internal leakage from the marine steam propulsion system. Pomorstvo, 32(2), 268-280. (doi:10.31217/p.31.2.12)

[26] Ameri, M., Mokhtari, H., & Bahrami, M. (2016). Energy, exergy, exergoeconomic and environmental (4E) optimization of a large steam power plant: a case study. Iranian Journal of Science and Technology, Transactions of Mechanical Engineering, 40(1), 11-20. (doi:10.1007/s40997-016-0002-z)

[27] Baressi Šegota, S., Lorencin, I., Anđelić, N., Mrzljak, V., & Car, Z. (2020). Improvement of marine steam turbine conventional exergy analysis by neural network application. Journal of Marine Science and Engineering, 8(11), 884. (doi:10.3390/jmse8110884)

[28] Lorencin, I., Anđelić, N., Mrzljak, V., & Car, Z. (2019). Genetic algorithm approach to design of multi-layer perceptron for combined cycle power plant electrical power output estimation. Energies, 12(22), 4352. (doi:10.3390/en12224352)

[29] Ebrahimgol, H., Aghaie, M., Zolfaghari, A., & Naserbegi, A. (2020). A novel approach in exergy optimization of a WWER1000 nuclear power plant using whale optimization algorithm. Annals of Nuclear Energy, 145, 107540. (doi:10.1016/j.anucene.2020.107540)

[30] Anđelić, N., Baressi Šegota, S., Lorencin, I., Poljak, I., Mrzljak, V., & Car, Z. (2021). Use of Genetic Programming for the Estimation of CODLAG Propulsion System Parameters. Journal of Marine Science and Engineering, 9(6), 612. (doi:10.3390/jmse9060612)

Mesh-Converged Modal Profile Assessment of Functionally Graded Spur Gears

Shkelzen Shabani[1,*], Halil Demolli[1]
University of Prishtina, Faculty of Mechanical Engineering, Prishtina, Kosovo[1]
shkelzen.shabani@uni-pr.edu

Abstract: *This study presents a mesh-converged finite element assessment of functionally graded spur gears. Two gear models are studied: a fully graded gear and a half-metal/half-graded gear. The material properties vary gradually from aluminum alloy to zirconia according to power-law distribution. The modal analysis is carried out in ANSYS using SOLID187 elements and the Block Lanczos method. A mesh-convergence study is performed, and a 0.25 mm mesh is adopted for the results. The study compares the natural frequencies and normalized mode-shape profiles of the two models. The results show how the material layout influences the vibration behavior of the gear.*
Keywords*: FUNCTIONALLY GRADED GEAR, FINITE ELEMENT ANALYSIS, MODAL ANALYSIS, NATURAL FREQUENCIES, MODE-SHAPE PROFILE, MESH CONVERGENCE*

1. Introduction

Gears are important parts of many mechanical transmission systems, and their vibration behavior has a direct effect on noise, reliability, and service life [1]. For lightweight applications, the choice of material is especially important, because reducing weight should not cause an unfavorable change in stiffness or natural frequencies.

Functionally graded materials offer a useful way to improve this balance. In these materials, the properties change gradually from one material to another, instead of changing suddenly at a sharp interface. For gears, this means that a lighter metallic region can be combined with a stiffer ceramic-rich region near the tooth surface.

Previous studies have shown that material gradation can affect the mechanical and dynamic response of rotating components and gears. Functionally graded discs have been investigated for stress, vibration, critical speed, and elastic behavior using analytical, numerical, and finite element approaches [2] [3] [4] [5] [6] [7]

More recently, finite element models have also been used to study stress, stiffness, weight reduction, and natural frequencies of intact and cracked functionally graded gears [8] [9] [10]. However, modal results are usually presented mainly through frequency values and general mode-shape contours.

In this article, functionally graded spur gears are studied using a mesh-converged finite element model. Two material layouts are compared: a fully graded gear and a half-metal/half-graded gear. The comparison is based on natural frequencies and normalized mode-shape profiles along a selected gear-tooth path. This gives a simple way to compare both the overall vibration response and the local bending-sensitive regions of the two gear models.

2. Materials and methods

2.1. Gear geometry and material gradation law

Two spur-gear models are considered in this work. The first model is a fully functionally graded gear, where the gear body is divided into 30 layers of equal thickness. The second model is a half-metal/half-graded gear, where the inner part is metallic and the outer part is divided into 15 graded layers (see Figure 1). In both models, the gradation follows the tooth profile and the material changes from aluminum alloy in the inner region to zirconia near the outer surface.

The material property P(r) is assigned according to the power-law relation:

$$P(r) = P_i + (P_0 - P_i)V_0(r) \quad (1)$$

$$V_0(r) = \left(\frac{r-R_i}{R_0-R_i}\right)^k, R_i \le r \le R_0, 0 \le k \le \infty \quad (2)$$

Here, P represents the material property, V_0 is the ceramic volume fraction, r is the radial coordinate, and R_i and R_o are the inner and outer radii of the graded region. The subscripts i and o refer to the metallic and ceramic phases, respectively. The parameter k is the gradation index.

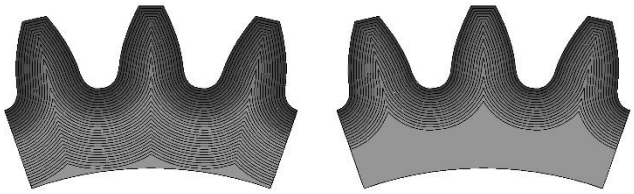


Fig. 1 *Spur gear models: (a) fully graded gear; (b) half-metal/half-graded gear.*

Table 1: *Gear parameters.*

Parameter	Value
Number of teeth	28
Module	3.1750
Pressure angle	20^o
Face width	5 mm

Table 2: *Material properties [11].*

Material	Elastic Modulus (GPa)	Density (kg/m3)	Poisson's ratio
Aluminum alloy	70	2700	0.3
Zirconia	200	5700	0.3

2.2. Finite element model and modal formulation

The gear geometry is prepared in KISSsoft using the selected gear parameters (see Table 1) and material properties (see Table 2). The model is then imported in Autodesk Inventor, creating multi-layer model. After that the model is imported in ANSYS for modal analysis. The three-dimensional finite element model is meshed using SOLID187 ten-node tetrahedral elements. The natural frequencies and mode shapes are extracted using the Block Lanczos eigen solver. The boundary conditions are used in that way to match the cantilever boundary conditions.

For the intact gear, the free-vibration eigenvalue problem is written as [10]:

$$[K - \omega^2 M]\Phi = 0 \quad (3)$$

where $[K]$ and $[M]$ are the global stiffness and mass matrices, ω is the natural angular frequency, and Φ is the corresponding mode-shape vector.

2.3. Mesh Convergence

A mesh-convergence study is carried out before comparing the two gear models. The percentage change between two consecutive mesh sizes is evaluated as :

$$\left|\frac{\Delta\omega}{\omega}\right|(\%) = \left|\frac{\omega_i - \omega_{i-1}}{\omega_i}\right| \times 100 \quad (4)$$

where:

ω_i - is the natural frequency on the finer mesh and ω_{i-1} is the natural frequency on the coarser mesh.

The mesh is refined until the first three natural frequencies show only negligible changes (see table 3). Based on this check, an element size of 0.25 mm is adopted for the final modal analysis.

Table 3: *Mesh-convergence results for the fully graded gear model.*

Elem, edge (mm)	ω_1 (kHz)	$\lvert\Delta\omega_1/\omega_1\rvert$ (%)	ω_2 (kHz)	$\lvert\Delta\omega_2/\omega_2\rvert$ (%)	ω_3 (kHz)	$\lvert\Delta\omega_3/\omega_3\rvert$ (%)
0.50	311.58	-	437.36	-	472.05	-
0.45	311.59	3.0 × 10-5	437.36	0	472.06	2.0 × 10-5
0.40	311.65	1.9 × 10-4	437.42	1.4 × 10-4	472.16	2.1 × 10-4
0.35	311.70	1.6 × 10-4	437.44	5 × 10-5	472.20	9 × 10-5
0.30	311.74	1.3 × 10-4	437.47	7 × 10-5	472.24	9 × 10-5
0.25	311.80	1.9 × 10-4	437.52	1.1 × 10-4	472.32	1.7 × 10-4
0.20	311.93	4.2 × 10-4	437.61	2.1 × 10-4	472.42	2.1 × 10-4
Max ($\lvert\Delta\omega/\omega\rvert$)		4.2 × 10-4				

3. Solution of the problem examined

The examined problem is solved by applying the mesh-converged finite element model to two gear configurations. The first configuration is a fully graded gear, while the second is a half-metal/half-graded gear. To reduce computational time, a three-tooth gear sector is used instead of the complete gear. The same sector geometry, boundary conditions, mesh size, element type, and modal extraction method are applied to both configurations, so that the effect of the material layout can be compared directly.

The natural frequencies and mode shapes are extracted using the Block Lanczos method. The results are then compared through the first three natural frequencies, the corresponding mode-shape contours and normalized mode-shape profiles. This procedure allows the global vibration response and the local bending-sensitive behavior of the two healthy gear models to be evaluated.

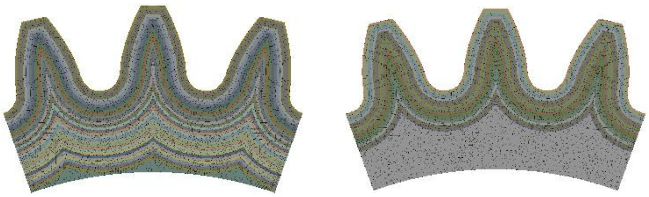


Fig. 2 *Finite element model of healthy gear: (a) fully graded gear; (b) half-metal/half-graded gear.*

4. Results and discussions

The modal results of the two healthy gear configurations are presented and compared in this section. The discussion is organized according to three aspects: natural frequencies and normalized mode-shape profiles. The aim is to show how the material layout affects both the global vibration response and the local bending-type behaviour of the gear tooth.

4.1. Natural frequencies

Figures 3–5 show the change of the first three natural frequencies with the power index *k* for the fully graded and half-metal/half-graded gear models. The value of *k*changes the amount of ceramic and metal in the graded part of the gear. For small values of *k*, the gear has more ceramic contribution near the outer region, so the stiffness is higher. When *k* increases, the gear becomes more metal-rich. Since aluminum alloy is less stiff than zirconia, the stiffness of the gear decreases. At the same time, the mass also decreases because aluminum has lower density than zirconia.

For the fully graded gear, the first natural frequency decreases from $k = 0.1$ to $k = 5$. In this range, the loss of stiffness has the main effect. For larger values of *k*, the first frequency increases slightly, because the reduction in mass starts to compensate for part of the stiffness loss. This effect is more visible in the first mode, which represents a more global vibration of the gear.

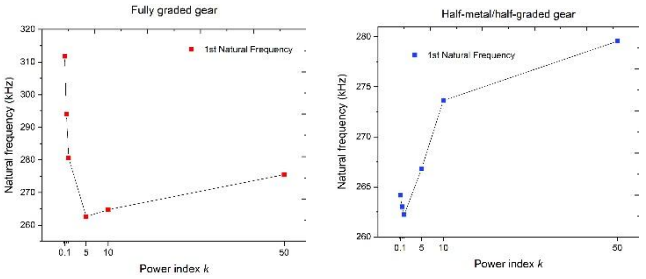


Fig. 3 *The effects of various power index (k) in the first natural frequency: a) Full graded gear; b) Half graded, half metal gear.*

The second and third natural frequencies of the fully graded gear decrease more strongly with increasing *k*. These modes have more complex deformation patterns and are more sensitive to stiffness changes. After $k = 10$, the curves become nearly stable, indicating that further changes in material distribution have a smaller influence.

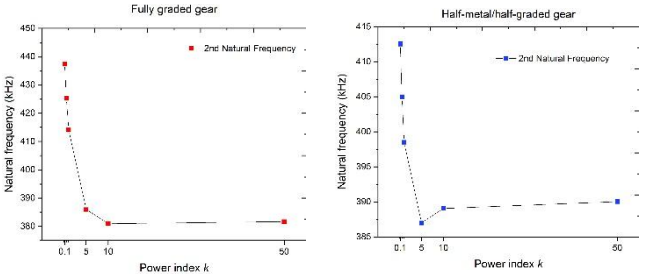


Fig. 4 *The effects of various power index (k) in the second natural frequency: a) Full graded gear; b) Half graded, half metal gear.*

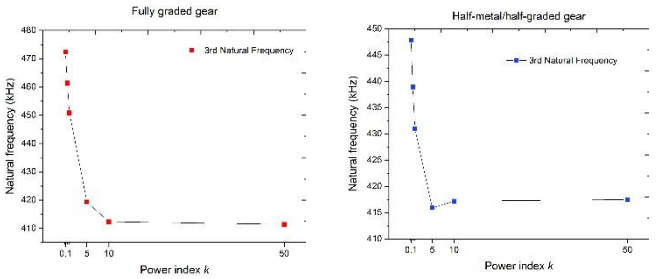


Fig. 5 *The effects of various power index (k) in the third natural frequency: a) Full graded gear; b) Half graded, half metal gear.*

For the half-metal/half-graded gear, the frequencies are generally lower than those of the fully graded model because a larger part of the structure is made of aluminum alloy, which reduces the overall stiffness. In the first mode, the frequency increases with *k*, as the mass reduction becomes more influential. For the second and third modes, the frequencies first decrease and then remain almost constant. Overall, the fully graded gear gives higher natural frequencies, while the half-metal/half-graded model shows a lower but more stable modal response at higher *k*.

4.2. Normalized mode-shape profiles

The directional deformation mode shapes of the fully graded and half-metal/half-graded gears are shown below (see Figure 6).

The deformation values were extracted along the central tooth path, from the root region to the tooth tip, using the same path for both gear models.

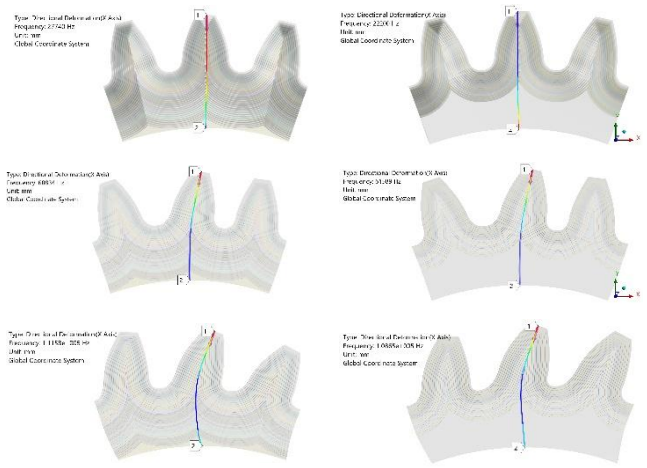


Fig. 6 *Mode shapes contours along the x axis: (a) fully graded gear; (b) half-metal/half-graded gear.*

As shown in Figure 7, the first mode has a smooth profile without a sign change, indicating a mainly global bending response. The second mode also follows a continuous trend, but with stronger curvature, showing greater sensitivity to the stiffness distribution along the tooth. In the third mode, the profile changes sign, meaning that different tooth regions deform in opposite directions. This indicates a more complex local bending behavior.

These results show that the two material layouts differ not only in natural frequencies, but also in deformation distribution. The fully graded gear shows a more pronounced higher-order bending response, especially in the third mode, while the half-metal/half-graded gear gives smoother normalized profiles. Therefore, Figures 6 and 7 confirm that material gradation affects both global modal behavior and the local tooth bending response.

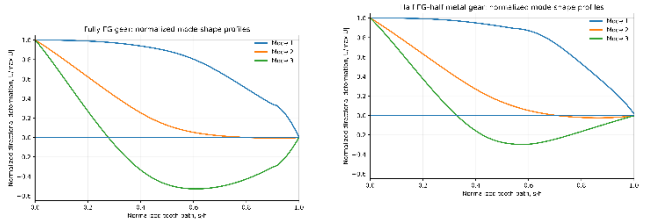


Fig. 7 *Normalized mode shapes along the x axis: (a) fully graded gear; (b) half-metal/half-graded gear.*

5. Conclusions

This study presented a mesh-converged finite element modal analysis of fully graded and half-metal/half-graded spur gears.

• The results show that the material layout plays an important role in the vibration behavior of the gear.

• The fully graded gear generally gives higher natural frequencies because it contains a larger ceramic-rich region, which increases the overall stiffness.

• The half-metal/half-graded gear gives lower natural frequencies, but its normalized mode-shape profiles are smoother and more stable.

• The normalized profiles show that material gradation affects not only the frequency values, but also how the tooth deforms along with its profile.

6. References

1. S. P. Radzevich, *Dudley's Handbook of Practical Gear Design and Manufacture* (2021).

2. M. Bayat, M. Saleem, B. B. Sahari, A. M. S. Hamouda, and E. Mahdi, Mech. Res. Commun. **35**, (2008).

3. E. Bagheri and M. Jahangiri, Int. J. Appl. Mech. **11**, 1950020 (2019).

4. J. N. Sharma, D. Sharma, and S. Kumar, International Journal for Computational Methods in Engineering Science and Mechanics **14**, (2013).

5. Ö. C. Farukoğlu, I. Korkut, and A. Motameni, ZAMM Zeitschrift Fur Angewandte Mathematik Und Mechanik **103**, (2023).

6. R. Madan, P. Khobragade, and S. Bhowmick, Multidiscipline Modeling in Materials and Structures **20**, 1192 (2024).

7. H. Callioglu, S. Muftu, and C. N. Koplay, Multidiscipline Modeling in Materials and Structures **21**, 98 (2024).

8. B. Singh, R. S. Mulik, and S. P. Harsha, Mechanics Based Design of Structures and Machines **51**, (2023).

9. B. Singh, R. S. Mulik, and S. P. Harsha, Proceedings of the Institution of Mechanical Engineers, Part L: Journal of Materials: Design and Applications **237**, (2023).

10. S. Shabani, F. Idrizi, R. Morina, E. F. Erdurcan, and H. Demolli, Proceedings of the Institution of Mechanical Engineers, Part D: Journal of Automobile Engineering **0**, 09544070251410619 (2026).

Traffic safety in Serbia and automotive industry today

Nataša Tomić-Petrović
Faculty of Transport and Traffic Engineering, University of Belgrade, Serbia
natasa@sf.bg.ac.rs

Abstract: *According to a new study by the most influential European consumer association BEUC, new mid-size electric vehicles will generally be cheaper to run than their petrol equivalents as early as 2026, while in 2025 "Sandero" became the best-selling car in Europe. Small city electric cars are forecast to be cheaper only from 2026. However, the EU is abandoning its plan to make all cars electric by 2035. "Ford" is radically reducing investments in electric vehicles - weak demand in the US is also cited.*
Chinese Technology giant Xiaomi is testing a factory of the future where humanoid robots are helping to assemble electric cars at a factory in Beijing. In November 2025, Peugeot changes the rules – the beginning of a new era for drivers - the square steering wheel!
It is interesting that the Chinese company Changan is entering the market of Serbia and the Western Balkans by launching the Deepal So5 and So7 models. These are electric SUV models, and in our city of Belgrade, test drives of these cars are already being scheduled.
In 2026 production of the "Grande Panda" with a gasoline engine has begun in Kragujevac.
In February 2026, the most urban electric car for 2025 was announced, and it was the Byd Dolphin Surf. It was also promoted in Belgrade, Serbia. Serbia was also the first country in Europe to sign an agreement with the American manufacturer of flying taxis, Archer Aviation. The first demonstration flights are expected in 2027, during the specialized exhibition EXPO.
Unfortunately, on our roads in Serbia we had the black month of March 2026. In the first 12 days of the third month, 19 people died in traffic accidents, most of them young people. Since the beginning of the year, 120 people have lost their lives in traffic accidents. (The Traffic Safety Agency).
How to prevent traffic tragedies in our country? Caution is essential for all road users. Smart radars should contribute to compliance with regulations. Recently, stationary radars were installed at a total of 30 "black spots". It is expected that they will significantly improve traffic safety.
Keywords*: TRAFFIC SAFETY, ELECTRIC CARS, ACCIDENTS*

1. Introductory considerations

In October 2025 French carmaker "Citroen" has ordered owners of the current C3 range to immediately stop using their vehicles due to a fault with the brake pedal assembly, and in the UK it affected around 1,100 vehicles. The so-called "stop-drive" recall is issued when there is a serious safety risk. The recall covered all models in the C3 range: the Citroen C3 (2025–), Citroen e-C3 (2024–), Citroen C3 Aircross (2025–) and Citroen e-C3 Aircross (2025–).

Customers of the affected models were offered replacement vehicles until the brake pedal assembly could be checked and repaired. According to an explanation from Stellantis, the owner of the Citroen brand, during regular quality checks it was discovered that certain right-hand drive models have a brake pedal manufactured outside specifications, which can lead to a complete loss of braking ability. However, they assured that the automatic emergency braking and electronic parking brake remained functional. In November 2025, the public learned that Stellantis had moved part of the Citroen-C3 production to Kragujevac.

In November 2025, "Peugeot" changes the rules – the square steering wheel represents the beginning of a new era for drivers!

In March 2026 BMW was recalling more than 360,000 vehicles (around 337,000 vehicles worldwide and 29,000 in Germany, across 5 different models, potentially affected by a fire risk – linked to the wiring in the dashboard).

2. Automotive industry today

Not long time ago, Court dismissed climate activists' lawsuit against Mercedes and BMW.

A new car has appeared in the offer of the Romanian brand "Dacia", the model is a mix of SUV and station wagon and is as long as 4.62 meters. After the "Sandero" became the best-selling car in Europe in 2025, for the second time in a row, the "Daster" took second place in its class.

The latest 3-wheel electric vehicle is designed to slide through traffic. The Trinova, California startup is 85 cm wide.

The first electric "Rolls-Royce" Black Badge Spectre is a blend of luxury and audacity, where tradition and technology are brought together in harmony. With 659 horsepower, it is a true blend of luxury and audacity. The ride is quiet yet powerful in this machine.

"Bugatti" is celebrating its 20th anniversary. The Bugatti Veyron was organized by the legendary gathering of hypercars. It is named after the racer Pierre Veyron.

The icon among jeeps in 2026 is the fully electric Jeep Recon, designed for off-road driving.

At "Fiat", October production was 73% above last year's average. Rubber and plastic production also recorded a positive trend, contributing to the overall growth of the processing sector.

The car from Kragujevac arrives as Fiat's savior in Europe: the "Grande Panda" was the best-selling Fiat in France in 2025 where 892 units of the B-segment model were registered in October. In Germany, 296 "Grande Pandas" were sold in the same month, and 283 in Spain. Much is expected from Turkey, where production of the popular Fiat Tipo will soon cease and sales of the "Grande Panda" will begin. Even more success is expected in 2026, when the car will also start being assembled in "Stellantis" factories in Morocco and Brazil, because the "Grande Panda" is designed as a global model. The "Grande Panda" is also among the seven finalists for the "European Car of the Year 2026!" award.

Fiat "Grande Panda" will be assembled in factory in Algeria. After months of stagnation and a difficult situation in Europe, Fiat has finally seen the light at the end of the tunnel. The reason? The Fiat "Grande Panda", which is starting to be delivered in significant quantities and giving the Italian brand an unexpected boost on the continent. This car has had the most success in Italy, where 1,912 Grande Pandas were registered in October, and the model from Kragujevac is now in 16th place in sales on the Apennine Peninsula.

Kragujevac's "Grande Panda" is not yet in the top 10 best-selling models in Europe. The problem with the car that is assembled in the heart of Šumadija was the lack of labor. Instead of the planned 500 units per day, 100-150 Grande Pandas rolled off the assembly lines, despite excellent demand across the continent. Sellers had to ask customers to be patient, or to be prepared to wait several months for delivery. This was the reason why many turned to another brand. In the meantime, production has stabilized, although it is still not at the desired level. In one period "Volkswagen" was left without key parts due to a shortage of semiconductors, and the cause was a dispute with a Dutch chip manufacturer. Nexperia is a silent giant of the chip industry.

In 2026 production of the "Grande Panda" with a gasoline engine has begun in Kragujevac. The factory employs more than 3,000 workers in three shifts. The "Stellantis" factory produces

three models of the "Grande Panda": electric, hybrid and with a gasoline engine. The production is underway introducing the hybrid model.

Chinese technology giant Xiaomi is testing a factory of the future where robots have begun assembling cars. Humanoid robots are helping to assemble electric cars at a factory in Beijing. Cars are being built every 76 seconds. The robots are currently serving as interns. [1]

It is also interesting that the Chinese company Changan is entering the market of Serbia and the Western Balkans by launching the Deepal So5 and So7 models. These are electric SUV models, and in our city of Belgrade, test drives of these cars are already being scheduled. For more traditional buyers, in the new era of mobility, the gasoline models Changan Cs55 and soon Cs35 and UNI-T are recommended.

3. Traffic safety and the future of electric vehicles

Few years ago, in 2023, the first E1 (E One) Electric Boat Racing Championship has been approved by the Union Internationale Motonautique (UIM), the world's leading body for motorboat racing. The competition was established primarily to create a new, competitive water racing offer, based on clean technologies, to protect our waters and coastal areas. [3]

According to a new study from 2025 by the most influential European consumer association BEUC, new mid-size electric vehicles will generally be cheaper to run than their petrol equivalents as early as 2026. Small city electric cars are forecast to be cheaper from this year. Although if the model of exclusive reliance on public chargers is maintained, petrol cars could remain more affordable for the next six years.

There are less than 1,000 electric vehicles in Serbia, and subsidies of 5,000 euros are planned. In Serbia, applications for subsidies for electric vehicles are submitted from March 1 to September 30, 2026, with the adoption of the Regulation on the conditions and manner of implementing subsidized purchases of new electric vehicles. [2]

The European Parliament and Council have reached a provisional agreement to revise the EU Driving Licence Directive, which will allow drivers with a standard Category B license to drive alternatively fueled vehicles (electric or hydrogen) weighing up to 4.25 tonnes (4,250 kg), starting approximately around 2028-2029. It indicates that from 2028, drivers with a category B driving licence will be able to drive vehicles weighing up to 4.25 tonnes, including camper vans. (this will only apply to those who passed their driving test after 1999). This marks the start of the implementation of the revised EU Driving Licence Directive, which was adopted in 2023. EU member states have 10 years to adapt.

Unfortunately, on our roads we had the black month of March 2026. In the first 12 days of the third month, 19 people died in traffic accidents, most of them young people. Since the beginning of the year, 120 people have lost their lives in traffic accidents / Serbian Ministry of Internal Affairs/. Caution is essential for all road users. Smart radars should contribute to compliance with regulations. Recently, stationary radars were installed at a total of 30 "black spots".

The Traffic Safety Agency has launched the "Get in the Car Without Alcohol" campaign, which is being implemented under the slogan "On the way to zero with zero per mille", and continues to promote that alcohol and driving never go together.

4. Conclusion

The EU is abandoning its plan to make all cars electric by 2035. Ford is radically reducing investments in electric vehicles - weak demand in the US is also cited.

According to a new study by the most influential European consumer association BEUC, new mid-size electric vehicles will generally be cheaper to run than their petrol equivalents as early as 2026, while in 2025 "Sandero" became the best-selling car in Europe. Small city electric cars are forecast to be cheaper only from 2026. However, the EU is abandoning its plan to make all cars electric by 2035.

How to prevent traffic tragedies in our country? Caution is essential for all road users. Smart radars should contribute to compliance with regulations. Recently, stationary radars were installed at a total of 30 "black spots". It is expected that they will significantly improve traffic safety.

In February 2026, the most urban electric car for 2025 was announced, and it was the “Byd Dolphin Surf”. It was also promoted in Belgrade, Serbia. Serbia was also the first country in Europe to sign an agreement with the American manufacturer of flying taxis, Archer Aviation. The first demonstration flights are expected in 2027, during the specialized exhibition EXPO. Welcome!

5. References

[1] Hong Huo, Qiang Zhang, Michael Q. Wang, David G. Streets, and Kebin He, Environmental Implication of Electric Vehicles in China, *Environ. Sci. Technol.* (2010), 44, 13, 4856–4861.

[2] Ministry of Environmental Protection of Serbia. (2022). Environmental Protection Strategy until 2030 (Ministarstvo zaštite životne sredine Srbije. (2022). Strategija zaštite životne sredine do 2030. godine) in Serbian

[3] Nautical lifestyle magazin, 68, 2023, p. 36 & 37.

Technical validity of motorcycles and mopeds as a factor of road safety in the Republic of Croatia

Luka Zovak[1], Goran Košir[2], Goran Zovak[2], Marija Ferko[1]
Faculty of Transport and Traffic Sciences, Zagreb, Croatia[1]
Centre for vehicles Croatia, Zagreb, Croatia[2]

Abstract: *This paper examines the technical validity of motorcycles and mopeds registered in the Republic of Croatia as a factor of road safety, analysing data from the Centre for Vehicles of Croatia (CVH) for the period 2023–2025. The study focuses on three dimensions: the age structure of the registered L category vehicle fleet, aggregate periodic technical inspection (PTI) defect data for all L category vehicles in 2025, and disaggregated inspection outcomes for L1 (mopeds) and L3 (motorcycles) subcategories. Results indicate that the Croatian PTW fleet is structurally aged, with over 57% of vehicles exceeding ten years of age in 2025. The overall PTI failure rate stands at 8,28%, with mopeds recording a substantially higher rate of 10,79% compared to 6,73% for motorcycles. The most prevalent defect categories are lighting and signalling devices (32,64%) and tires and suspension (25,15%). The findings highlight the need for strengthened PTI enforcement and targeted public awareness campaigns.*

Keywords*: ROAD SAFETY, MOTORCYCLES, MOPEDS, PERIODICAL TECHNICAL INSPECTION, VEHICLE DEFECTS*

1. Introduction

Motorcycles, mopeds, motor tricycles and quadricycles, collectively classified under European Union vehicle categories L1 through L7, occupy a distinctive and growing position within the contemporary transport system of the Republic of Croatia. Although this vehicle group encompasses three-wheeled and four-wheeled variants, many registered vehicles within this category are powered two-wheelers, and the term PTW (powered two-wheeler) will be used throughout this paper to refer to all L category vehicles collectively. Their relatively low acquisition and operating costs, combined with superior maneuverability in congested urban traffic, have rendered them an increasingly popular mode of transport, particularly during the spring and summer months when conditions in the Adriatic and continental regions are favorable for two-wheel travel. The registered PTW fleet in Croatia has grown steadily over recent years, reaching 184,555 L-category vehicles by 2025.

Despite their practical utility, powered two-wheelers are associated with a markedly elevated road safety risk profile relative to enclosed motor vehicles. PTW riders are among the most vulnerable participants in road traffic, lacking the structural crash protection available to car occupants and frequently exposed to the consequences of both their own riding behavior and the actions of other road users. Road fatality statistics across Europe consistently demonstrate that PTW riders are overrepresented in accident outcomes relative to their share of total vehicle kilometers travelled.

The causes of PTW accidents are multifactorial. Human behavioral factors, including excessive speed, impaired riding, and inadequate hazard perception, are widely recognized as primary contributors. However, the technical condition of the vehicle itself represents an equally important, independently addressable dimension of accident risk. Mechanical failures such as deteriorated braking systems, defective tires, malfunctioning lighting equipment, or non-compliant modifications can directly precipitate loss of vehicle control or impair a rider's capacity to respond effectively to road hazards. In Croatia, the periodic technical inspection (PTI) is the primary institutional mechanism through which safety-relevant vehicle deficiencies are identified and mandated for correction. The Centre for Vehicles Croatia (*Centar za vozila Hrvatske, CVH*) oversees PTI operations and maintains the national vehicle registration database. Despite the clear public safety relevance of PTW technical condition, systematic empirical analyses of inspection outcomes specific to this vehicle class remain limited in the Croatian research literature.

This paper addresses that gap by providing a comprehensive, data-driven examination of three interrelated dimensions: the age structure of the Croatian registered PTW fleet for the period 2023–2025; the aggregate defect profiles recorded at PTI for all L-category vehicles in 2025; and the disaggregated inspection outcomes and most prevalent defects for L1 (moped) and L3 (motorcycle) subcategories. The overarching objective is to assess the extent to which the structural and technical characteristics of the Croatian PTW fleet constitute a road safety concern, and to formulate evidence-based policy recommendations. The paper is structured as follows: Section 2 establishes the legislative and institutional framework; Section 3 analyses fleet age structure; Section 4 presents aggregate PTI defect data; Section 5 provides disaggregated L1 and L3 analysis; Section 6 discusses road safety implications; and Section 7 presents conclusions and recommendations.

2. Legislative and institutional framework

The regulation of powered two-wheelers in the Republic of Croatia is embedded within a layered framework of European Union and national legislation. At the EU level, Regulation (EU) No. 168/2013 of the European Parliament and of the Council on the approval and market surveillance of two- or three-wheel vehicles and quadricycles establishes the type-approval requirements for L-category vehicles and defines the subcategories L1 through L7 according to engine displacement, maximum design speed, and number of wheels [1]. This classification directly determines the applicable inspection periodicity and technical safety standards. With respect to roadworthiness testing, Directive 2014/45/EU of the European Parliament and of the Council on periodic roadworthiness tests for motor vehicles and their trailers sets out the minimum harmonised standards for PTI procedures across EU member states [2]. Croatia has transposed this Directive into national law through the Act on Road Traffic Safety (*Zakon o sigurnosti prometa na cestama*) and accompanying secondary legislation, including the Ordinance on Technical Inspection of Vehicles (*Pravilnik o tehničkom pregledu vozila*) [3]. Under the applicable Croatian legal regime, mopeds and motorcycles are subject to mandatory periodic roadworthiness testing.

The institutional responsibility for PTI oversight is vested in the CVH, which also maintains the Central Vehicle Register (*Središnji registar vozila*). The CVH collects and publishes annual statistical data on vehicle registrations and inspection outcomes, which constitute the primary data sources for the present analysis [4]. It is important to note that the PTI data examined in this paper pertain exclusively to vehicles actually presented for inspection; vehicles operated with expired technical validity that were not presented for inspection fall outside the captured dataset — an inherent limitation of administratively sourced inspection data that should be borne in mind when interpreting the figures presented in subsequent sections.

3. Age structure of registered motorcycles and mopeds (2023. – 2025.)

The age profile of a vehicle fleet serves as a leading structural indicator of its likely technical condition and road safety risk. For powered two-wheelers where brake, tire, or lighting failure can be immediately life-threatening, monitoring fleet age assumes particular importance. Research consistently demonstrates that the

risk of safety-relevant technical defects increases substantially with vehicle age, and that vehicles older than ten years exhibit disproportionately elevated defect rates at periodic inspection [5]. Furthermore, older vehicles lack the advanced active safety technologies such as anti-lock braking systems (ABS) that have become progressively standard on newer PTW models and that contribute meaningfully to crash prevention [6]. The following analysis draws on CVH registration data for the period 2023 – 2025 and encompasses all L1–L7 category vehicles registered in the Republic of Croatia [4].

As shown in Figures 1, 2 and 3, and summarised in Table 1, the Croatian PTW fleet is characterised by a persistent and marked structural ageing across all three years examined. In 2023, a total of 165,260 L-category vehicles were registered, of which 115,192 units, representing 69.69% of the fleet, were older than ten years. Vehicles in the six-to-nine-year age bracket numbered 17,735 (10.74%), those aged two to five years accounted for 19,747 registrations (11.95%), and newly registered vehicles up to one year of age constituted 12,586 units (7.62%) [4].

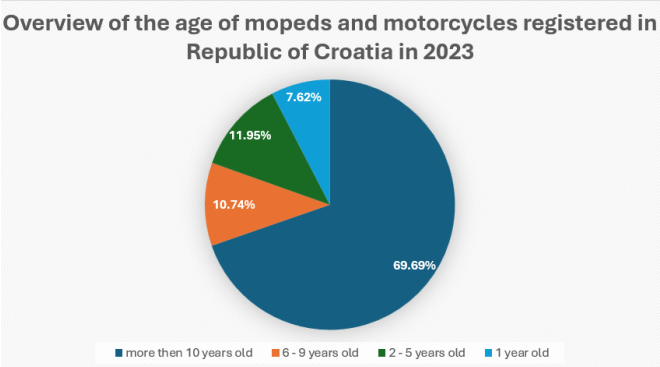


Figure 1. Age structure of registered mopeds and motorcycles in the Republic of Croatia, 2023 [4]

In 2024, the total registered fleet increased to 175,410 vehicles, reflecting year-on-year growth of approximately 6.14%. The over-ten-years cohort remained dominant, accounting for 117,431 vehicles (66.93%), while the six-to-nine-year bracket comprised 20,092 units (11.46%), the two-to-five-year cohort 21,716 vehicles (12.39%), and newly registered vehicles 16,171 units (9.22%). The proportional decline in the oldest cohort, from 69.69% in 2023 to 66.93% in 2024, is marginal and does not indicate a substantive structural shift in fleet composition [4].

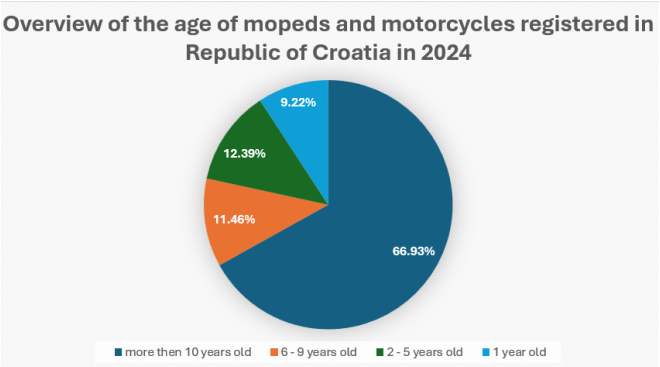


Figure 2. Age structure of registered mopeds and motorcycles in the Republic of Croatia, 2024 [4]

By 2025, the registered fleet had grown further to 184,555 vehicles, cumulative increase of 11.67% compared to 2023. The most notable development in the 2025 data is a more pronounced decline in the proportional share of vehicles older than ten years, which fell to 57.58% (118,896 units). This reduction of approximately 12 percent relative to 2023 is primarily driven by the substantial growth of the six-to-nine-year cohort, which expanded from 10.74% in 2023 to 21.56% in 2025 (22,605 units), suggesting a partial maturation of vehicles registered in the 2016–2019 period now entering this age bracket. The two-to-five-year and up-to-one-year cohorts showed moderate growth in absolute terms, registering 25,963 units (12.58%) and 17,091 units (8.28%) respectively [4].

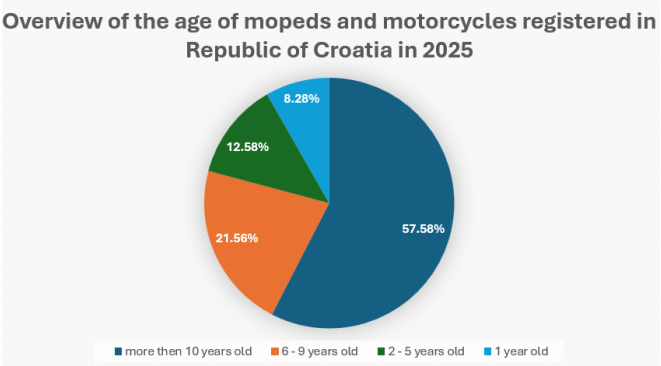


Figure 3. Age structure of registered mopeds and motorcycles in the Republic of Croatia, 2025 [4]

Table 1. Age structure of registered L – category vehicles in Croatia, 2023 – 2025

Age category	2023		2024		2025	
	number	%	number	%	number	%
>10 years old	115,192	69.69%	117,431	66.93%	118,896	57.58%
6 - 9 years old	17,735	10.74%	20,092	11.46%	22,605	21.56%
2 - 5 years old	19,747	11.95%	21,716	12.39%	25,963	12.58%
1 year old	12,586	7.62%	16,171	9.22%	17,091	8.28%
TOTAL	**165,260**	**100%**	**175,410**	**100%**	**184,555**	**100%**

Source: [4]

Notwithstanding the encouraging directional trend in 2025, the data presented in Table 1 confirm that the Croatian PTW fleet remains structurally aged. Even in 2025, vehicles six or more years old collectively accounted for 79.14% of the total registered fleet. The European Road Safety Observatory has documented that PTW riders are consistently overrepresented in road fatality statistics across EU member states, with motorcyclists alone accounting for approximately 16% of all road deaths in 2022 [7]. The persistence of such a large proportion of aged vehicles therefore constitutes a structural road safety risk that cannot be adequately addressed through fleet renewal alone but requires robust technical inspection enforcement as a complementary measure [5].

4. Aggregate defect profile of L – category vehicles at periodic technical inspection (2025)

The periodic technical inspection constitutes the primary formal mechanism through which safety-relevant technical defects in the vehicle fleet are identified, documented, and mandated for correction. A systematic review of the international evidence base has demonstrated that the proportion of road crashes attributed to vehicle defects ranges from 3% to 19% in high-income countries, and that PTI programs are an effective mechanism for identifying and compelling correction of such deficiencies [5]. An analysis of the aggregate PTI defect data for all L-category vehicles inspected in Croatia in 2025 provides a systemic overview of the most prevalent technical failure modes within the national PTW fleet. CVH recorded a total of 34,426 individual defects across all inspected L-category vehicles during 2025, distributed across fifteen standardized component system categories as presented in Table 2 [4].

Of the 165,908 L category vehicles submitted for PTI in 2025, a total of 13,734 were found to have at least one defect, yielding an overall malfunction rate of 8.28%. The average number of defects per defective vehicle was 2,507, indicating that vehicles presenting with at least one fault typically exhibited multiple concurrent deficiencies. a pattern consistent with the established relationship between vehicle age and compounding mechanical wear [5].

Table 2. Number of recorded errors and malfunctions by system category, all L – category vehicles, 2025

TERM	NUMBER OF ERRORS	% IN THE TOTAL DETERMINED NUMBER OF L CATEGORY DEFECTS	AVERAGE NUMBER OF ERRORS PER DEFECTIVE L CATEGORY VEHICLE
VEHICLE IDENTIFICATION	977	2.84	0.07
CONTROL DEVICES	238	0.69	0.02
BRAKING DEVICE	2,389	6.94	0.17
LIGHTING AND LIGHT SIGNALLING DEVICES	11,236	32.64	0.82
DEVICES THAT ENABLE NORMAL VISIBILITY	1,805	5.24	0.13
SELF-SUPPORTING BODY, CHASSIS AND OTHER PARTS	1,979	5.75	0.14
AXLES, WHEELS, TIRES AND SUSPENSION	8,657	25.15	0.63
ENGINE	1,611	4.68	0.12
ENVIRONMENTAL IMPACT	275	0.80	0.02
ELECTRICAL DEVICES AND INSTALLATIONS	165	0.48	0.01
TRANSMISSION MECHANISM	365	1.06	0.03
CONTROL AND SIGNALING DEVICES	2,794	8.12	0.20
COUPLING OF TOWING AND ATTACHED VEHICLE	25	0.07	0.00
OTHER DEVICES AND VEHICLE PARTS	210	0.61	0.02
VEHICLE EQUIPMENT	1,700	4.94	0.12
TOTAL ERRORS	**34,426**	**100.00**	**2.51**
TOTAL NON-DEFECTIVE L VEHICLES	**13,734**		
TOTAL L VEHICLES REVIEWED	**165,908**		
% OF L VEHICLE MALFUNCTIONS	**8.28**		

Source: [4]

As shown in Table 2, the most prevalent defect category by a considerable margin was Lighting and Light Signaling Devices (Label 03), which accounted for 11,236 defects, equivalent to 32.64% of all recorded deficiencies. This finding is particularly significant from a road safety perspective, as lighting defects directly impair the visibility of PTW riders to other road users and simultaneously reduce the rider's own ability to perceive the road environment under low-light conditions. Research into PTW accident causation has consistently identified conspicuity deficits, including defective lighting and missing reflectors as contributing factors in collision scenarios, particularly in interactions with other motor vehicles [8]. The average number of lighting defects per defective vehicle (0.82) suggests that lighting failures are among the most frequently occurring individual fault types across the entire fleet.

The second largest defect category was Axles, Wheels, Tires and Suspension (Label 06), responsible for 8,657 defects or 25.15% of the total. Tire and suspension deficiencies are directly implicated in vehicle stability and performance, particularly in emergency breaking and evasive maneuver scenarios. The high prevalence of this category is consistent with the fleet age structure documented in Section 3, as rubber degradation and suspension wear are strongly age and mileage dependent failure modes.

Control and Signaling Devices (Label 11) constituted the third most frequent defect group, with 2,794 occurrences (8.12%), followed by the Braking Device category (Label 02) with 2,389 defects (6.94%). Brake deficiencies represent one of the most direct safety-critical failure modes for any vehicle and are particularly consequential for PTWs, where braking performance is the primary means of emergency speed reduction in the absence of structural crash protection. The Rechnitzer et al. report on vehicle roadworthiness confirmed a statistically significant relationship between brake deficiencies and elevated crash risk, particularly for single-vehicle accident scenarios [9]. The combined share of braking, lighting, tire, and suspension defects accounts for approximately 70% of all recorded PTI deficiencies, a concentration that highlights the primary technical risk domains within the Croatian L category fleet.

Vehicle Equipment (Label 15) recorded 1,700 defects (4.94%), while Self-Supporting Body, Chassis and Other Parts (Label 05) accounted for 1,979 deficiencies (5.75%). Devices Enabling Normal Visibility (Label 04) registered 1,805 defects (5.24%). Defect categories with comparatively low frequencies included Environmental Impact (Label 08, 0.80%), Coupling of Towing and Attached Vehicles (Label 13, 0.07%), and Electrical Devices and Installations (Label 09, 0.48%). These lower-frequency categories nonetheless carry road safety relevance, and their presence reinforces the case for comprehensive PTI coverage across all vehicle system groups [2].

5. Disaggregated technical inspection analysis of L1 and L3 vehicle category

5.1. Overall inspection outcomes

While the aggregate L category defect data presented in Section 4 provides a system-level overview, a disaggregated analysis of the L1 (moped) and L3 (motorcycle) subcategories reveals important structural differences in inspection outcomes with significant implications for targeted road safety intervention. Table 3 presents the PTI results for L1 and L3 vehicles individually and in combination, based on CVH inspection records for 2025 [4].

Table 3. PTI outcomes for L1 and L3 category vehicles, 2025

Vehicle category	Failed PTI	Passed PTI	Total	Failure rate (%)
L1	6,592	54,907	61,547	**10.79**
L3	6,732	94,058	100,848	**6.73**
L1 & L3	13,324	148,965	162.395*	**8.20**

Source: [4]

Of the 61,547 L1 category vehicles (mopeds) subjected to PTI in 2025, a total of 6,592 failed the inspection, yielding a failure rate of 10.79%. By contrast, of the 100,848 L3 category vehicles (motorcycles) inspected, 6,732 failed, corresponding to a markedly lower failure rate of 6.73%. The combined failure rate for L1 and L3 vehicles was 8.20%, closely aligned with the overall L category rate of 8.28% [4].

The substantially higher failure rate for mopeds relative to motorcycles, a differential of approximately 4%, warrants careful interpretation. Research on PTW accident risk has established that mopeds and motorcycles exhibit meaningfully different crash profiles, user demographics, and maintenance behavior patterns [10]. Mopeds are typically lower-cost vehicles whose users may prioritize cost minimization over systematic vehicle upkeep. Furthermore, the specific technical requirements applicable to L1 vehicles, notably the mandatory speed limiter, introduce a category-specific failure mode with no direct analogue in L3 vehicles, as discussed in Section 5.3. The Croatian context is particularly relevant: a study of motorcyclist behavior among 842 Croatian riders confirmed that younger riders exhibit significantly higher rates of risky behaviors and non-compliance patterns [11], a profile consistent with the moped user demographic.

5.2. Defect severity distribution

Beyond the binary pass/fail outcome, the CVH inspection data permit disaggregation of recorded defects by severity classification, specifically between minor defects, which do not preclude passage of PTI, and major defects, which result in PTI failure. Table 4 presents this distribution for L1 and L3 vehicles separately and in combination [4].

Table 4. Distribution of minor and major defects at PTI – L1 and L3 categories, 2025

Number of recorded errors at PTI of L1 & L3 categories	L1 - mopeds	L3 - motocycles	Combined L1 & L3
Minor defect / passed PTI	3,974	6,190	10,164
Failed PTI	11,387	11,987	23,374
Total defects	**15,361**	**18,177**	**33,538**

Source: [4]

A total of 33,538 individual defects were recorded across L1 and L3 vehicles combined, of which 23,374, representing 69.70% were classified as major defects resulting in PTI failure, and 10,164 (30.30%) constituted minor defects compatible with PTI passage. For L1 mopeds, 15,361 defects were recorded in total, with 11,387 (74.12%) classified as major and 3,974 (25.88%) as minor. For L3 motorcycles, 18,177 total defects were recorded, with 11,987 major (65.95%) and 6,190 minor (34.05%). The higher proportion of major defects among L1 vehicles is consistent with the higher overall failure rate observed for this subcategory.

It is noteworthy that even minor defects, not individually sufficient to cause PTI failure, may contribute to incremental increases in accident risk when present in combination with other vehicles, riders or environmental factors. A PTW with several concurrent minor defects may exhibit meaningfully degraded handling or conspicuity characteristics that, while falling below individual failure thresholds, collectively represent an elevated risk profile. The overview by Vlahogianni confirms that risk factors in PTW accidents operate in combination rather than in isolation, reinforcing the case for monitoring minor defect prevalence as a complementary safety indicator alongside the failure rate [8].

5.3. Most prevalent defects – L1 category (mopeds)

Table 5 presents the ten most frequently recorded individual defects for L1 category vehicles at PTI in 2025, classified by number of occurrences and defect severity (P = minor/passed; F = major/failed). This ranking provides granular insight into the specific technical failure modes most commonly affecting the moped sub-fleet [4].

Table 5. Ten most frequently recorded defects – L1 category (mopeds), 2025

Defect description	No. of occurrences	Classification
Tires, need replacement of tires soon	2052	Minor (P)
Speed limiter on mopeds, does not work	1882	Major (F)
Service brake executive elements, insufficient braking efficiency (braking coefficient)	631	Major (F)
Rear position lights, one or more lights not working	512	Major (F)
Tires, tread depth, small	493	Major (F)
Reflectors, missing	474	Major (F)
Brake lights, one or more lights not working	443	Major (F)
Indicators, one or more lights not working	425	Major (F)
Short light not working	407	Major (F)
Short light, minor glass or lens cloud	310	Minor (P)

Source: [4]

The most frequently recorded defect among L1 vehicles was tire condition requiring imminent replacement (2,052 occurrences), classified as a minor defect. The second most prevalent defect, and the most common major defect resulting in PTI failure, was the non-functioning speed limiter (1,882 occurrences), a deficiency specific to the L1 category. Under Croatian and EU law, mopeds are required to be limited to a maximum design speed of 45 km/h; a non-functional speed limiter represents both a registration non-compliance and a direct road safety hazard, as it permits the vehicle to operate at speeds exceeding the design parameters of its braking and stability systems [1]. This deficiency has no equivalent in the L3 category and accounts for a substantial portion of the differential in failure rates between the two subcategories.

Braking deficiencies ranked third, with 631 recorded instances of insufficient braking efficiency in service brake executive elements, a major defect with direct accident causation potential. The Rechnitzer analysis of vehicle roadworthiness and crash incidence confirmed that brake-related defects are among the most causally significant technical failure modes in PTW accident sequences [9]. Rear position light failures (512), tread depth deficiencies (493), missing reflectors (474), brake light failures (443), indicator failures (425), and headlight malfunctions (407) collectively represent a cluster of lighting, visibility, and signaling deficiencies. Research on PTW safety risk factors has consistently identified conspicuity and lighting as critical variables in collision scenarios involving other motor vehicles [8, 12].

5.4. Most prevalent defects – L3 category (motorcycles)

Table 6 presents the equivalent defect ranking for L3 category vehicles (motorcycles) at PTI in 2025. The defect profile of the L3 sub-fleet exhibits both points of similarity and meaningful divergence relative to that of L1 vehicles, reflecting the different vehicle characteristics, use patterns, and rider demographics documented in the comparative PTW literature [4, 10].

Table 6. Ten most frequently recorded defects – L3 category (motorcycles), 2025

Detected defects	No. of occurrences	Classification
Tires, need replacement of tires soon	3075	Minor (P)
First aid box (container), missing	1129	Minor (P)
Reflectors, missing	952	Major (F)
Tires, tread depth, small	941	Major (F)
Exhaust system, modification that is not permitted or approved	589	Major (F)
Direction indicators, modification that is not permitted or approved	522	Major (F)
Reflective vest, missing	482	Minor (P)
Brake lights, one or more lights not working	428	Major (F)
Rear postion lights, one or more lights not working	408	Major (F)
Direction indicators, one or more lights not working	366	Major (F)

Source: [4]

As with L1 vehicles, the most common defect among L3 motorcycles was tire wear requiring imminent replacement (3,075 occurrences, minor). The second most frequent defect was the absence of a first aid box (1,129, minor) — reflects a Croatian legal requirement for motorcycles to carry a mandatory first aid kit [3]. Missing reflectors ranked third (952, major), followed by insufficient tire tread depth (941, major).

A particularly notable feature of the L3 defect profile is the relatively high frequency of non-approved modifications: exhaust system modifications were recorded 589 times (major), while non-approved direction indicator modifications accounted for 522 defects (major). Such modifications may compromise structural integrity, emissions compliance, or the effectiveness of mandatory signaling equipment, and they represent a category of non-compliance that is specific to the motorcycle sub-culture and has no direct equivalent in the utility-focused moped segment [11]. Missing reflective vests (482, minor) ranked seventh, reflecting an equipment requirement under Croatian law [3]. Brake light failures (428, major), rear position light failures (408, major), and direction indicator failures (366, major) complete the top ten, reinforcing the systemic importance of lighting and signaling deficiencies identified in Section 4 [8, 12].

6. Discussion – road safety implications

The findings presented in Sections 3–5 collectively paint a coherent and concerning picture of the technical condition of the Croatian PTW fleet. Three principal road safety implications merit sustained analytical attention.

First, the structural ageing of the fleet represents a persistent background risk factor that amplifies the likelihood of safety-critical technical failures. With over 57% of registered PTWs exceeding ten years of age in 2025, and more than 79% surpassing six years of age, the Croatian fleet is operating at a structural age profile that generates elevated defect risk across multiple safety-critical systems simultaneously. According to the European Road Safety Observatory, motorcyclists are 49 times more likely to die in a crash per vehicle kilometer than car drivers, a disparity that existing research attributes in part to the absence of passive crash protection and to the technical vulnerabilities of older vehicles [12]. The progressive mainstreaming of active safety systems, including ABS, traction control, and electronic stability control, on newer PTW models underscores the importance of fleet renewal as a long-term road safety lever [6], even as PTI enforcement addresses the immediate deficiency landscape.

Second, the concentration of defects in lighting, tire, and braking systems is not coincidental. These three system categories are precisely those most directly implicated in PTW accident causation in the European in-depth research literature. The overview by Vlahogianni similarly confirmed that lighting, tire, and braking conditions are among the critical vehicle-related risk factors for PTW accident involvement and severity [8]. The alignment

between the Croatian PTI defect profile and this established body of European accident causation evidence strongly suggests that targeted enforcement focusing on these defect categories would yield commensurate improvements in road safety outcomes.

Third, the significantly higher failure rate of L1 mopeds (10.79%) relative to L3 motorcycles (6.73%) suggests that subcategory-differentiated intervention strategies may be more effective than uniform fleet-wide approaches. Comparative research by Blackman and Haworth established that mopeds and motorcycles exhibit distinct crash profiles driven by differences in vehicle design, speed capability, and user demographics [10]. The concentration of speed limiter failures and braking deficiencies in the L1 sub-fleet, combined with the risk behavior patterns documented among younger Croatian riders [11], points toward a user group and vehicle type that may benefit particularly from enhanced enforcement activity and targeted public information campaigns emphasizing the safety rationale for speed limitation compliance.

7. Conclusion and policy recommendations

This paper has presented a comprehensive, data-driven analysis of the technical validity of motorcycles and mopeds in the Republic of Croatia, drawing on CVH registration and PTI data for the period 2023–2025. The findings across the three analytical dimensions examined lead to several clear and consistent conclusions.

The Croatian L category vehicle fleet is structurally aged, with the majority of registered PTWs exceeding ten years of age in all three years examined. While a gradual directional improvement is observable between 2023 and 2025, driven primarily by growth in the six-to-nine-year age cohort, over 79% of the fleet remained six or more years old in 2025. The overall PTI failure rate of 8.28% for L category vehicles, with a particularly elevated rate of 10.79% for mopeds, indicates that a substantial share of the fleet presents for inspection in a condition that fails to meet minimum roadworthiness standards. The dominant defect categories, lighting and signaling, tires and suspension, and braking systems are precisely those most directly associated with accident causation in European PTW crash research. Non-approved modifications represent an additional and growing category of concern specific to the motorcycle sub-fleet.

Based on these findings, three principal policy recommendations are advanced. First, enforcement of PTI compliance obligations for L category vehicles should be strengthened, with particular emphasis on the higher-risk moped subcategory and older vehicles. Targeted roadside inspection campaigns focusing on lighting, tire condition, and braking performance would complement the existing PTI framework and help capture vehicles operated with expired technical validity that fall outside the administrative dataset.

Second, public awareness campaigns addressing the road safety rationale for speed limiter compliance in mopeds, and the risks associated with non-approved vehicle modifications in motorcycles should be developed in collaboration with rider associations, insurers, and road safety authorities. Such campaigns should be targeted at the specific user groups most associated with these failure modes.

Third, longitudinal research linking PTI defect records to accident data should be commissioned to enable causal estimation of the road safety impact of specific technical deficiency types. The current analysis is limited to inspection outcomes and does not permit direct quantification of the accident contribution of individual defect categories. Closing this evidence gap would substantially strengthen the basis for future policy development. Future research should also examine the spatial distribution of PTI outcomes across Croatian counties, the economic determinants of maintenance behavior, and the potential safety dividend of accelerated fleet renewal incentive schemes.

Literature

[1] European Parliament and Council. (2013). Regulation (EU) No 168/2013 on the approval and market surveillance of two- or three-wheel vehicles and quadricycles. Official Journal of the European Union, L 60, 52–128. Available at: https://eur-lex.europa.eu/eli/reg/2013/168/oj/eng [Accessed: 3.4.2026.]

[2] European Parliament and Council. (2014). Directive 2014/45/EU on periodic roadworthiness tests for motor vehicles and their trailers. Official Journal of the European Union, L 127, 51–128. Available at: https://eur-lex.europa.eu/eli/dir/2014/45/oj/eng [Accessed: 3.4.2026.]

[3] Republic of Croatia. (2023). Zakon o sigurnosti prometa na cestama (Act on Road Traffic Safety). Narodne novine, Zagreb. Available at: https://www.zakon.hr/z/78/zakon-o-sigurnosti-prometa-na-cestama [Accessed: 3.4.2026.]

[4] Centar za vozila Hrvatske (CVH). (2025). Statistical Data on Vehicle Registration and Periodic Technical Inspection Outcomes for L-Category Vehicles in the Republic of Croatia, 2023–2025. CVH, Zagreb. Available at: https://www.cvh.hr/gradani/tehnicki-pregled/statistika/ [Accessed: 3.4.2026.]

[5] Gómez-Lantada, C., Simó-Solsona, M., & Sallent-Ribes, J. (2021). Effect of Periodic Vehicle Inspection on Road Crashes and Injuries: A Systematic Review. International Journal of Environmental Research and Public Health, 18(12), 6476. https://doi.org/10.3390/ijerph18126476 [Accessed: 6.4.2026.]

[6] Savino, G., Giovannini, F., & Pierini, M. (2020). Active safety systems for powered two-wheelers: A systematic review. Traffic Injury Prevention, 21(1), 78–86. https://doi.org/10.1080/15389588.2019.1700408 [Accessed: 6.4.2026.]

[7] European Commission – European Road Safety Observatory. (2020). Facts and Figures: Motorcyclists and Moped Riders. Publications Office of the European Union, Brussels. Available at: https://road-safety.transport.ec.europa.eu/system/files/2021-07/facts_figures_p2w_final_20210323.pdf [Accessed: 6.4.2026.]

[8] Vlahogianni, E.I., Yannis, G., & Golias, J.C. (2012). Overview of critical risk factors in Power-Two-Wheeler safety. Accident Analysis & Prevention, 49, 12–22. https://doi.org/10.1016/j.aap.2012.04.009 [Accessed: 6.4.2026.]

[9] Rechnitzer, G., Haworth, N., & Kowadlo, N. (2001). The Effect of Vehicle Roadworthiness on Crash Incidence and Severity. Monash University Accident Research Centre, Report No. 164. Melbourne. Available at: https://www.monash.edu/__data/assets/pdf_file/0017/216710/The-effect-of-vehicle-roadworthiness-on-crash-incidence-and-severity.pdf [Accessed: 6.4.2026.]

[10] Blackman, R.A., & Haworth, N.L. (2013). Comparison of moped, scooter and motorcycle crash risk and crash severity. Accident Analysis and Prevention, 57, 1–9. Available at: https://www.researchgate.net/publication/236598676_Comparison_of_moped_scooter_and_motorcycle_crash_risk_and_crash_severity [Accessed: 6.4.2026.]

[11] Ferko, M., Babić, D., Brijs T., Babić D., Pirdavani A. (2025). Understanding risky riding: Factors influencing crashes, near-crashes, and traffic fines among motorcyclists in Croatia. Transportation Research Part F: Traffic Psychology and Behaviour. Available at: https://www.sciencedirect.com/science/article/abs/pii/S1369847825002529 [Accessed: 6.4.2026.]

[12] European Road Safety Observatory (ERSO). (2024). Road Safety Thematic Report — Powered Two-Wheelers. European Commission, Brussels. Available at: https://www.efa-eu.com/wp-content/uploads/2024/11/8-ERSO-TR-Powered-two-wheelers-20240912.pdf [Accessed: 6.4.2026.]

Determining the use indicators of the wagon vehicle and improving the efficiency of the transportation process

Israil Shukur Oglu Elyazov, Etibar Bakhtiyar Oglu Guliyev
Azerbaijan University of Architecture and Construction, Baku
[1]

ABSTRACT. *The primary function of the Azerbaijan Railways wagon fleet is to ensure the transportation process is continuously supplied with serviceable and operational wagons. Given the continuous growth in transit freight volumes along international transport routes passing through our country, Azerbaijan Railways CJSC successfully continues to modernize and expand its wagon fleet to ensure the efficient and safe transportation of goods. To this end, studying the wagon fleet structure, analyzing optimal wagon fleet utilization indicators, and determining the required number of wagon fleets are currently considered pressing issues. Accordingly, determining the structure of wagons within and outside the railway wagon fleet is of particular importance. Accounting for freight wagon fleets is crucial for regulating, standardizing, and utilizing the wagon fleet for its intended purpose in managing rail transport to meet the needs of the national economy for freight and passenger transportation. The operating freight car fleet includes both local cars operated by Azerbaijan Railways CJSC and transit freight cars from abroad located on the tracks of industrial enterprises. Efficient use of the freight car fleet is an important factor influencing the operational performance, cost structure, and service reliability of rail transport systems. This study develops a comprehensive methodological framework for determining the efficiency of the freight car fleet and proposes an integrated performance assessment model. Key performance indicators, including car turnaround time, technical availability, load factor, downtime rate, and daily productivity, are analytically formalized. An integrated performance function is proposed for assessing overall operational efficiency. The results demonstrate that reducing turnaround time, minimizing downtime, increasing technical availability, and implementing digital fleet management systems significantly improve the efficiency of rail freight transportation. The proposed model can be applied to comparative analysis, strategic planning, and optimization of rail crew work at railway enterprises.*

KEY WORDS*: WAGON, WORKING FLEET, BALANCE METHOD, WAGON TURNOVER, MILEAGE, TRIP, TRANSPORTATION, WAGON SHOULDER, TECHNICAL STATION, PRODUCTIVITY, RAILWAY.*

INTRODUCTİON. The existing fleet also includes wagons belonging to other ministries and companies, each with an eight-digit inventory number beginning with 5, belonging to CIS member states, whose access to the common railway network has been authorized by the Directorate of the CIS Railway Transport Council and the railway director for the transportation of freight specified in the declaration within the railway (in suburban service). Accordingly, the structure of changes in the number of wagons belonging to the railway's wagon fleet, the methodical sequential calculation of fleet utilization indicators, and the methodology for calculating the required quantity are distinguished by their relevance [1, 2, 4]:

Research work conducted in the field of wagon management varies in its specifics. It is known that the existing freight wagon fleet on Azerbaijan Railways is modified by the following transport reports:

- new wagons arriving from industrial enterprises, factories, and imported ones;
- wagons arriving from Caspian Sea ferry crossings (Turkmenbashi, Aktau, Kuryk) from the Alyat International Sea Trade Port ferry;
- wagons from the inventory of wagons of CIS member states and the Baltic Republics, as well as wagons of enterprises and organizations of other ministries and departments that have permission to enter the general CIS railway network, and wagons received from Iranian Railways at Julfa station;
- wagons of enterprises and organizations of other ministries and departments that have permission to enter the general CIS railway network in the established manner and that have been accepted from bypass tracks;

At the same time, it can be said that the existing fleet of freight cars on the railway may also be modified by:

- cars decommissioned due to technical condition,
- cars received from Alat, delivered from the International Sea Trade Port of Turkmenbashi, Aktau, and the Kuryk ferry crossing,
- cars from the inventory of the Union member states and the Baltic Republics, owned by enterprises and organizations of other ministries and departments that have, in accordance with the established procedure, permission to enter the common railway network of the CIS, and delivered to the Iranian Railway at the Julfa station,
- freight cars from the inventory of Azerbaijan Railways CJSC on the balance sheet of companies, enterprises, and organizations of other ministries and departments of the Republic of Azerbaijan,
- freight cars delivered to bypass routes, owned by enterprises and organizations of other ministries and departments that have, in accordance with the established procedure, permission to enter the common railway network of the Commonwealth country Independent States.

MAİN PART. The increase in the volume of freight transportation by rail leads to changes in the structure of the wagon fleet and the purchase of new wagons. In connection with this, both the inventory and available fleet of freight wagons on the railway are constantly changing. The inventory and available fleet of freight wagons on the railway always differ. The current fleet of freight wagons is determined for each station, section of the road, railway and the entire railway network of the CIS country. It is known that the initial data for calculating the inventory of freight wagons on the railway by versatility, purpose, type and technical condition are determined on the basis of the main results of the physical inventory in accordance with the numerical records of wagons, conducted in the periods established by the Directorate of the Council of Railway Transport of the Commonwealth of Independent States [10,11]. Regardless of the turnover of wagons, the availability of freight wagons at all stations and railway lines during the reporting period is calculated using the balance method [3], based on the integral efficiency function.

$B = f(N_{in}, N_{to}, N_{ss}, N_{is}) = \mathrm{N_{in}} - \mathrm{N_{to}} - -\mathrm{N_{ss}} + \mathrm{N_{is}}$ (1)

here, N_{to} -is the required fleet size during the planning period; N_{in} - is the number of freight cars in the fleet at the beginning of the planning period; N_{ss} is the number of cars whose service life has expired; and N_{is} -is the number of newly manufactured (accepted into the fleet) cars. At all stations with a daily turnover of 50 or more freight cars, freight car turnover is based on records of the number of received and dispatched freight cars reflected in the company's balance sheet. At all stations with a daily turnover of 50 or fewer cars, turnover is based on data from the locomotive and train movement desk log. In cases where the balance of freight cars at stations does not correspond to the actual availability of freight cars, the section manager, upon submission by the heads of the transportation, statistics, and economic analysis departments, establishes a procedure for recording the actual number of cars and, based on the results, makes a decision to change the balance of freight cars at the station.

Adjustments to the balance of freight cars on section tracks may only be made with the permission of the head of the department of statistics and economic analysis, and on the entire railway, with the permission of the head of the "Directorate of the Council for Railway Transport of the CIS Country."

The movement of all freight cars between railway sections and roads is recorded both by total quantity and by type, categorizing them as empty, loaded, and not included in the working inventory. The functional and structural composition of the existing freight car fleet of Azerbaijan Railways CJSC (ARC CJSC) [6] is primarily divided into two main groups.

1. Freight car fleet operated by CJSC Azerbaijan Railways,

2. Freight car fleet not operated by CJSC Azerbaijan Railways.

According to statistical data for 2025 [7], Table 1 presents the structural composition of the wagon fleet of CJSC Azerbaijan Railways.

The freight car fleet operated by CJSC Azerbaijan Railways includes freight cars from the existing inventory, excluding freight cars leased to companies, organizations, and enterprises of other committees, ministries, and departments located on their sidings and stations, as well as those provided to new sections of the country's railways under construction. Changes in the composition and structure of the freight car fleet at the disposal of the country's railways occur due to changes in the existing car fleet, as well as for the following reasons:

- the provision and return of cars from the inventory car fleet of CIS railways to railways under construction;
- the leasing and transfer of cars to and from the sidings of enterprises, as well as the return of cars from leases.

Freight cars owned by enterprises and organizations of other ministries and departments, with an eight-digit number beginning with 5, and duly authorized to enter the unified interstate network of the CIS, when transferred to a railway under construction, are counted as owned cars assigned to the enterprises' bypasses. When transferring such cars from railways under construction to the general CIS railway network, they are counted as cars arriving from the enterprises' bypasses. The entire fleet of freight cars at the railway's disposal is divided into two main groups:

1. Operating freight car fleet,
2. Non-operating freight car fleet (cars removed from the operating fleet).

Working fleet includes cars on trains assigned to implement the operational freight transportation plan and cars located on the tracks of the railway's marshalling yard. Depending on their technical and operational condition, working fleet cars are divided into two groups: loaded and empty.

Loaded rail cars are further divided into cars for unloading on the track, local freight cars intended for marshalling, and cars leaving the track (transit loaded cars).

Freight cars on the local railway include cars destined for railways under construction, railways in foreign countries, as well as cars destined for railways under construction and railways adjacent to foreign countries.

Table 1 - Freight car fleet of Azerbaijan Railways CJSC [7]

№	Car type	Total number of cars	Including cars from the Nakhchivan ARc	Cars with expired service life	Cars with unexpired service life
A	**General Purpose Cars**	**4944**	**538**	**1700**	**3164**
1.1	Box Cars	807	155	364	443
1.2	Flat Cars	1129	57	396	733
1.3	Gondola Cars	1261	233	261	1000
1.4	Tank Cars	1199	42	211	988
1.5	Isothermal Cars	548	51	468	-
B	**Special-Purpose Cars**	**941**	**32**	**180**	**761**
2.1	Hopper Cars	110	-	10	100
2.2	Dump Cars	64	-	4	60
2.3	Flat Cars with Fittings	228	17	27	201
2.4	Cement Cars	103	3	3	100
2.5	Grain Cars	407	6	107	300
2.6	Transporters	27	4	27	-
2.7	Other Special Cars	2	2	2	-
	General Car FleetThe	5885	570	1880	3925

Transit loaded cars include loaded cars transiting via the Baku-Turkmenbashi, Baku-Aktau, and Baku-Kuryk ferries. Freight cars, snowplow cars, and transport cars, as well as cars equipped for special freight, commercial, and passenger transportation, located at wagon preparation points for transportation, are always accepted as empty cars in the railway's inventory. Cars decommissioned are referred to as non-operational cars. The non-operational cars include the following freight cars:

- technically faulty freight cars,
- freight cars in the railway administration's reserve,

- freight cars used for other railway section operations,
- freight cars intended for sanitary, technical, and special railway section needs.

All railway freight cars held in reserve by Azerbaijan Railways CJSC, as well as cars intended for occasional seasonal agricultural transportation (grain, wheat, and other food products), must be accounted for in accordance with local authorities' decisions. The rules for the placement, storage, issuance and accounting of wagons in reserve of Azerbaijan Railways CJSC are established in a special charter.

Technically defective wagons are freight cars that do not meet the standards and requirements of the Technical Operating Rules, are considered unfit for transport operations due to their technical condition, are unsuitable for storing and protecting the transported cargo, and have been opened and repaired by railway crews or wagon inspectors. All defective wagons in the CIS railway fleet, as well as defective wagons of enterprises and organizations of other ministries, companies, and departments, whose eight-digit number begins with the number 5 and which have received permission to enter the CIS interstate network in accordance with the established procedure, are subject to mandatory numbering.

Freight wagons held in reserve by Azerbaijan Railways Closed Joint-Stock Company, wagons operated for technical and special purposes, and wagons used for other technical purposes, when accepted for repair from the time of issuance of a warning letter on Form VU-23 until the time of issuance of a warning letter on Form VU-36. The group of wagons identified during inventory after repairs (major and depot), but not in service, includes all freight wagons intended for sanitary, special, and utility purposes, as well as wagons used for other technical purposes in the industry.

It is known that the rules for registering the existence, condition, and use of freight wagons are determined by special instructions [12]. According to paragraph 3.7 of these instructions [12], the group of wagons allocated for technical and special needs of railways includes wagons used from the inventory fleet of Azerbaijan Railways CJSC.

Therefore, it is proposed to include the following special cars in the group of all freight cars intended for economic, technical, and special needs on the railway:

- mobile road section workshops and laboratory cars,
- cars used for medical and sanitary needs,
- flat cars and cars for rail welding trains,
- cantilever and overhead railway cranes,
- cars for fire and repair trains,
- cars at road machine stations and diagnostic cars,
- cars for the transportation of raw materials, spare parts, and materials,
- cars for the storage and transportation of refrigerants, compressed gases, oil and petroleum products,
- hopper-dispensers for the transportation of crushed stone and sand from storage warehouses,
- cars used to prevent and eliminate washouts and damage to railway tracks and artificial railway structures (bridges, tunnels, viaducts, overpasses, etc.) as a result of floods and floodwaters,
- cars used for electrification and power generation, locomotive operations, civil engineering, construction and water supply, and other technical and special railway needs. In accordance with the instruction [12], all freight cars intended for economic, sanitary-technical, diagnostic-control and special needs on the Azerbaijan Railways are divided into the following groups of special cars:

1. Cars for medical and sanitary purposes,
2. Flatcars for railway welding trains,
3. Cantilever and bridge railway cranes,
4. Cars for fire and repair trains,
5. Cars at road equipment stations and diagnostic cars,
6. Laboratory cars and mobile workshops of road sections,
7. Cars for the transportation of raw materials, spare parts and materials,
8. Cars for the storage and transportation of refrigerants, compressed gases, oil and petroleum products,
9. Hopper cars (dosing cars) for the transportation of gravel and sand from warehouses,
10. Cars used for the prevention and Elimination of washouts and damage to tracks and artificial structures (bridges, siphons, crossings, tunnels, viaducts, etc.) of railways resulting from floodwaters and inundations.
11. Carriages used for electrification and power generation, locomotive operation, civil engineering, construction and water supply, as well as for other technical and special needs of railways [12, Articles 4-7].

Carriages for technical, economic, and special needs are allocated within limits established by the Chairman of Azerbaijan Railways CJSC. The rules for the use and accounting of such cars are regulated by special provisions and rules. The transfer of cars from the inventory working fleet to the non-working fleet and vice versa is formalized by notification form DU-6. In many cases, cars from the exchange fleet, provided to the railway company in excess of the norm, are regularly included in the working fleet.

The transfer of cars from the operating inventory fleet to the non-operating fleet and vice versa is documented in accordance with relevant regulations and documents. The transfer time is considered to be the time the document is drawn up; for the railway administration's reserve fleet, it is the time the cars are issued; and for the reserve fleet, it is the time the station receives an order from Azerbaijan Railways JSC to release cars from the reserve fleet. Freight car fleet not under the control of Azerbaijan Railways JSC includes:

- cars provided for temporary use to enterprises and organizations of other ministries and departments on leased tracks with the permission of the chairman of Azerbaijan Railways JSC or his first deputy, under contracts, and on leased tracks. Both sides of these cars must be marked with stencils indicating the name of the leasing company (for "Rental," "Urgent Return"), the station, and the route of registration. Inventory of freight car fleet on the Horadiz-Agbend, Barda-Khankendi, and other railways under construction. The primary information for accounting for the availability of freight cars on the railways under construction is the results of a freight car inventory in physical terms. Current freight car availability on the railways under construction is accounted for using the balance sheet method.

The correct selection and application of freight car utilization indicators is considered a key factor in optimizing the transportation process in rail transport. Freight car utilization indicators are determined based on the fleet of cars operating at stations, depots, track sections, and the railway as a whole. In the rolling stock industry, the key quantitative and qualitative indicators of freight car utilization are the number of cars in the fleet and the volume of freight transported by rail, which are managed by the railway station, the railway, and the national rail network as a whole [1, 11]. In basic studies [8, 9] on wagon management based on freight wagon utilization indicators, the following parameters are considered: The average turnaround time of freight wagons on the railway is calculated in days or hours. The average turnaround time of freight wagons (wagon turnover) is taken to be equal to one

period of the average operating time of the freight wagon fleet during transportation, that is, the time required for loading (unloading) and subsequent re-loading (unloading) of a wagon. Thus, the average turnaround time (in days) of freight wagons is calculated by dividing the number of wagons in the existing operational fleet by the number of completed transport operations according to formula (2);

$$T_o = \frac{\sum N_{rp}^v}{\sum U_{dr}} = \frac{\sum N_{rp}^v}{\sum U_{qr} + \sum U_{pr}} \qquad (2)$$

here $\sum N_{rp}^v$ –-is the total inventory of freight cars on a railway. The primary workload of a railway or track section is defined as the sum of loaded cars $\sum U_{pr}$, $\sum U_{qr}$, and loaded cars received from adjacent tracks or railways.

Many researchers [1,5,9] have calculated the average turnaround time of various types of cars according to known rules using a universal method. However, calculating turnaround time, taking into account car travel time, stops at intermediate stations, technical and commercial operations at technical stations, and freight operations, varies in importance. This article uses special formulas to calculate the average car turnaround time, taking these time parameters into account. Thus, the optimal car turnaround time is calculated to ensure train traffic intensity and railway safety.

1. Wagon turnaround time due to movement is the number of hours wagons spend en route, divided by the time spent in operation, minus the time spent at intermediate railway stations:

$$T_{dov} = \frac{\sum NT_{dv}}{\sum U_{ps}} = \frac{\sum NT_{dv}}{\sum U_{gr} + \sum U_{pr}}, \qquad (3)$$

here, $\sum NT_{dv}$ -is the travel time along the track sections,

2. The turnaround time of wagons depending on the intermediate stations is determined by dividing the wagon-hours during which freight wagons are parked at intermediate railway stations by the wagon operating time,

$$T_{fot} = \frac{\sum N_r}{\sum U_{rv}} = \frac{\sum NT_{ft}}{\sum U_{gr} + \sum U_{pr}}, \qquad (4)$$

here, $\sum NT_{ft}$ - is the time freight wagons spend at intermediate railway stations.

3. Car turnaround time depending on technical stations – by dividing the car-hours during which transit freight cars are idle for work:

$$T_{tor} = \frac{\sum N_r}{\sum U_{tv}} = \frac{\sum NT_{tr}}{\sum U_{gr} + \sum U_{pr}}, \qquad (5)$$

here, $\sum NT_{tr}$ -is the time during which transit cars are idle for work,

4. Car turnaround time for freight operations – by dividing the car-hours during which freight cars are idle for work:

$$T_{gor} = \frac{\sum NT_{gr}}{\sum U_{pv}} = \frac{\sum NT_{gr}}{\sum U_{gr} + \sum U_{pr}}, \qquad (6)$$

here, $\sum NT_{gr}$ - is the time during which the cars are idle under freight handling

Thus, in general, the average car turnaround time can be calculated as follows, taking into account the main characteristics of the cars during freight transportation

$$\theta_{dov} = T_{dov} + T_{fot} + T_{tor} + T_{gor} \qquad (7)$$

The main operational and performance indicator of a railway is labour productivity. Therefore, one of the key performance indicators of a railway is the productivity of wagons, which is determined by the daily freight turnover per wagon of the entire rolling stock in operation. The average daily productivity of freight wagons on a railway shows the average volume of work performed by one wagon in the operational fleet and is defined in net km [9]. This indicator is determined by dividing the net km of wagon fleet operation by the average daily working time of freight wagons in the fleet and multiplying by the number of working days in the reporting period. Therefore, one of the main performance indicators of a rolling stock fleet is the productivity of wagons, which is determined by the daily freight turnover (in ton km net) per wagon of the entire rolling stock in operation [9]. The average daily productivity of freight cars shows the average volume of work performed by one car in the operating fleet and is measured in net tonne-kilometers. This indicator is determined by dividing the net tonne-kilometer of car fleet operation by the average daily operating time of freight cars in the fleet and multiplying by the number of working days in the reporting period:

$$W_v = \frac{\sum(PL)_n}{\sum N_{rb}^g \cdot T}, \qquad (8)$$

hhere, $\sum(PL)_n$–is the freight turnover for the reporting period, called the net tonne-kilometer volume of rail transportation or road operation, and T is the number of working days in the reporting period.

When calculating technical and economic indicators, static and dynamic car loading are distinguished. As is well known, the average dynamic load of a freight car is the mass of cargo transported by the rolling stock on the road during its entire service life, expressed in tons. Thus, the average dynamic load of a freight car in an inventory fleet can be calculated by dividing the net ton-kilometer of road service by the total number of car-kilometers of the freight car fleet in operation [12, pp. 3-5]:

$$Q_{rb} = \frac{\sum(PL)_n}{\sum N^g \cdot S} \qquad (9)$$

here, $\sum N^g \cdot S$ is the total mileage of freight cars in the operating fleet, called a car-kilometer.

The average dynamic load per loaded car, which is considered one of the key operational indicators of a railway, is determined by dividing the operational ton-kilometer of loaded cars in the rolling stock by car-kilometers

$$Q_{qr} = \frac{\sum(PL)_n}{\sum N_{qr} \cdot S}, \qquad (10)$$

here $\sum N_{qr} \cdot S$ -is the mileage of loaded cars in the operating rolling stock of the railway in car-kilometers.

One of the key quantitative indicators of the transportation process is the average daily mileage of a freight car. The average daily mileage of a freight car is the distance traveled by a freight car in the operating fleet over a reporting period (year, quarter, month, week, and day). Thus, the average daily mileage of a freight car is determined by dividing the total mileage of freight cars in the operating fleet by the number of freight cars in the operating fleet and multiplying by the number of days in the reporting period [12, pp. 4-6]:

$$S_v = \frac{\sum N^g \cdot S}{\sum N_{rb}^g \cdot T}, \qquad (11)$$

Technical operations are primarily performed at divisional and marshalling yards. Therefore, such stations are called technical stations, and the movement of cars in this area is determined by a car section or car leg. The average distance between service stations (car sections) is called the average mileage of a freight car in the operating depot between adjacent service operations. The average mileage between service stations is calculated by dividing the car-km traveled by all freight cars in the operating depot by the number of empty transit cars from other lines:

$$L_v = \frac{\sum N^g \cdot S}{\sum N_{tr}}, \qquad (12)$$

here, $\sum N_{tr}$ - is the total number of transit freight cars from other railways.

The loaded and empty trips of freight cars in a fleet are different. As is well known, a freight car's empty trip is equal to the average distance traveled by a freight car during one complete transportation cycle in the operating fleet, that is, during the car changeover period (in both loaded and empty operations). Thus, a freight car's empty trip is determined by dividing the total mileage of freight cars in the operating fleet in car-km by the railroad's car work:

$$R_{pr} = \frac{\sum N^{g} \cdot S}{\sum U_{op}} = \frac{\sum N^{g} \cdot s}{\sum U_{gr} + \sum U_{pr}}, \quad (13)$$

It is known that the loaded trip of a wagon is the average mileage of a loaded wagon over the entire period of its movement, which is included in the total mileage of the loaded wagon. This indicator is calculated by dividing the mileage of loaded wagons in the operating wagon fleet in transport kilometers by the volume of work performed by the wagon fleet:

$$R_{gr} = \frac{\sum N^{g} \cdot S}{\sum U_{gp}} = \frac{\sum N_{gr} \cdot S}{\sum U_{gr} + \sum U_{pr}}, \quad (14)$$

Table 2 *- Key indicators of freight wagon utilization on the railway network of Azerbaijan Railways CJSC*

№	Indicator Name	Unit	2024 year	2025 year
1	Freight Car Turnover	day	6,5	7,2
2	Average Daily Mileage	km	286	294
3	Average Daily Useful Mileage	km	186	196
4	Static Load	ton	52,4	53,5
5	Dynamic Load of a Working Car	ton	34,5	34,9
6	Dynamic Load of a Loaded Car	ton	54,4	55,7
7	Average Daily Productivity*	ton·km netto	8345	8452

Technical work (inspection, technical commercial inspection, etc.) on wagons is performed at technical stations. Operations such as commercial inspection, inspection, and diagnostic testing of wagons, carried out at the technical station, increase the travel time of wagons, both loaded and fully loaded, which leads to a change in wagon turnover [5, 8].

Following these reports, the required number of freight wagons can be calculated by multiplying the number of loaded wagons per day by the type of rolling stock and the wagon turnover θv:

$$N_{po} = \sum_{i=1}^{n} \left(U_{qr}^{i} \cdot \theta_{в} \right), \quad (15)$$

Currently, the technical and operational indicators for the utilization of the freight wagon fleet of Azerbaijan Railways are calculated using the formulas (1-15) given above. The values obtained by calculating the indicators of rolling stock utilization on the Azerbaijan Railways using formulas (1-15) given in the article are presented in Table 2. Thus, a comparative analysis of the obtained values of rolling stock utilization indicators over the past years requires updating the rolling stock structure and acquiring new freight cars, which allows for an increase in the volume and efficiency of transportation processes in the railway transport of the Republic of Azerbaijan.

CONCLUSİONS. This article examines the freight car fleet structure and the technical performance characteristics of both those operated by Azerbaijan Railways CJSC and those not operated by it, and determines the optimal composition of operational and non-operational cars based on the freight transportation process.

This article systematizes the structure and composition of the entire freight car fleet operated by Azerbaijan Railways CJSC and presents the key functional characteristics of freight cars operating on the country's railways and transit cars from abroad traveling on the railways.

To improve the efficiency of transportation processes in the freight car fleet of Azerbaijan Railways CJSC, a methodology for calculating car fleet utilization indicators has been developed. A formula has been adopted for determining the required number of cars in the fleet based on car fleet utilization indicators. This methodology for selecting freight car fleet utilization indicators will enhance the role of the car fleet in the transportation process, while ensuring the safety and efficiency of freight transportation.

REFERENCES

1. Wagon economy: Textbook / Ustich, I.I. Khaba, V.A. Ivashov, et al.; edited by P.A. Ustich. - M .: Marshurut, 2003.-560 p.

2. Lapshin V.F., Orlov M.V. Fundamentals of technical maintenance of wagons: a trai-ning manual. Ekaterinburg: Ural State Uni-versity of Railway Transport, 2006, 375 p.

3. Gursky, E. P. Multifactor model for calculating the required fleet of freight cars / Bulletin of BelGUT. - 2007. - No. 1-2. - P. 90-94

4. Treshina, N.P. Economics of railway transport / N.P. Crack, B.M. Lapidis, M.F. Trikhinkov. -M.: UMK, Ministry of Railways of Russia, 2011,-597 p

5. Anikeeva-Naumenko L. O. Methods for Improving the Efficiency of Freight Car Use in Rail Transport. Author's dis. for Cand. Sci. (Econ.), Moscow, MGUPS (MIIT) – 2014, 24 p. Defended on 14.05.2014

6. "State Program for the Development of the Railway Transport System of the Republic of Azerbaijan in 2010-2014" Order No. 1002, Baku, July 6

7. Azerbaijan Railways CJSC: Baku 2025, www.railway.gov.az

8. Carriages. Fundamentals of design and exami-nation of technical solution / edited by V. N. Ko-turanova. – Moscow : Marshrut. – 2004. – 490 p. – ISBN 5-89035-256-3

9. Improving the structure of the wagon fleet. Railway transport and technology: Collection of works of the Scientific and Practical Conference, Issue 1 (256): Ural State University of Railway Transport, October 29-30, 2023. Yekaterinburg, Russia, 2024. Articles 17-19.
https://council.usurt.ru/b/rtt-7ex-mme-wsy

10. Elyazov I.Sh., Hasanli E.H., Hasratova L.M. Railways, Textbook. "Cooperation" editi. Baku 2014. 504 p.

11. Elyazov I.Sh, Bagirov B.I., Huseynov I.D., Nazarov A.A., Abdullayev R.R. Railway transport vehicles //Textbook for technical higher schools. Baku: 2023,–324p.
https://www.research-gate.net/publi-cation/376981431_DMIR-YOL_NQLIYYATI-NIN_HRKT_VASITLRI

12. Instructions for recording the availability, condition and use of freight cars (Approved by the Ministry of Railways of the Russian Federation dated 03.08. 2000. No. CD-TsChU/771).

INFORMATİON ABOUT THE AUTHORS

1. **Elyazov Israil Shukur ogly**
Azerbaijan University of Architecture and Construction, Baku,
Department of Transport and Logistics
Candidate of Technical Sciences,
Associate Professor,
e-mail: elyazov1962@mail.ru
https://orcid.org/0000-0002-7690-9996

2. Guliyev Etibar Baktiyar oglu
Azerbaijan University of Architecture and Construction, Baku,
Department “Transport and Logistics”
Candidate of Technical Sciences,
Associate Professor,
e-mail: etibar.guliyev@azmiu.edu.az
https://orcid.org/0000-0001-9512-4599

Prospects for the use of liquefied gas in marine diesel engines

Romanoz Topuria[1], Teimuraz Kochadze[1], Mikheil Lejava[2], Zaza Shubladze[2], Malxaz Tavdgiridze[2]

Akaki Tsereteli State University, 59 Tamar Mepe St., Kutaisi 6400, Georgia[1]
Batumi State Maritime Academy, 53 Rustaveli Ave., Batumi 6010, Georgia[2]
romtop54@gmail.com , temko1954@gmail.com , m.lejava@bsma.edu.ge , z.zhubladze@bsma.edu.ge , malxazi2938@mail.ru

Abstract: *the paper discusses the preparation of a fuel mixture consisting of liquefied gas and diesel fuel in marine diesel engines through the implementation of the gas–diesel process, where diesel fuel is used as pilot fuel. This approach reduces the ignition delay period compared to conventional liquid fuels, shortens combustion duration, and extends the flammability limits of the working mixture. Improved mixture formation leads to an increase in combustion rate and more complete combustion during the active combustion phase, causing the engine cycle to approach the Otto cycle. As a result, the environmental and performance characteristics of the diesel engine are significantly improved compared to conventional diesel and standard gas–diesel engines. The paper also analyzes the dependence of ignition delay on combustion parameters and fuel injection timing.*

KEYWORDS: *GASEOUS FUEL, LIQUEFIED GAS, MARINE DIESEL ENGINE, PILOT FUEL, DUAL-FUEL COMBUSTION, IGNITION DELAY.*

1. Introduction

During recent decades, the number of transport piston engines operating on liquid petroleum fuels has significantly increased, while gasoline, diesel fuel, and heavy fuels still remain the primary energy sources. Consequently, global petroleum consumption has risen considerably, whereas oil reserves continue to decline. According to current extraction and consumption rates, proven oil reserves are estimated to last approximately 40 years, while natural gas reserves may last about 60 years [2].

Despite optimistic forecasts regarding the discovery of new deposits and the development of advanced extraction technologies, it is evident that petroleum resources are finite. Over time, oil extraction will become increasingly difficult and expensive. There may eventually come a point when oil reserves remain available, but their extraction becomes economically impractical due to excessive production costs. Therefore, the actual cost of petroleum fuels will inevitably continue to rise.

Under these circumstances, several important questions arise:

1. Is there an alternative to piston internal combustion engines, or will they retain their dominant role in global energy systems?
2. Which fuels should be considered перспективіve in the near and long-term future?
3. What structural modifications will be required for piston engines to adapt to new fuel types?

As noted in [1], answers to these questions should be based on accumulated scientific knowledge, engineering experience, and the forecasts of leading specialists in the field of piston engines.

Historically, transport fuel transitioned from coal-based fuels to petroleum fuels approximately one hundred years ago. Today, another major transition is underway, this time toward natural gas. According to increasingly strict international environmental regulations, LNG (Liquefied Natural Gas) is regarded as one of the fuels of the future. Experts predict that LNG will become widely used in large-scale transportation systems. According to DNV (Det Norske Veritas), LNG conversion represents one of the most promising solutions for marine propulsion engines.

The high price of diesel fuel and growing environmental concerns have accelerated the development of technologies based on economical and environmentally friendly fuels such as natural liquefied gas. Compared to petroleum fuels, LNG offers significant advantages in terms of environmental protection, safety, reliability, and fuel economy. Research has shown that the use of LNG considerably reduces sulfur oxide (SOx) emissions and substantially decreases carbon dioxide (CO_2) and nitrogen oxide (NOx) emissions. LNG-fueled engines can achieve nearly zero sulfur oxide emissions, which is particularly important following the implementation of ECA regulations in 2015 and subsequent international standards. Due to the lower carbon content of LNG, harmful CO_2 emissions are reduced by approximately 25%.

Internal combustion piston engines remain among the most efficient thermal engines currently available, which explains their widespread application in all transport sectors. However, one of their major disadvantages is the dependence on petroleum-based liquid fuels. Therefore, further development prospects for these engines are directly associated with the transition toward gaseous and alternative fuels.

Diesel engine conversion can be implemented either through the gas–diesel cycle or through spark-ignition operation using gaseous fuels. The gas–diesel process is technically advantageous because the engine retains the ability to operate in conventional diesel mode when necessary. Gas–diesel engines typically employ qualitative load regulation. At the same time, combined regulation is recommended in order to avoid excessively rich mixtures, which increase hydrocarbon (CnHm) emissions and deteriorate fuel economy.

2. Preconditions and Methods for Solving the Problem

An important issue is the determination of the influence of pilot fuel dosage and injection advance angle on gas–diesel engine operation. To evaluate the influence of pilot fuel dosage, the dynamic factor is introduced as:

$$K=G_{di}/G_{gi} \quad (1)$$

where: G_{di} – quantity of pilot diesel fuel; G_{gi} – quantity of gaseous fuel.

It is also important to determine the equivalent excess air coefficient:

$$\alpha_{\text{eqv}} = \frac{L}{m_g l_g + m_d l_d} \quad (2)$$

where: *mg* – quantity of gaseous fuel; *lg* – air required for complete combustion of gaseous fuel; *md* – quantity of liquid fuel; *ld* – air required for complete combustion of liquid fuel; *L* – quantity of air entering the cylinder.

The ignition delay period plays a decisive role in ensuring an efficient engine working cycle. Therefore, when converting diesel engines to gaseous fuels and designing advanced dual-fuel engines, it is necessary to establish reliable relationships for determining the

ignition delay period τi\tau_iτi, allowing sufficiently accurate prediction of combustion onset.

Currently known ignition delay equations may generally be divided into two groups [2]. The first group includes equations based on the fundamental theory of chain reactions, particularly the equation proposed by Academician N.N. Semenov:

$$\tau_i = const p^{-n} e^{\frac{E}{RT}} \quad (3)$$

where: n – constant; R – universal gas constant; p – pressure; T – temperature; E – activation energy.

Some researchers introduced additional coefficients accounting for the specific features of the piston engine cycle, as proposed by Hiroyasu and co-authors [4]. Nevertheless, these equations remain variations of Equation (3) and generally contain exponential functions.

Consequently, obtaining reliable relationships for calculating ignition delay when diesel engines operate on various gaseous fuels

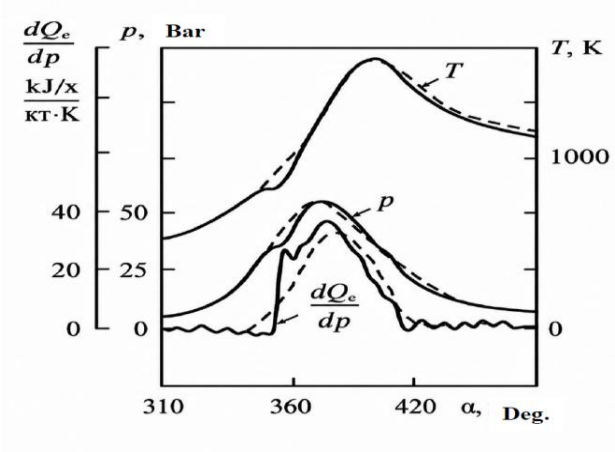


Fig. 1. *Pressure variation in the cylinder of a diesel engine converted to dual-fuel operation (LNG + pilot diesel fuel): experimental (solid line) and calculated (dashed line) results.*

The heat release rate variation $dQx/d\varphi=f(\varphi)$ during the working cycle is determined by processing the indicator diagram.

During fuel evaporation, heat absorption occurs when $dQx/d\varphi<0$, which subsequently changes into heat release after ignition when $dQx/d\varphi>0$ (Fig. 1). The instant when: $dQxd\varphi=0$ is accepted as the beginning of ignition.

Temperature and heat release rates were obtained from indicator diagram processing using Wiebe's law with combustion parameter m=2.03m = 2.03m=2.03.

The heat release characteristics in a dual-fuel engine confirm the statement of A.L. Boehman and O. Le Corre that the combustion process in dual-fuel engines consists of four stages:

1. ignition delay period - $dQx/d\varphi<0$
2. kinetic combustion of the pilot diesel fuel;
3. kinetic combustion of natural gas;
4. diffusion combustion of natural gas together with the remaining pilot fuel.

Among the factors determining good engine performance characteristics (power, torque, efficiency, etc.), combustion completeness and combustion rate are of decisive importance.

— compressed natural gas, liquefied gas, and hydrogen-containing synthesis gas — remains an important scientific and practical task. When operating on liquefied gaseous fuel, external mixture formation occurs because mixing begins in the intake system. Subsequently, the gas–air mixture is compressed inside the cylinder, while ignition is initiated near the end of compression through injection of a pilot dose of diesel fuel.

The volume between the gas injector and the combustion chamber must be carefully selected. Although a larger volume improves mixture homogenization, incorrect volume selection may produce undesirable effects. After the intake valve closes, a certain amount of gaseous fuel may remain trapped in this volume, potentially igniting in either the intake or exhaust systems.

In dual-fuel operation mode, the ignition delay period τi\tau_iτi is defined as the time interval between pilot diesel fuel injection and self-ignition of the liquefied gas–air mixture. The accuracy of determining τi\tau_iτi primarily depends on the method used to identify ignition onset. Several methods have been proposed [2]; in the present work, a method based on heat release rate analysis was employed.

Therefore, the adjustment of fuel supply system parameters and fuel injection advance angle must consider these factors.

The completeness of combustion for two-phase fuel combustion is calculated according to Wiebe's equation:

$$x = \beta \cdot x_1 + (1-\beta) \cdot x_2,$$

or:

$$x = \beta \cdot \left\{1 - e^{\left[a_1\left(\frac{\varphi-\varphi_{10}}{\Delta\varphi_1}\right)^{m_1+1}\right]}\right\} + (1-\beta) \cdot \left\{1 - e^{\left[a_2\left(\frac{\varphi-\varphi_{20}}{\Delta\varphi_2}\right)^{m_2+1}\right]}\right\},$$

where β is the phase separation coefficient. When the pilot diesel fuel quantity is approximately 10%, the coefficient for the first phase are: $\beta \approx 0.10-0.15$, and for the second phase – 1- β $\approx 0.85-0.90$.

The combustion rate with respect to crankshaft rotation angle is expressed as:

$$W_\varphi = \frac{dx}{d\varphi} = -\beta \cdot \frac{a_1(m_1+1)}{\Delta\varphi_1} \cdot \left(\frac{\varphi-\varphi_{10}}{\Delta\varphi_1}\right)^{m_1} \cdot e^{\left[a_1\left(\frac{\varphi-\varphi_{10}}{\Delta\varphi_1}\right)^{m_1+1}\right]} -$$

$$-(1-\beta) \cdot \frac{a_2(m_2+1)}{\Delta\varphi_2} \cdot \left(\frac{\varphi-\varphi_{20}}{\Delta\varphi_2}\right)^{m_2} \cdot e^{\left[a_2\left(\frac{\varphi-\varphi_{20}}{\Delta\varphi_2}\right)^{m_2+1}\right]}$$

Using the above relationships, calculations of combustion completeness and combustion rate for the diesel fuel + liquefied gas mixture were performed as functions of crankshaft rotation angle. Calculations and graphical analyses were carried out using Microsoft Excel Worksheet.

The following initial parameters were used:

- Phase separation coefficients: $\beta=0.1$, $1-\beta=0.9$;
- Shape coefficients: $m1=1$, ; $m2=2.5$;
- Combustion start angles: $\varphi 10=335^0$, $\varphi 20=340^0$;
- Combustion durations: $\Delta\varphi 1=12^0$, $\Delta\varphi 2=50^0$;
- Maximum combustion completeness: $x10max=0.999$, $x20max=0.999$;
- Constants: $a1=-6.908$, $a2=-6.908$.

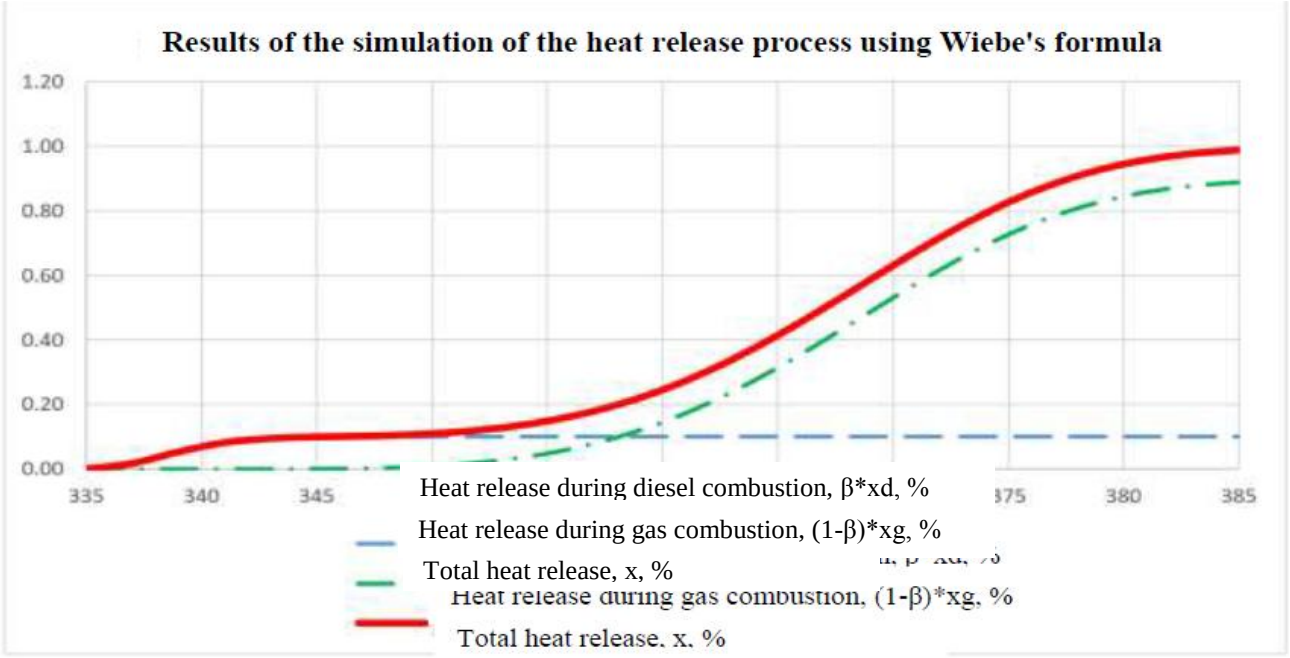


Fig. 2. *Dependence of combustion completeness on crankshaft rotation angle at $\varphi_{10}=335^0$; $\varphi_{20}=340^0$.(Other settings are the same)*

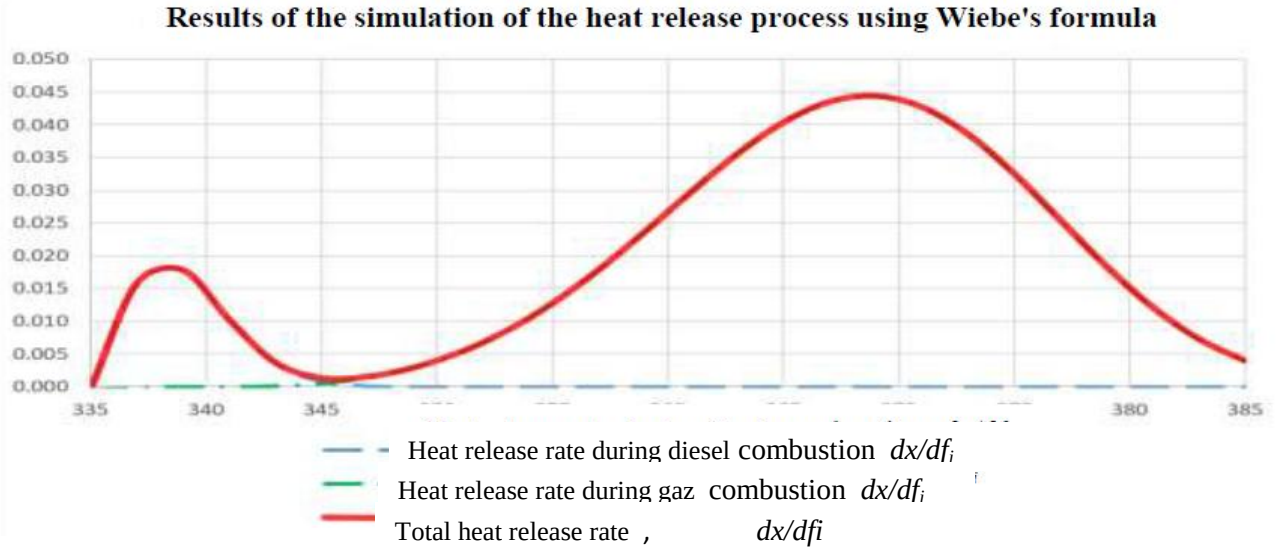


Fig. 3. *Dependence of heat release rate on crankshaft rotation angle at $\varphi_{10}=335^0$; $\varphi_{20}=340^0$.(Other settings are the same)*

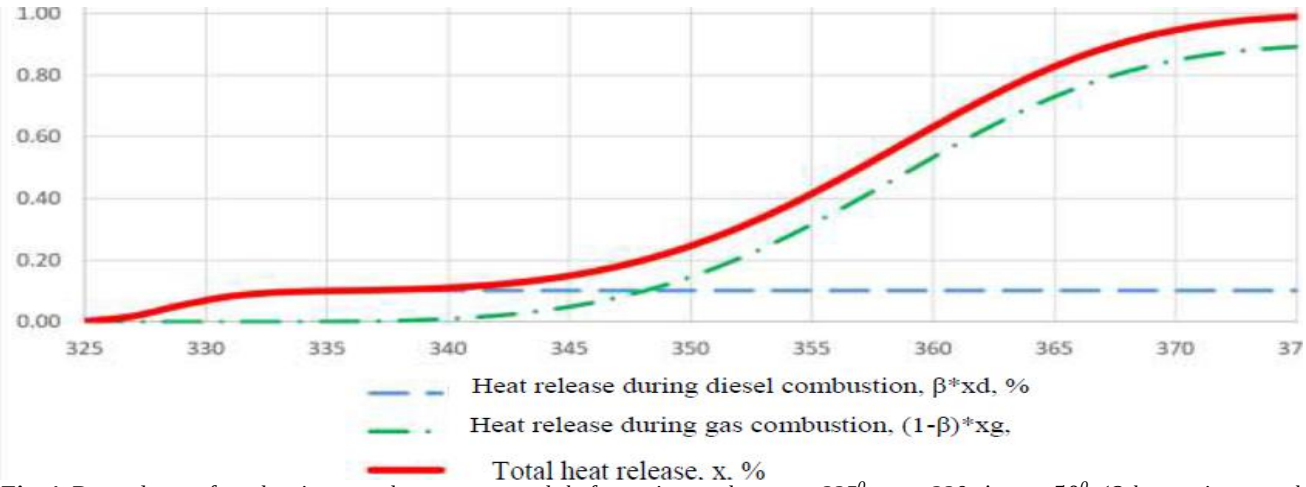


Fig. 4. *Dependence of combustion completeness on crankshaft rotation angle at $\varphi_{10}=335^0$, $\varphi_{20}=330$; $\Delta\varphi_2 = 50^{0\prime}$ (Other settings are the same)*

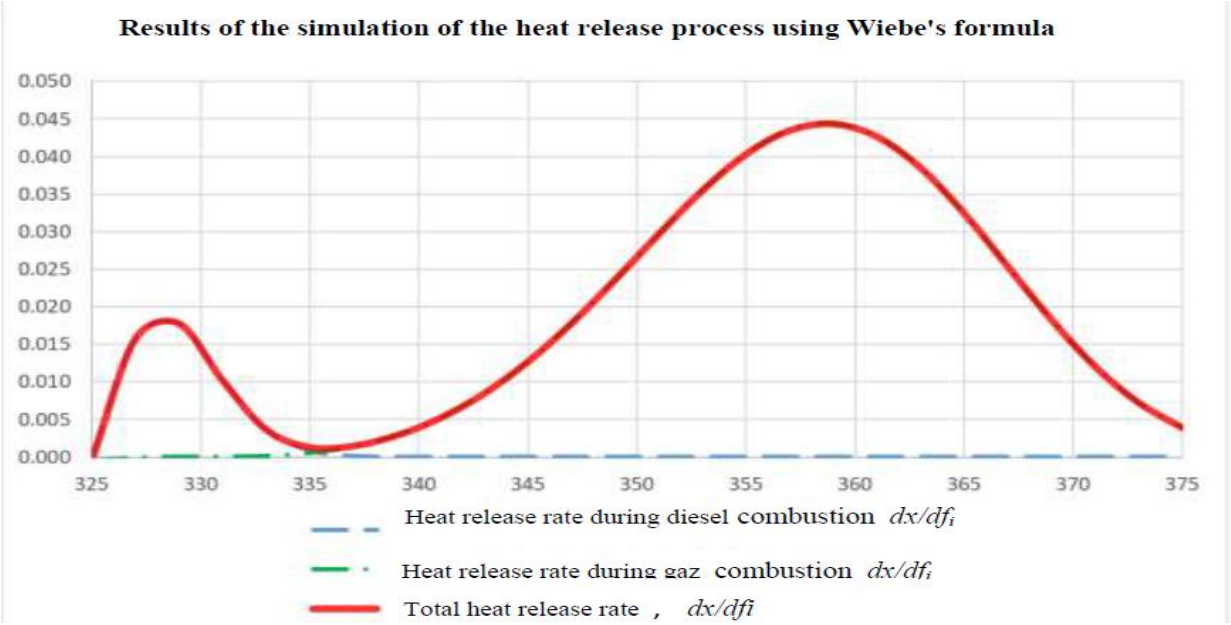


Fig. 5. *Dependence of heat release rate on crankshaft rotation angle at $\varphi_{10}=325^0$, $\varphi 20=330^0$. $\Delta\varphi_2 = 50^0$, (Other settings are the same)*

3. Conclusion

Figure 2 shows the dependence of combustion completeness on crankshaft rotation angle when pilot fuel injection occurs at 335∘335^\circ335∘. Under these conditions, combustion of both fuels is completed within the range of $335–385^0$ indicating a reduction in ignition delay and consequently improved effective engine parameters.

Figure 3 demonstrates that the maximum heat release rate for liquid fuel reaches 0.018 at 338^0, whereas for liquefied gas fuel the maximum value of 0.045 is achieved at 368^0 .

Figures 4 and 5 illustrate the same parameters when liquid fuel injection occurs earlier, at 325^0. In this case, complete combustion occurs within the range of $325^0–375^0$. The maximum heat release rate for liquid fuel reaches 0.018 at 327^0 , while for gaseous fuel it reaches 0.045 at 357^0 . Such an early injection advance is not acceptable because the piston has not yet reached top dead center, while the heat release rate already reaches its maximum value. This leads to piston deceleration and consequently reduces effective engine performance parameters.

Therefore, analysis of the theoretical research results demonstrates that combustion duration and heat release rate depend on pilot fuel properties (particularly self-ignition temperature), pilot fuel quantity, and injection advance angle. The theoretical investigation established that for liquefied natural gas and pilot diesel fuel operation, fuel injection at nominal engine speed should occur at a crankshaft rotation angle of approximately 335^0∘.

4. References

1. Galyshev Yu.V., Magidovich L.E. *Prospects for the Use of Gaseous Fuels in Internal Combustion Engines.* Dvigatelestroyeniye, 2001, No. 3, pp. 31–35.
2. Kavtaradze R.Z. *Theory of Piston Engines. Special Chapters.* Moscow: Bauman Moscow State Technical University Publishing House, 2008, 720 p.
3. Boehman A.L., Le Corre O. *Combustion of Syngas in Internal Combustion Engines.* Combustion Science and Technology, 2008, Vol. 180, No. 6, pp. 1193–1206.
4. Hiroyasu H., Kadota T., Arai M. *Fuel Spray Characterisation in Diesel Engines.* In: Mattavi J.N. and Amann C.A. (eds.), *Combustion Modeling in Reciprocating Engines.* Plenum Press, 1980, pp. 369–408.

Piston secondary dynamics and their effect on blow-by, friction and power loss.

Erjon Selmani[1], Shpresa Caslli[1], Fadil Likaj[2]
Polytechnic University of Tirana, Albania[1]
European University of Tirana, Albania[2]
eselmani@fim.edu.al

Abstract: *In this paper the effect of the piston secondary dynamics was investigated. The piston secondary dynamics comprises the rotation around the pin axis and the translation of the piston body between the two sides of the liner. The most prominent situation of this motion arises on diesel engines. For this purpose ©Ricardo RINGPACK simulation suite was used to simulate the behavior of the piston and rings of a turbodiesel engine. In particular, three aspects of the work of the engine were analysed: Gas blow-by, friction and power losses of the pack. In order to detect the magnitude of the secondary dynamics of the piston, the engine was simulated in two conditions, with and without the secondary motions of the piston. According to results, the rings of a piston without the secondary motion, maintain a more stable position in relation with the piston groove and are more able to prevent gas flows. Furthermore, the secondary motions elimination seems to decrease the friction between components and thus to slightly improve the power loss of the assembly, although at a smaller magnitude with respect to the blow-by gasses.*

Keywords*: PISTON SECONDARY DYNAMICS, PISTON RINGS, BLOW-BY, POWER LOSS.*

1. Introduction

The piston is responsible to transmit the power and torque to the crankshaft while the rings are responsible to seal the combustion chamber. They work together and affect each other at the same time. The rings have three degrees of freedom, axial, radial and twist, and their motion is a combination of inertia, gas pressures and friction forces [1-2]. The piston primary motion is the translation between the dead centers, however it undergoes also to a secondary motion which is a combination of a rotation and a displacement perpendicular to the axis. The secondary dynamics negative effects associated with this movement are engine noise (especially when the engine is cold), wear of the surfaces and cavitation of the lubricating oil [3-4]. The secondary motion is related to the eccentricity of the wrist-pin axis and to the gap between the piston skirt and the liner. Previous studies have highlighted several factors affecting the gas dynamics [5, 6]. In literature, previous analyses [7] have thoroughly considered the tribological performance, in [yang] the structural parameters on the secondary motion are analysed, [8-9] detailed a model of the piston secondary motion for understanding the vibration due to the piston slap.

This study is designed to understand how secondary piston dynamics affect ring sealing capacity and package power losses, as a combined effect rather than separate approaches.

The present work features a specific analysis which will be done comparing the same engine with and without the secondary motion. The mathematical model of the problem was formulated in terms of ring, gas and piston dynamics and solved in ©Ricardo RINGPAK and elaborated in Matlab®. The analysis was applied to a turbo diesel engine and the performance of the ring-pack was evaluated in terms of inter-ring pressures, ring axial and radial dynamics, ring-liner clearances and blow-by gases. The results are then discussed and compared between the cases and the work ends with the conclusions stemming from the discussions.

2 Piston Secondary Motion Model

The secondary dynamics of the piston are shown in Figure 1, it reflects the displacement of the piston normal to the axis (slap) and the rotation around the wrist pin (tilt).

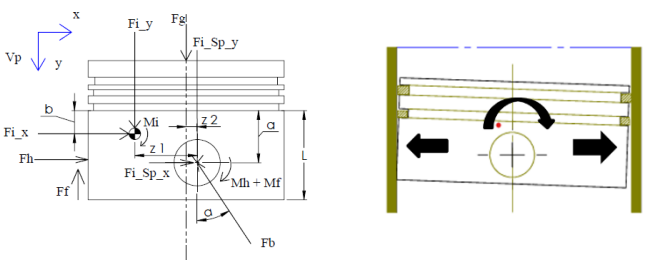


Fig. 1 *Free body diagram of the piston and piston secondary motions*

The equations (1)-(3) below are necessary to model the piston secondary dynamics are written below. Those equations include gas and inertial forces, but also the hydrodynamic forces related to the oil film pressure and its viscous friction effect.

(1) $$F_g - F_f + F_{i_y} + F_{i_Sp_y} - F_b * cos\alpha = 0$$

Where: F_g is the gas force, F_f is the friction force, F_{iy} is the inertia force on y, F_{ispy} is the inertia force on the wrist pin, F_b is the connecting rod force.

(2) $$F_h + F_{i_x} + F_{i_Sp_x} - F_b * sin\alpha = 0$$

Where: F_h is the hydrodynamic force, F_{ix} is the inertia force on x, F_{ispx} is the inertia force on the wrist pin.

(3) $$M_h + M_f + M_i - F_b * z2 - F_{iy} * z1 + F_{i_y} * (a - b) = 0$$

Where :M_i inertia moment on the piston, M_h, M_f, hydrodynamic and friction moments on the wrist pin, a, b, z1 z2 dimensions,
L skirt length.
The hydrodynamic pressure exerted by the oil on the surfaces can be calculated using the 2-dimensional Reynolds equation with partial derivatives (4).

(4) $$\frac{\vartheta}{\vartheta_y}\left(h^3\frac{\vartheta_p}{\vartheta_y}\right) + \frac{1}{R^2}\frac{\vartheta}{\vartheta_\varphi}\left(h^3\frac{\vartheta_p}{\vartheta_\varphi}\right) = -6\mu V_p\frac{\vartheta_h}{\vartheta_y} + 12\mu\frac{\vartheta_h}{\vartheta_t}$$

Where : h is the oil film thickness, μ is the dynamic viscosity, Vp is the piston velocity. R is a conversion factor.

3.1 Modelling Of Gas And Ring Dynamics

In order to compute the inter-ring gas pressures and flows, the ideal gas equation (4) is coupled with the continuity equation (5).

(4) $$\left(\frac{dp}{dt}v + \frac{dv}{dt}p\right) = \left(\frac{dm}{dt}\right)RT + mR\left(\frac{dT}{dt}\right)$$

Where : p is the pressure, v is the volume, m is the gas mass, R is gas constant and T is the inter-ring temperature.

(5) $$\frac{dm}{dt} = Q_{in} - Q_{out}$$

Where Qin, Qout are the mass flow entering and exiting a crevice

The flow through the gap can be modeled using the orifice-flow model for a laminar and compressible flow, meanwhile the temperature of the gas can be assumed to have an isothermal distribution and thus be equal to the temperature of the surrounding walls.

Consequently, the equilibrium equations (Newton's second law) for axial, radial and torsional motion of each ring can be written according to equations (6) to (8).

(6) $$m_r\frac{d^2x}{dt^2} = F_P - F_i - F_s - F_f$$

Where mr is the mass of the ring, indexes mean pressure, inertia, squeeze from oil, friction.

(7) $$m_r \frac{d^2y}{dt^2} = F_{gas_{back}} + F_{tension} - F_{gas} - F_{Poil}$$

Where the forces are exerted in radial faces of the ring

(8) $$I\frac{d^2\alpha}{dt^2} = M_{gas} + M_{gr_oil} + M_{l_oil} - M_{pre}$$

Where I is the ring moment inertia,α is the ring rotation.

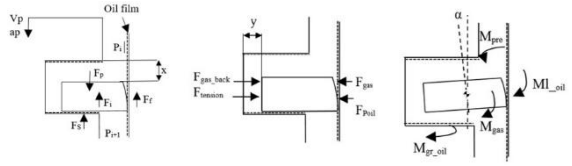


Fig. 2 *Free body diagram of the rings*

4 .3 Modelling Of Boundary And Lubricated Contact

In this work, the clearance between the two interacting surfaces when there is contact is modeled using the Greenwood-Tripp model, equation (9). It is a statistical contact mechanics model based on the clearance distribution h and the composite asperity parameters (surface roughness), when the lubricating film becomes thin enough that surface asperities begin to touch. The outcome of the model is the so called asperity pressure profile Pa .

(9) $$P_a = \frac{16\sqrt{2}}{15}\pi(\eta\beta\sigma)^2 E\sqrt{\frac{\sigma}{\beta}}F\left(\frac{h}{\sigma}\right)$$

Where: η is the composite asperity density, β is the composite radius of curvature of asperities, σ is the composite R.M.S. surface asperity height, E is the elastic modulus of the contact surfaces.

After the asperity pressure, we calculated the asperity shear stress, according to equation (10) below.

(10) $$\tau_a = C * P_a$$

Where C is the friction coefficient of the coupled surface.

Then the calculation of the power loss due to asperities (11).

(11) $$P_{a_loss} = F_{asperities}\, v = \int_{x1}^{x2} L\,\tau_a\, v\, d_x$$

Where $F_{asperities}$ is the asperities friction force, L is the ring length, v is the velocity.

The total friction which the rings are subjected is composed of two parts, as given in equation (12)

(12) $$Ftotal = Fhydrodynamic + Fasperities$$

The hydrodynamic or viscous friction force can be computed according to equation (13) below.

$$F_{hydrodynamic} = \int \tau_\omega\, dA$$

Where τ_ω is the oil shear stress and is a function of the oil velocity and dynamic viscosity μ, which can be easily computed from the Reynolds theory of thin-film lubrication.

3 Simulation

Theoretically speaking, the piston dynamics affects the ring dynamics and both are able to interfere in the gas flow due to the equilibrium of forces and moments.

Each ring is allowed to have three degree of freedom, so does the piston, while the gas flows through a complex series of channels and crevices between two large volumes (combustion chamber and crankcase). Previous authors have investigated other parameters and factors that affect the ring dynamics and gas flow, but in none of these cases has the effect of the secondary piston movement been specified as the only parameter investigated.

At this purpose RINGPAK Solver of ©Ricardo was used to perform simulations. In this case a turbodiesel 4-cylinder engine was used as a reference, running at full load condition and three speed regimes: 2000, 3000 and 4000 rpm.

The geometry and dimensions of the rings are given in figure 3.

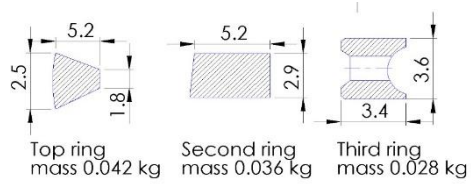


Fig. 3 *Ring geometry, dimensions and masses*

The model requires also the oil type and properties, as well as the lubrication model and respective boundary conditions. For this purpose a SAE Grade 5W30 oil was used, on the other hand Navier-Stokes lubrication model with half-Sommerfeld ring-liner boundary conditions is adopted. The ring-liner contact is depicted in figure 4.

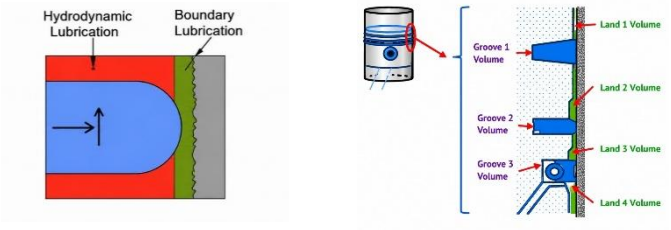


Fig. 4 *Ring – Liner contact under boundary and hydrodynamic lubrication (left). Inter ring crevices (right)*

In order to proceed with the solution of the mathematical model, some assumptions are needed with respect to the gas-flow model. We will assume a uniform gas pressure in each land and groove volume. The gas used is assumed to behave as an ideal gas, hence it obeys to the ideal gas equation, with its temperatures in the several orifices to be assumed iso-thermal. To calculate the gas mass flow rate, the isentropic gas flow model has been used.

Given the large clearance at the piston edge, the crown top land pressure can be set equal to the cylinder pressure, while the piston bottom land pressure equal to the crankcase.

The surface asperity profile and data are taken from the engine manufacturer, while the piston and cylinder liner distortions have been accounted from previous works, figure 5.

The cylinder bore distortion affects the ring conformation the correct through the radial contact of the ring face to the liner.

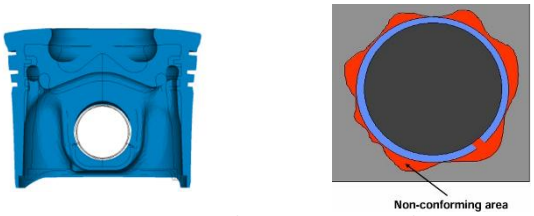


Fig. 5 *Piston distortion (left) and ring non conformability to a distorted bore (right)*

The simulations were repeated twice for each speed value, with and without the piston secondary motion. A series of outcomes were

then analysed, in particular the ring motions, the inter ring pressures, the piston dynamics, the gas flow,the blow-by the friction forces and the power loss form the ringpack. The results were analysed and compared between the two cases taken in exam.

4 Simulation, results and discussion.

4.1 Base Case: 2000 rpm, piston secondary motion enabled.

In figure 6, are depicted the ring axial locations during a complete cycle of 720 degree of the crank angle, for the 2000 rpm case. The first ring lifts substantially only during the exhaust and intake stroke of the working cycle, when the gas pressure above this ring is lower than the pressure below it. The second ring shows a nearly unstable position, while the third ring is always seated.

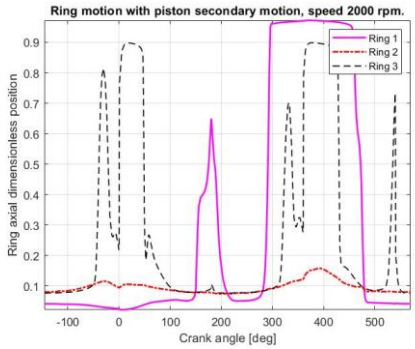


Fig. 6 *Ring axial positions during a cycle*

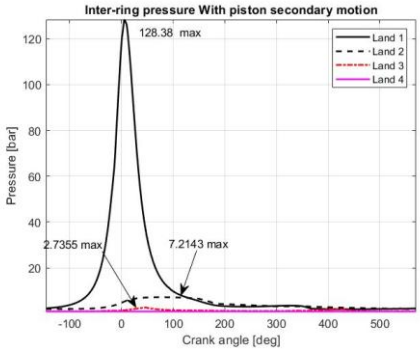


Fig. 7 *Inter-Ring pressures*

Figure 7 shows the inter-ring pressures during a cycle with the respective maximal values, while figure 8 shows the blow-by curves. The positive area is the downward direction of the gas, the negative area is the upward direction, the difference in area represents the lost gasses to the crankcase or blow-by.

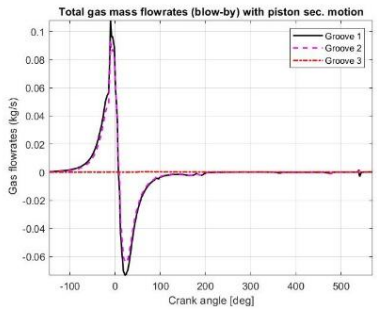


Fig. 8 *Blow-by for a complete cycle*

In figure 9 are represented the ring friction force curves. As depicted, the maximal value of this force is reached from the top ring during the beginning of the expansion stroke, with a maximal value of 650 Newton. In the following figure 10, are depicted together the asperity and hydrodynamic forces. As it clearly showed, the asperity friction if the far most important of the two.

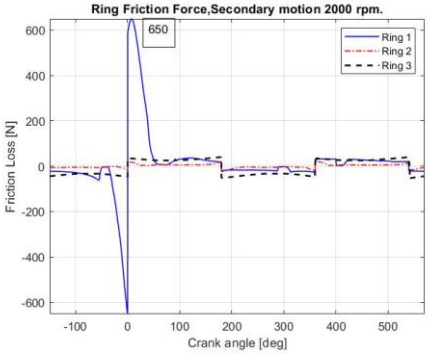


Fig. 9 *Ring friction force*

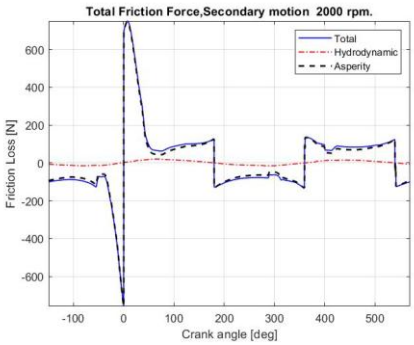


Fig. 10 *Total ring friction force*

In the following figure 11 and 12 are depicted the power losses for this case for a cycle. As figures witness, the total power loss from the ring pack, for a cycle is nearly 3.8 kw. Just for clarity, the effective power of the engine is 115 kw.

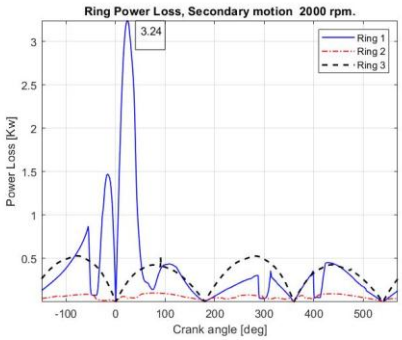


Fig. 11 R*ing power loss*

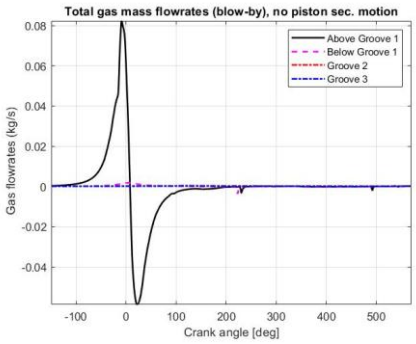


Fig. 12 *Total Ring power loss*

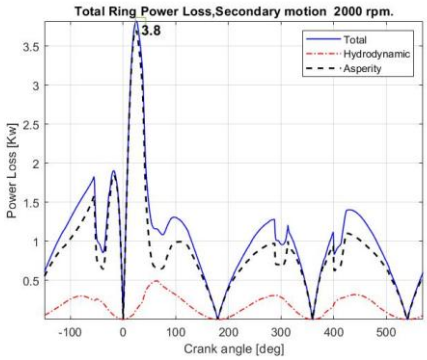


Fig. 13 *Ring axial positions, no secondary motion during a cycle*

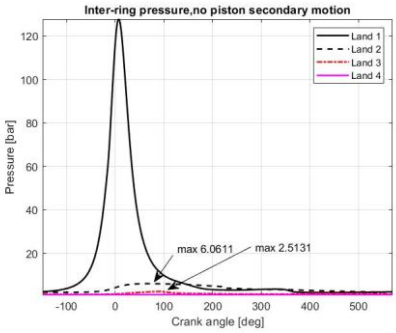


Fig. 14 *Inter-ring pressures, no secondary motion*

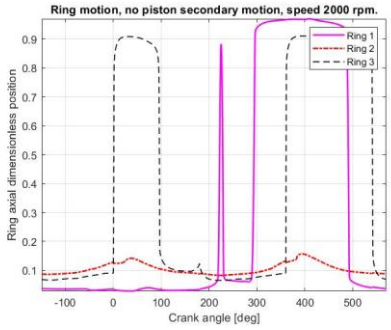


Fig. 15 *Blow-by, no secondary motion.*

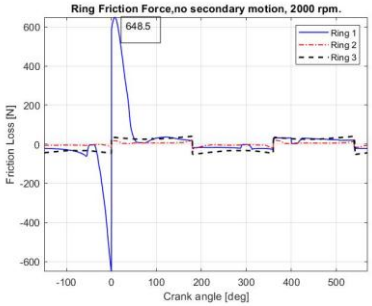


Fig. 16 *Ring friction force, no secondary motion*

4.2 Alternative Case: 2000 rpm, piston secondary motion Disabled.

In figures 13 are depicted the ring axial locations. As we can see, the top ring has a similar behavior, while the second ring seems to be more stable. According to figure 14, the peak pressure of the second land is lower in comparison to the previous case, which is a clear sign of a better sealing of the first ring. At last, in figure 15 the blow-by values are clearly lower. In figures 16 to 18 are depicted the friction forces and power losses for the ring pack. In this case, the curves are similar to the previous case but the friction and the power loss are higher.

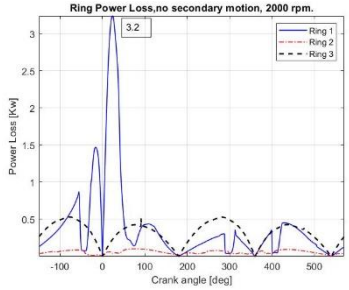


Fig. 17. R*ing power loss, no secondary motion*

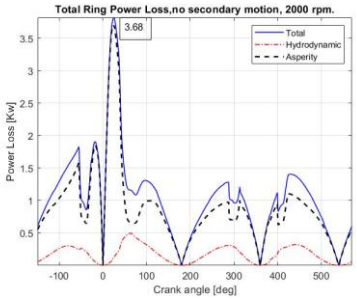


Fig. 18. *Total power loss, no secondary motion*

4.3 Comparison for 3000 and 4000 rpm case.

In table 1 below, are reported the values of gas blow-by for the other two cases, namely 3000 and 4000 rpm and compared to the 2000 already described.

In table 2 instead, are reported the values of ring friction forces and power losses for the other cases and compared between them.

Table 1*. Total blow-by gas in mass for every simulated case*

	Blow-by		
Case	2000 rpm	3000 rpm	4000 rpm
Base (secondary motion enabled)	0.1194 [kg]	0.102 [kg]	-0.00785 [kg]
Secondary motion disabled	0.00612 [kg]	0.0053 [kg]	0.00403 [kg]

Table 2: *Ring one Friction force and total Power loss for every case analysed.*

	Total Ring 1 friction force [N]/total power loss [kW]		
Case	2000 rpm	3000 rpm	4000 rpm
Base Case (secondary motion enabled)	650/3.8	728.4/5.56	729.4/7.46
Secondary motion disabled	648.5/3.68	726/5.45	727/7.40

According to the results of table 1, increasing the engine speed the blow-by level reduces, the reduction is more remarked in the case of the original setup with the secondary motion included. When the secondary motion of the piston is disabled, the blow-by undergoes to a steady reduction, which can be synonymous of a normal functioning of the piston and the ring-pack. On the other hand, the negative value for the base case and 4000 rpm speed can be related to a irregular working condition of the rings, namely axial flutter and radial collapse, as described in certain references. Figure 19 explains how the ringpack performs with and without the secondary motion.

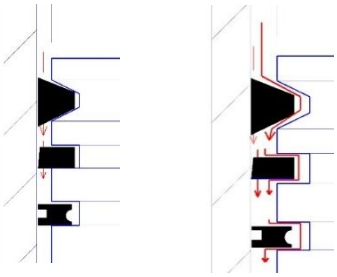


Fig. 19. *Piston-liner clearances with and without secondary motion.*

From the values reported in table 2, it is possible to note how the engine performance drops in terms of friction force and power loss. Increasing the engine speed increases the friction force due to asperities, which is always the dominant factor. On the other hand, with the secondary motion disabled, the friction forces and consequently the power loss is slightly lower than the base case. This result may be related to the contact pattern of the rings to the liner, which without the secondary motion, it may result in a smaller contact surface,

5 Conclusion.

An internal combustion engine was simulated virtually through ©Ricardo RINGPAK suite to understand the impact of the piston secondary motion on the sealing capability of the ringpack and the effect on the friction force and power losses from the ring pack.

The secondary motion of the piston is a combination of a tilt and a displacement which may occur to the piston during certain strokes, and force the piston to move perpendicularly to the cylinder axis or to rotate around the pin axis. In this analysis a turbo-diesel 4-cylinder engine was used as a test at full load, and three different speeds; 2000, 3000 and 4000 rpm.

According to the analysis and discussion and comparison of the results in table 1, the engine with the disabled secondary motion is able to perform much better in terms of containment of blow-by gasses.

The main reason for this is a better positioning of the piston and the rings both in axial and radial direction in relation to the contact with the groove and the liner wall.

When the piston tilts and twists, it is pushed against one side of the liner, opening more crevices on the opposite side. In this situation, the rings are unable to seal properly because the gas can flow easily through the grooves and past the rings in addition to the ring gaps.

In addition, when the secondary motion is included, the ring twist angles are altered between positive and negative, which is a sign of a non-optimal positioning and possible instability.

On the other hand, without the secondary motion, even the ring friction forces (mainly asperity) and the power losses are lower than with the secondary motion, although of a lower magnitude than the differences in blow-by.

The secondary motion of the piston is used in some diesel engines, for reducing the force component against the cylinder wall, but it may be also a consequence of the wear of the piston skirt and cylinder liner due to the mileage. Its elimination could bring positive effects, but sometimes it is necessary to be accounted.

6. References

1. Keribar, Rifat, Zafer Dursunkaya, and Michael F. Flemming. "An integrated model of ring pack performance." ASME, Transactions, Journal of Engineering for Gas Turbines and Power 113 (1991): 382-389.

2. Wannatong, Krisada, Somchai Chanchaona, and Surachai Sanitjai. "Simulation algorithm for piston ring dynamics." Simulation Modelling Practice and Theory 16.1 (2008): 127-146.

3.Tan, Yeow-Chong, and Zaidi Mohd Ripin. "Analysis of piston secondary motion." Journal of Sound and Vibration 332.20 (2013): 5162-5176.

4. Delprete, Cristiana, Abbas Razavykia, and Paolo Baldissera. "Detailed analysis of piston secondary motion and tribological performance." International Journal of Engine Research 21.9 (2020): 1647-1661.

5. Delprete, Cristiana, Erjon Selmani, and Arian Bisha. "Gas escape to crankcase: impact of system parameters on sealing behavior of a piston cylinder ring pack." International Journal of Energy and Environmental Engineering 10.2 (2019): 207-220.

6. Selmani, Erjon, Cristiana Delprete, and Arian Bisha. "Engine Speed and Load Effect on the Sealing Capacity of a Piston Ring-Pack." International Conference “New Technologies, Development and Applications”. Cham: Springer International Publishing, 2020.

7. Delprete, Cristiana, Abbas Razavykia, and Paolo Baldissera. "Detailed analysis of piston secondary motion and tribological performance." *International Journal of Engine Research* 21.9 (2020): 1647-1661.

8. Tan, Yeow-Chong, and Zaidi Mohd Ripin. "Analysis of piston secondary motion." *Journal of Sound and Vibration* 332.20 (2013): 5162-5176.

9. Yang, Haixiang, et al. "Research on the influence of key structural parameters on piston secondary motion." *Scientific Reports* 11.1 (2021): 19080.